# Stability of magnesite in the Earth lower mantle: insight from high-pressure and high-temperature experiments.

**Lélia Libon**

A thesis
submitted in fulfillment
of the requirements for the degree of
*Doctor rerum naturalium*
(Dr. rer. nat.)
in the scientific discipline **Mineralogy**

submitted to the
Faculty of Mathematics and Natural Sciences
Institute of Geosciences
of the University of Potsdam

*Submitted on*: 22.03.2023
*Defended on*: 18.07.2023, Potsdam

*Supervisors:*
Prof. Max Wilke
Dr. Karen Appel

*Reviewers:*
Prof. Max Wilke
Prof. Sébastien Merkel
Prof. Stephan Klemme

Published online on the
Publication Server of the University of Potsdam:
https://doi.org/10.25932/publishup-60461
https://nbn-resolving.org/urn:nbn:de:kobv:517-opus4-604616

# Dedication

A ma mère, Isabelle. C'est avec toi que je partage cet accomplissement.

# List of publications

The content of this thesis has been or is in the process of being published in the following contributions:

**Libon, L.**, G. Spiekermann, I. Blanchard, J. M. Kaa, S. Dominijanni, M. Förster, M. J. Sieber, C. Albers, W. Morgenroth, K. Appel, C. McCammon, A. Schreiber, V. Roddatis, K. Glazyrin, R. Husband, L. Hennet, M. Wilke. **Reevaluating the fate of subducted magnesite in the Earth's lower mantle.** (in review).

Albers, C., Sakrowski, R., Thiering, N., **Libon, L.**, Spiekermann, G., Kaa, J., Gretarsson, H., Sundermann, M., Tolan, M., Wilke, M., Sternemann, C. **High-efficient X-ray emission spectroscopy of cold-compressed $Fe_2O_3$and laser-heated pressurized $FeCO_3$ using a von Hámos spectrometer.** (in review in Journal of Analytical Atomic Spectrometry).

Albers, C., Sakrowski, R., Libon, L., Spiekermann, G., Winkler, B., Schmidt, C., Bayarjargal, L., Cerantola, V., Chariton, S., Giordano, N., Gretarsson, H., Kaa, J., Liermann, H-P., Sundermann, M., Thiering, N., Tolan, M., Wilke, M., and Sternemann, C. (2022). **$Fe^{3+}$-hosting carbon phases in the deep Earth.** Physical Review B, 105(8), 085155.

Spiekermann, G., Libon, L., Albers, C., Sakrowski, R., Petitgirard, S., Sahle, C. J., Sundermann, M., Gretarsson, H., Sergueev, I., Sternemann, C., Wilke, M., and Murakami, M. (2021). **Reflective imaging, on-axis laser heating and radiospectrometry of samples in diamond anvil cells with a parabolic mirror.** High Pressure Research, 41(2), 142-154.

Mergner, V., Kupenko, I., Spiekermann, G., Petitgirard, S., Libon, L., Chariton, S., Krug, M., Steinbrügge, R., Sergueev, I., and Sanchez-Valle, C. (2021). **Sound Velocities in FeSi at Lower Mantle Conditions and the Origin of Ultralow-Velocity Zones.** Geophysical Research Letters, 48(14), e2020GL092257.

Spiekermann, G., Kupenko, I., Petitgirard, S., Harder, M., Nyrow, A., Weis, C., Albers, C., Biedermann, N., Libon, L., Sahle, C. J., Cerantola, V., Glazyrin, K., Konôpková, Z., Sinmyo, R., Morgenroth, W., Sergueev, I., Yavas, H., Dubrovinsky, L., Tolan, M., Sternemann, C. and Wilke, M. (2020). **A portable on-axis laser-heating system for near-90° X-ray spectroscopy: application to ferropericlase and iron silicide.** Journal of synchrotron radiation, 27(2), 414-424.

## *Others co-authors publications:*

*In review:*

Kaa, J., Konôpková, Z., Preston, T. R., Cerantola, V., Sahle, J. C., Förster, M., Albers, C., **Libon, L.**, Sakrowski, R., Wollenweber, L., Buakor, K., Dwivedi, A., Mishchenko, M., Nakatsutsumi, M., Plückthun, C., Schwinkendorf, J-P., Spiekermann, G., Thiering, N., Petitgirard, S., Tolan, M., Wilke, M., Zastrau, U., Appel, K., Sternemann, C. **A von Hámos spectrometer for diamond anvil cell experiments at the High Energy Density Instrument of the European X-ray free electron laser.** (in review in Journal of Synchrotron Radiation).

Biedermann, N., Morgenroth, W., Spiekermann, G., Kaa, J., **Libon, L.**, Gabarino, G., Mezouar, M., Pakhomova, A., Wirth, R., Wilke, M., Appel, K. **Stability and chemical reactions of carbonates in presence of Mg-Fe-silicates at conditions of the Earth's mantle.** (in review in EPSL).

*Published:*

Kaa, J., Sternemann, C., Appel, K., Cerantola, V., Preston, T. R., Albers, C., Elbers, M., Libon, L., Makita, M., Pelka, A., Petitgirard, S., Plückthun, C., Roddatis, V., Sahle, C. J., Spiekermann, G., Schmidt, C., Schreiber, A., Sakrowski, R., Tolan, M., Wilke, M., and Konôpková, Z (2022). **Structural and electron spin state changes in an X-ray heated iron carbonate system at the Earth's lower mantle pressures.** Physical Review Research, 4(3), 033042.

Krstulović, M., Rosa, A. D., Sanchez, D. F., Libon, L., Albers, C., Merkulova, M., Grolimund, D., Irifune, T., and Wilke, M. (2022). **Effect of temperature on the densification of silicate melts to lower Earth's mantle conditions.** Physics of the Earth and Planetary Interiors, 323, 106823.

# Abstract

Carbonates carried in subducting slabs may play a major role in sourcing and storing carbon in the deep Earth's interior. Current estimates indicate that between 40 to 66 million tons of carbon per year enter subduction zones, but it is uncertain how much of it reaches the lower mantle. It appears that most of this carbon might be extracted from subducting slabs at the mantle wedge and only a limited amount continues deeper and eventually reaches the deep mantle. However, estimations on deeply subducted carbon broadly range from 0.0001 to 52 million tons of carbon per year. This disparity is primarily due to the limited understanding of the survival of carbonate minerals during their transport to deep mantle conditions. Indeed, carbon has very low solubility in mantle silicates, therefore it is expected to be stored primarily in accessory phases such as carbonates.

Among those carbonates, magnesite ($MgCO_3$), as a single phase, is the most stable under all mantle conditions. However, experimental investigation on the stability of magnesite in contact with $SiO_2$ at lower mantle conditions suggests that magnesite is stable only along a cold subducted slab geotherm. Furthermore, our understanding of magnesite's stability when interacting with more complex mantle silicate phases remains incomplete. In the first part of this dissertation, laser-heated diamond anvil cells and multi-anvil apparatus experiments were performed to investigate the stability of magnesite in contact with iron-bearing mantle silicates. Sub-solidus reactions, melting, decarbonation and diamond formation were examined from shallow to mid-lower mantle conditions (25 to 68 GPa; 1300 to 2000 K). Multi-anvil experiments at 25 GPa show the formation of carbonate-rich melt, bridgmanite, and stishovite with melting occurring at a temperature corresponding to all geotherms except the coldest one. In situ X-ray diffraction, in laser-heating diamond anvil cells experiments, shows crystallization of bridgmanite and stishovite but no melt phase was detected in situ at high temperatures. To detect decarbonation phases such as diamond, Raman spec-

troscopy was used. Crystallization of diamonds is observed as a sub-solidus process even at temperatures relevant and lower than the coldest slab geotherm (1350 K at 33 GPa). Data obtained from this work suggest that magnesite is unstable in contact with the surrounding peridotite mantle in the upper-most lower mantle. The presence of magnesite instead induces melting under oxidized conditions and/or foster diamond formation under more reduced conditions, at depths ∼700 km. Consequently, carbonates will be removed from the carbonate-rich slabs at shallow lower mantle conditions, where subducted slabs can stagnate. Therefore, the transport of carbonate to deeper depths will be restricted, supporting the presence of a barrier for carbon subduction at the top of the lower mantle. Moreover, the reduction of magnesite, forming diamonds provides additional evidence that super-deep diamond crystallization is related to the reduction of carbonates or carbonated-rich melt.

The second part of this dissertation presents the development of a portable laser-heating system optimized for X-ray emission spectroscopy (XES) or nuclear inelastic scattering (NIS) spectroscopy with signal collection at near 90°. The laser-heated diamond anvil cell is the only static pressure device that can replicate the pressure and temperatures of the Earth's lower mantle and core. The high temperatures are reached by using high-powered lasers focused on the sample contained between the diamond anvils. Moreover, diamonds' transparency to X-rays enables in situ X-ray spectroscopy measurements that can probe the sample under high-temperature and high-pressure conditions. Therefore, the development of portable laser-heating systems has linked high-pressure and temperature research with high-resolution X-ray spectroscopy techniques to synchrotron beamlines that do not have a dedicated, permanent, laser-heating system. A general description of the system is provided, as well as details on the use of a parabolic mirror as a reflective imaging objective for on-axis laser heating and radiospectrometric temperature measurements with zero attenuation of incoming X-rays. The parabolic mirror improves the accuracy of temperature measurements free from chromatic aberrations in a wide spectral range and its perforation permits in situ X-rays measurement at synchrotron facilities. The parabolic mirror is a well-suited alternative to refractive objectives in laser heating systems, which will facilitate future applications in the use of $CO_2$ lasers.

# Contents

# 1 Introduction

## 1.1 The interior of the Earth

The Earth's mantle plays an important role in the evolution of our planet. Its dynamic forces are exposed through plate tectonics, which eventually determines the habitability at the surface. However, determining the physical and chemical properties of the deep mantle, and the possible exchange between the surface and the deep interior are still major challenges since direct sampling tools are limited.

### 1.1.1 Structure of the Earth's interior

Our knowledge of the Earth's interior structure such as the "preliminary reference Earth model" (PREM) (Dziewonski and Anderson, 1981), as well as other seismological profiles (e.g., iasp91 from Kennett and Engdahl (1991), sp6 from Morelli and Dziewonski (1993) or ak135 from Kennett et al. (1995)), comes from the analysis of seismology data. The seismic waves are refracted according to the physical properties of the medium they passed through (e.g., density and elasticity), and are reflected on discontinuities that mark the boundaries of each layer (Fig. 1.1). Thus, revealing the different Earth's layers at defined depths.

Three main layers are derived from seismological profiles, the crust, mantle, and core, separated from one another by discontinuities. The crust thickness varies, from 7 km thick under the oceanic crust to an average of 35 km under continents and reaching up to 70 km under mountains roots. Below the crust, the mantle is divided into the upper mantle (UP) above 410 km and the lower mantle (LM) between 660 to 2700 km. In between lies the transition zone (TZ), from 410 to 660 km, a region of an

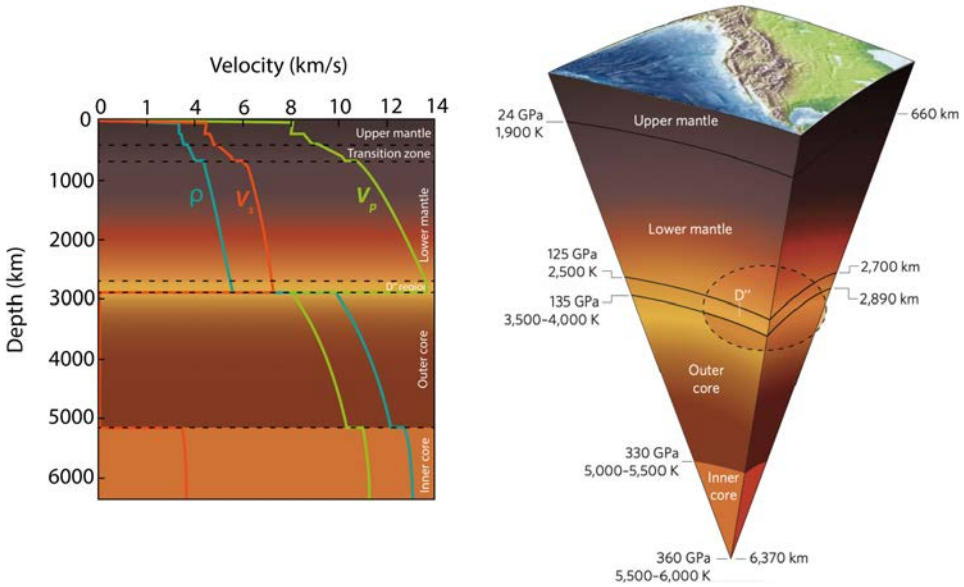


Figure 1.1: Density and velocity profile of Earth modified after Dziewonski and Anderson (1981) and a cross-section showing the expected range of pressures and temperatures of the different layers composing the Earth's interior after Duffy (2008).

anomalously steep seismic velocity gradient. At the core-mantle boundary (CMB), near 2900 km, a 200–300 km thick region, known as D", exhibits an extreme lateral heterogeneity and anomalous properties (Garnero, 2000). The Earth's core is divided into a liquid outer core and a solid inner core. The core is inferred to be primarily composed of a metallic Fe-Ni alloy (McDonough and s. Sun, 1995) but might also contain ∼10 % of light elements (including S, O, Si, C, and H) incorporated during its formation (Birch, 1964; Rubie et al., 2011). Seismic wave signature data are a great tool for probing the inaccessible regions of the planet but do not provide compositional information on the different layers.

### 1.1.2 Composition of the mantle

The upper mantle chemical composition can be constrained by near-surface sampling from mantle peridotite at mid-ocean ridges, ophiolites, and with xenoliths brought back to the surface by volcanism. However, aside from a few inclusions in sublithospheric diamonds believed to originate from the TZ and the lower mantle (Stachel et al., 2000; Kaminsky, 2012) (which are still debated in their interpretations - Kaminsky (2017)), most mantle samples come from less than ∼200 km of depth. Thus, the chemical composition of the TZ and lower mantle relies on a combination of indi-

rect evidence such as cosmochemistry, theoretical calculations, and high-pressure and high-temperature experiments.

Knowledge of the mineralogical composition of the deep mantle is essential for the interpretation of geophysical data. Different theoretical compositional models, based on high-pressure and -temperature experiments are proposed for the mantle, out of which the following two are most commonly assumed: (1) the pyrolite association (ultramafic source), corresponding to the juvenile mantle composition (Ringwood, 1991; Kesson et al., 1998; Irifune et al., 2010) and (2) the basalt association (mafic source), corresponding to the composition of a subducting slab, but approximated by the mid-ocean ridge basalt (MORB) composition, with higher Si and Al contents and lower Mg content (Irifune and Ringwood, 1993; Ono et al., 2001; Hirose et al., 2005).

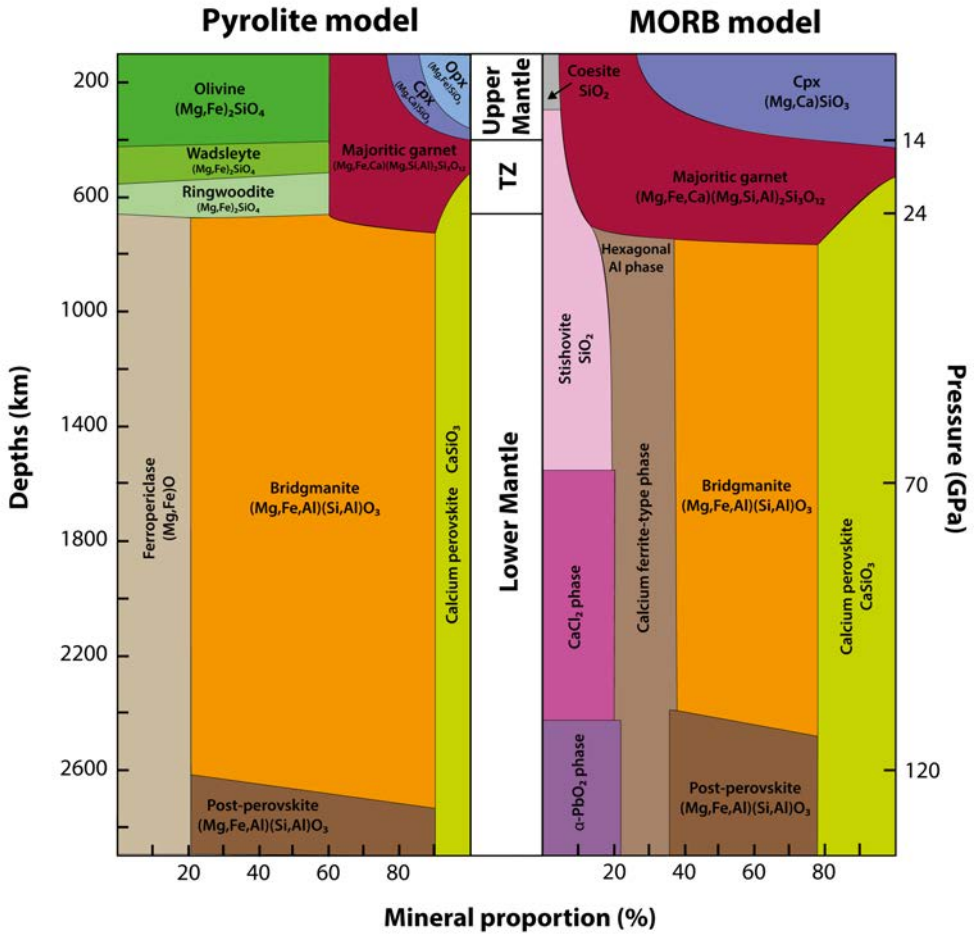


Figure 1.2: Approximate mineral proportions of lower mantle minerals in pyrolite and MORB compositional models as a function of depth, modified after Trønnes (2009), with data from Irifune and Tsuchiya (2007). TZ: Transition Zone, Cpx: Clinopyroxene; Opx: Orthopyroxene.

According to the pyrolite model (Fig. 1.2), the upper mantle consists of four main mineral phases: olivine - $[(Mg, Fe)_2SiO_4]$, orthopyroxene (Opx) - $[(Mg, Fe)SiO_3]$, clinopyroxene (Cpx) - $[(Mg, Ca)SiO_3]$ and an aluminous phase: majoritic garnet $[(Mg, Fe, Ca)(Mg, Si, Al)_2Si_3O_{12}]$. Reaching the transition zone at ∼14 GPa and ∼410 km, the olivine phase undergoes a series of phase transformations forming wadsleyite, marking the beginning of the TZ and then to ringwoodite at ∼17 GPa (∼520 km). Meanwhile, both orthopyroxene and clinopyroxene with the increase of depths/pressure, dissolve in the garnet phase resulting in an increase of the pyroxene components in this phase. At mid-TZ, Opx and Cpx have dissolved completely and only the garnet phase is left. The lower mantle, ∼24 GPa (660 km), is expected to be composed of mainly three mineral phases. The breakdown of ringwoodite and the majority garnet form an assemblage of (1) **bridgmanite** - $[(Mg, Fe)(Si, Al)O_3]$ (Tschauner et al., 2014): a magnesium silicate in the perovskite structure of $ABX_3$ (*Pbnm* space group) (Liu, 1974; Fiquet et al., 2000; Murakami et al., 2012; Hirose et al., 2017), and the most abundant mineral of the Earth (nearly 50% of the bulk Earth in volume) (Ricolleau et al., 2009; Murakami et al., 2012; Mashino et al., 2020; Hirose et al., 2017); and (2) **ferropericlase** - $[(Mg, Fe)O]$ also known as magnesiowüstite. Starting at ≥18 GPa, a Ca-rich phase starts to exsolved from the garnet forming: **Ca-perovskite** - $[CaSiO_3]$ recently named of "davemaoite" (Tschauner et al., 2021). This assemblage is stable throughout most of the lower mantle until the CMB. At CMB, a CaIrO3-type-$(Mg, Fe)SiO_3$ also named post-perovskite phase, resulting from the high-pressure transition of bridgmanite at 107-126 GPa (depending strongly on the composition and the pressure scale used), is expected (Murakami et al., 2004; Hirose et al., 2006; Oganov and Ono, 2004).

The MORB mineral associations (Fig. 1.2) are quite different than the ones from the pyrolytic model, with different volume proportions of minerals. At the upper mantle, the phases comprised are clinopyroxene, garnet, and a free $SiO_2$ phase, coesite transitioning to stishovite at ∼10 GPa. Meanwhile, similar to the pyrolite mantle, Cpx progressively dissolves in garnet. At the topmost part of TZ, the assemblage consists of garnet and a small amount of stishovite. Reaching ∼20 GPa, Ca-perovskite exsolved from the majorite garnet. At the upper part of the lower mantle, an assemblage of stishovite, Ca-perovskite, as well as two phases from the phase transformation of garnet: bridgmanite and an Al-rich phase in the hexagonal structure or a calcium ferrite-type structure are present. At mid-lower mantle (∼62 GPa), stishovite transform in $CaCl_2$-type structure (Ono et al., 2002; Hirose et al., 2005), and in $\alpha$-$PbO_2$

structure at ∼120 GPa (Hirose et al., 2005). The phase transition from bridgmanite to the post-perovskite phase starts at 110 GPa and 2500 K (Hirose et al., 2005). The calcium ferrite-type phase and the Ca-perovskite stay stable up to the bottom of the lower mantle. The proportion of Ca-perovskite in the MORB model accounts for a larger volume (25 vol.%) than in the pyrolite one (10 vol.%) (Hirose et al., 2017), making it a major phase in the TZ and lower mantle. New findings suggest that Ca-perovskite governs the dynamics of subducting slabs and the stagnation of the slab at TZ and lower mantle boundary or at the CMB could contribute to the seismically observed region's low shear-wave velocities (Immoor et al., 2022).

### 1.1.3 The redox state of the mantle

The oxygen fugacity ($fO_2$), first introduced in petrology by Eugster (1957), defines the chemical potential of oxygen and is a fundamental thermodynamic parameter that controls the redox state of Earth's mantle. Fugacity is measured in Pascal but is usually expressed relative to the $fO_2$ value of known solid-state buffers (at given pressure and temperature) such as the fayalite-magnetite-quartz (FMQ: $3\,Fe_2SiO_4 + O_2 = 2\,Fe_3O_4 + 3\,SiO_2$), the iron-wüstite (IW: $2\,Fe + O_2 = 2\,FeO$) or the nickel–nickel oxide (Ni-NiO: $2\,NiO = 2\,Ni + O_2$) buffer. The redox solid-state buffer equilibria are often described as $fO_2$-temperature curves where above it, the oxidized phase is stable, and reciprocally below it, the reduced phase is stable (Fig. 1.3).

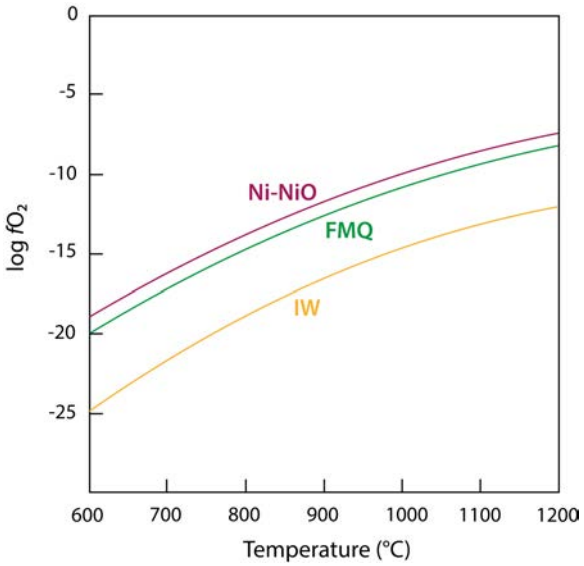


Figure 1.3: Log of the oxygen fugacity as a function of temperature at 1 bar of commonly used buffer equilibria modified after Frost (1991). Ni-NiO: nickel-nickel oxide buffer; FMQ: fayalite-magnetite-quartz and IW: iron-wüstite

The oxygen fugacity controls the valence states of certain elements in minerals, liquids, and gases, which directly influence the redox state of the mantle (Frost and McCammon, 2008). In the upper mantle to ∼200 km depth (6 GPa), the $fO_2$ can be constrained using the $Fe^{3+}/\sum Fe$ relation in rock samples that are formed by partial melting of the mantle, such as MORB or spinel and garnet xenoliths, which are generally found to fall within +1 and -2 log units of FMQ (Frost et al., 2004). At greater depths, $fO_2$ is only estimated, by assuming that the mantle retains a constant $Fe^{3+}/\sum Fe$ ratio. Studies show that the general trend of the $fO_2$ of the mantle is to decrease with pressure/depth, principally due to the effect of pressure on the $Fe^{3+}/Fe^{2+}$ equilibria. Further details on $fO_2$ in the mantle can be found in Frost and McCammon (2008).

At depth of ∼250 km (8 GPa) and below, thermodynamic calculations (Ballhaus, 1995) and experiments (Frost et al., 2004; Rohrbach et al., 2007) demonstrated that a Fe,Ni-rich metal phase precipitate in the mantle from (Fe, Ni)-bearing olivine (O'neill and Wall, 1987). The NiO contained mainly in olivine is reduced forming a Ni-rich metal, and the Fe also contained in the olivine partitions into the metal alloy that forms. At this depth, garnet will host a significant amount of $Fe^{3+}$. These reactions can be described simply by (Frost and McCammon, 2008):

$$\underset{\text{olivine}}{\text{NiO}} + \underset{\text{olivine}}{2\text{FeO}} \longrightarrow \underset{\text{metal}}{\text{Ni}} + \underset{\text{garnet}}{Fe_2O_3} \cdot \tag{1.1}$$

and

$$\underset{\text{olivine}}{3\text{FeO}} \longrightarrow \underset{\text{metal}}{\text{Fe}} + \underset{\text{garnet}}{Fe_2O_3} \cdot \tag{1.2}$$

Therefore, at metal-saturated depths, the $fO_2$ become narrowly constrained reaching a value of IW 0.3 at the bottom of the upper mantle and TZ, where about 0.1 to 0.2 wt.% of metal would form (Frost and McCammon, 2008).

At depths corresponding to the lower mantle (≥24 GPa), the dominant mineral is bridgmanite. Measurements performed on experimental samples have shown that because of the energetically favored coupled substitution of $Fe^{3+}$-$Al^{3+}$ substitution (Richmond and Brodholt, 1998; Navrotsky, 1999; Liu et al., 2017), bridgmanite can incorporate a large amount of $Fe^{3+}$ into its structure relative to other mantle silicate

phases at the same $fO_2$ conditions (Frost and Langenhorst, 2002; Frost and McCammon, 2008). Experimental results show that this strong preference for $Fe^{3+}$, forces the $Fe^{2+}$ contained in ferropericlase to disproportionate producing the high $Fe^{3+}$ content present in bridgmanite (Eq. 1.3).

$$\underset{\text{ferropericlase}}{3Fe^{2+}} \longrightarrow \underset{\text{bridgmanite}}{2Fe^{3+}} + \underset{\text{metal}}{Fe^{0}} \cdot \tag{1.3}$$

It is expected that ∼1 wt.% of Fe-rich metallic phase (∼88 % Fe, ∼10 % Ni and ∼1 % S) can precipitate in the lower mantle (Frost et al., 2004; Frost and McCammon, 2008). Therefore, the $fO_2$ of the lower mantle is narrowly constrained at values around IW to –1.5 log units below IW (Frost et al., 2004), and because of this considerable buffer capacity and its almost infinite reservoir the lower mantle can impose its ambient $fO_2$ conditions on any additional redox-sensitive component, such as carbonates, and carbon-rich fluids (Rohrbach and Schmidt, 2011).

## 1.2 Carbonates in the deep Earth

### 1.2.1 The deep carbon cycle

Carbon is one of the most important volatile elements on Earth. Its presence in the atmosphere is the backbone of building and sustaining a habitable planet. Yet, not all are aware that most of the carbon of the planet is contained in its interior (in mantle and core) (Dasgupta and Hirschmann, 2010). Over geological times, carbon moved between surface and deeper reservoirs, impacting the atmospheric, oceanic, and crustal $CO_2$ budget (Plank and Manning, 2019; Kelemen and Manning, 2015). The term "deep carbon cycle" refers to this long-term cycle taking place in the Earth's interior through the different layers controlled by the global geodynamics of the planet. The global fluxes of carbon still have high uncertainties due to the multiple independent parameters in its input and output mechanisms, and carbon flux estimation from various studies shows a wide range of discrepancies and uncertainties (Table 1.1) (Plank and Manning, 2019; Kelemen and Manning, 2015).

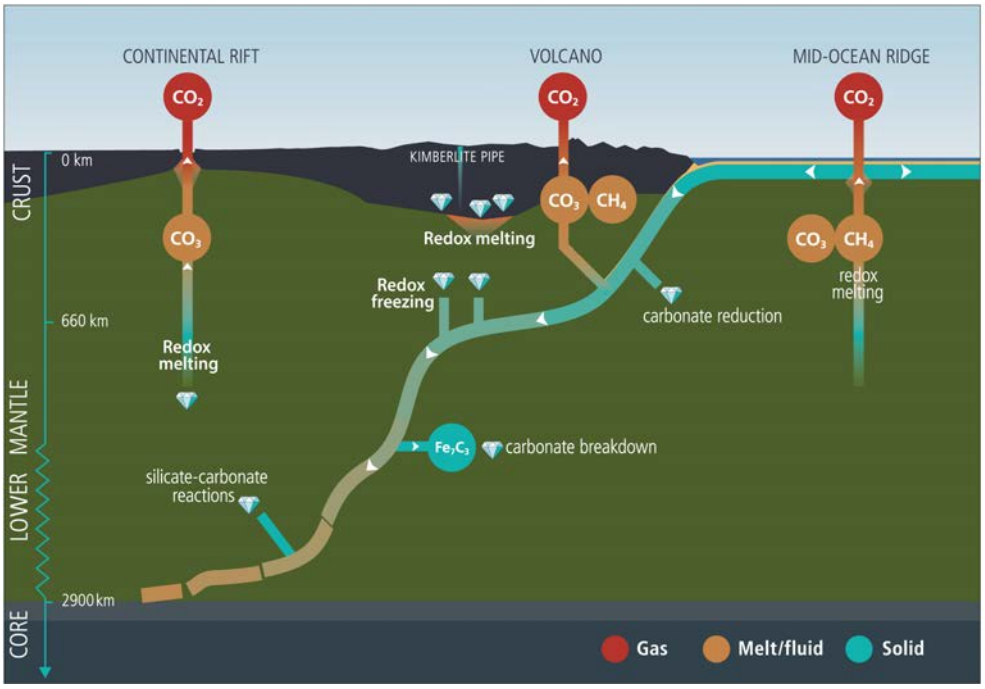


Figure 1.4: Schematic cartoon illustrating the deep carbon cycle modified after Stagno et al. (2019).

Carbon enters the Earth's mantle through subduction zones in the form of seafloor sediments, carbonates contained in the altered oceanic crust (AOC), organic carbon, and from the altered mantle with a total estimate ranging from 39 to 114 Mt of C per yr (Table 1.1). However, the input flux of carbon varies from trench to trench, as subducted slabs are unique in their carbon-bearing component (carbonates, organic carbon, sediment, serpentinites), their temperature field, and slab geometry. Carbon gets released from the mantle to the surface via arc magmatism, mid-ocean ridges, oceanic island volcanoes (OIV), and by diffuse outgassing. The total output estimation range from 30 to 127 Mt of C per yr (Table 1.1).

It appears that this cycle is close to near equilibrium in its input and output fluxes (Table 1.1). Most of the carbon is probably extracted from subducted slabs at the convecting mantle wedge to the mantle lithosphere, the crust, and released by volcanoes or diffuse outgassing to return to the atmosphere (Kelemen and Manning, 2015). However, some carbonates in the altered oceanic may continue to subduct into the deep mantle. It is acknowledged that modern-day subducted slabs penetrate deep into the lower mantle and as carbon has very low solubility in mantle silicates, it is primarily present in accessory phases such as carbonates (Shcheka et al., 2006). These carbonates entrapped in subducted slabs may play a significant role to carry

carbon from the Earth's surface to its very deep interior, with the estimation for deeply subducted carbon broadly ranging from 0.0001 to 52 Mt of C per yr (Kelemen and Manning, 2015) (Table 1.1). This disparity largely stems from the limited understanding of the survival of carbonate minerals during their transport to deep mantle conditions. Current constraints suggest that a significant amount of carbonates may survive the first 150 km of subduction and make it deeper into the Earth's deep mantle (Molina, 2000; Connolly, 2005; Gorman et al., 2006; Kerrick and Connolly, 2001).

| | Planck & Manning, 2019 | Kelemen & Manning, 2015 | Dasgupta & Hirschmann, 2010 |
|---|---|---|---|
| **Input** | | | |
| **Sediments** | 57 to 60 | 13 to 23 | 13 to 17 |
| **AOC** | 18 | 22 to 29 | 12 to 61 |
| **Altered Mantle** | 1.3 to 10 | 4 to 15 | 36 |
| **Deeply subducted carbon** | - | 0.0001 to 52 | 24 to 48 |
| ***Total*** | 82 + 14 | 39 to 66 | 61 to 114 |
| **Output** | | | |
| **Arc volcanoes** | 23 | 18 to 43 | 13 to 37 |
| **Solid storage** | 40 | 0 to 47 | - |
| **Diffuse degassing** | - | 4 to 12 | - |
| **Ridges and OIV** | 16 | 8 to 42 | 13 to 90 |
| ***Total*** | 79 + 9 | 30 to 97 | 31 to 127 |

Table 1.1: Compilation of major carbon fluxes estimated in C of Mt $yr^{-1}$ from Dasgupta and Hirschmann (2010); Kelemen and Manning (2015); Plank and Manning (2019). AOC: Altered Oceanic Crust; OIV: Ocean Island Volcanoes.

### 1.2.2 Melting of subducted carbonate-rich slabs

In order to "survive" subduction and reach the lower mantle, carbonates must bypass re-mobilizing processes such as melting and decarbonation. Investigations on melting temperatures of carbonated-MORB and carbonated-peridotite from the upper mantle to transition zone conditions are central for a better understanding of the behavior of deeply subducted oceanic crust.

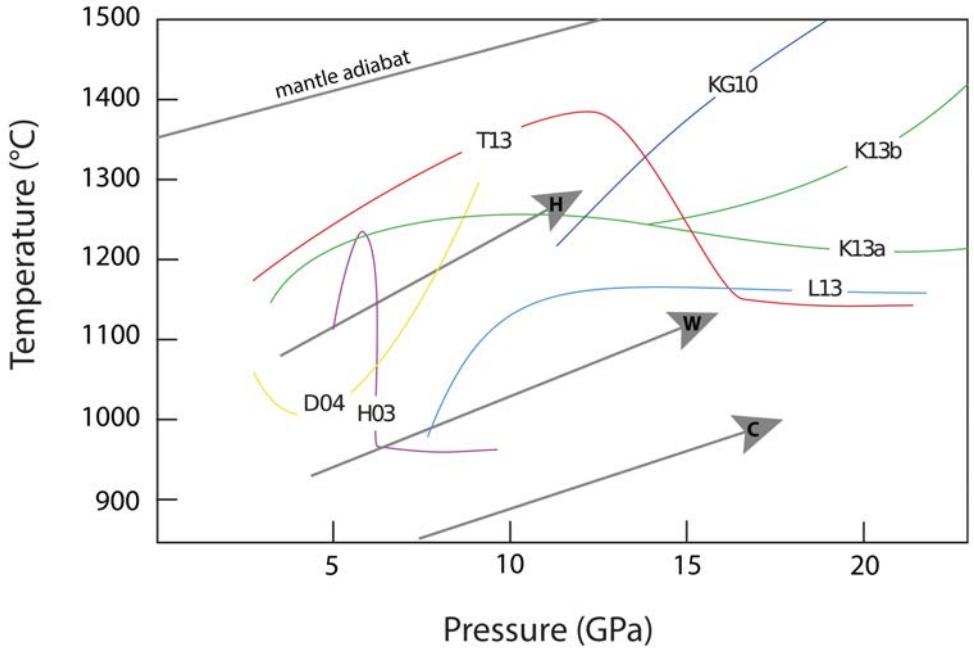


Figure 1.5: Compilation of experimentally determined solidus curves of basaltic compositions modified from Yaxley et al. (2019). Solidus curves for carbonated-MORB are shown as solid-colored curves and are from: H03 - Hammouda (2003); D04 - Dasgupta et al. (2004); KG10 - Keshav and Gudfinnsson (2010); K13a,b - Kiseeva et al. (2013); and T13 - Thomson et al. (2016b). Also shown is the solidus of alkaline carbonatite L13 from Litasov et al. (2013). The mantle adiabat is from Katsura et al. (2010). Model subduction geotherms are H: hot, W: warm, and C: cold slabs from Syracuse et al. (2010).

In Fig. 1.5 a compilation of these anhydrous solidus curves is presented, both on simplified systems (Keshav and Gudfinnsson, 2010) and natural-like systems (Hammouda, 2003; Dasgupta et al., 2004; Yaxley and Brey, 2004; Kiseeva et al., 2013; Thomson et al., 2016b). These solidus curves display large variations of position and shape caused by slight variations of bulk composition between studies; well illustrated with the curve of the study of Kiseeva et al. (2013) (K13a and K13b in Fig. 1.5 and Table 1.2). Most of these solidus curves intersect the hot and warm slabs' geotherms, suggesting that carbonated-rich subducted slabs would undergo melting and lose their carbonate components above the transition zone. This process has been identified to create a barrier for deep carbonate subduction and carbon might be rarely transported beyond transition zone depths but instead is recycled into the overlaying mantle (Thomson et al., 2016b).

| | K13a | K13b |
|---|---|---|
| $SiO_2$ | 45.32 | 42.22 |
| $TiO_2$ | 1.34 | 1.43 |
| $Al_2O_3$ | 14.88 | 15.91 |
| FeO | 8.85 | 9.46 |
| MnO | 0.15 | 0.14 |
| MgO | 7.15 | 7.64 |
| CaO | 14.24 | 14.85 |
| $Na_2O$ | 3.14 | 3.36 |
| $K_2O$ | 0.4 | 0.42 |
| $P_2O_5$ | 0.14 | 0.15 |
| $CO_2$ | 4.4 | 4.4 |
| Total | 100.01 | 99.98 |

Table 1.2: Bulk compositions (as wt.%) of the two compositions of carbonated MORB used in Kiseeva et al. (2013).

However, the possible existence of carbonate-rich melts in the deep mantle strongly depends on the pressure, temperature, and $fO_2$ conditions. Indeed, the redox state of the mantle strongly affects the speciation of volatile elements such as carbon. Oxygen fugacity decreases with the increase in pressure in the upper mantle (see section 1.1.3). Therefore, at depths greater than 250 km, most of the mantle should be too reduced for oxidized carbonate-rich melts to be stable. Therefore, when carbonate-rich melt migrate out of the subduction slabs and interact with the overlying metal-saturated mantle, it causes their reduction to diamond through the 'redox freezing' reaction (Eq. 1.4) (Fig. 1.4) (Rohrbach and Schmidt, 2011; McCammon et al., 2020) :

$$\underset{\text{solid}}{2\text{Fe}} + \underset{\text{solid or melt}}{\text{MgCO3}} \longrightarrow \underset{\text{solid}}{3(\text{Fe}_{2/3}, \text{Mg}_{1/3})\text{O}} + \underset{\text{solid}}{C} \cdot \tag{1.4}$$

where $(\text{Fe}, \text{Ni}, \text{Mg})\text{O}$ is a component in olivine, garnet, and bridgmanite or ferropericlase. Evidence of this process is reported in Thomson et al. (2016b), where inclusions of majorite garnet and calcium-rich silicate in super-deep (or sublitho-

spheric) diamonds (10 to 20 GPa) are reported to form by the interaction between a MORB-derived carbonatite melt and a reduced peridotite. Accordingly, redox freezing is believed to provide an effective mechanism to immobilize carbon-rich melt into diamond across the mantle at depths from ∼250 to ∼700 km, and to contribute to the barrier that hinders carbonate transport into the deep Earth (Thomson et al., 2016b; Rohrbach and Schmidt, 2011). Oxidation of diamond-bearing mantle during re-mobilization by upwelling to lower depths ≤250 km (where the ambient mantle ceases to be metal saturated) can lead to redox melting, the inverse process of redox freezing where melting is triggered by the increase $fO_2$ (Fig. 1.4) (Rohrbach and Schmidt, 2011; Foley, 2010). Those melts may then transport carbon back to the surface in a rising mantle plume, such as within ocean-island basalts (OIB) or carbonatites (Hammouda and Keshav, 2015; McCammon et al., 2020; Dasgupta and Hirschmann, 2010). Despite the evidence for a melting barrier that limits the preservation of subducted carbonates, solid carbonates may bypass melting (Fig. 1.5) and be transported beyond the transition into the lower mantle if carried in the coldest subducting slabs (Thomson et al., 2016b, 2014; Kiseeva et al., 2013).

### 1.2.3 Carbonate inclusions in super-deep diamonds

Transport of carbonates to at least the transition zone has been proposed based on the presence of carbonate inclusions in super-deep (sublithospheric) diamonds from the Juina area, Mato Grosso State, (Brazil) (Brenker et al., 2007; Wirth, 2009; Kaminsky et al., 2015) (Fig. 1.6). Almost 50 different minerals were identified in inclusions in these diamonds. Among them, coexisting periclase (MgO) and wüstite (FeO) were identified, pointing to depths of formation at ≥2000 km (86 GPa) (Kaminsky et al., 2015). These observations raised important questions on the carbon source(s) and the mechanisms to crystallize those diamonds. Subducted carbonates

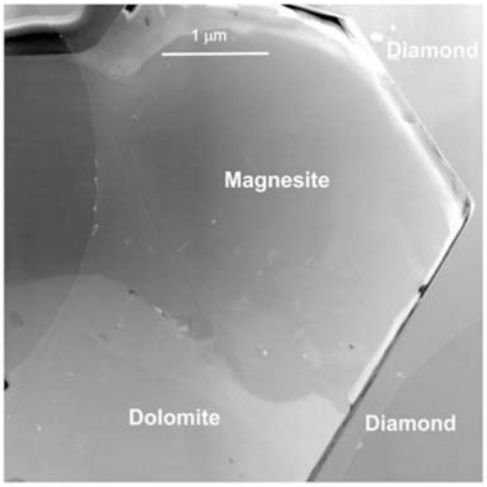


Figure 1.6: TEM image of a syngenetic inclusion of dolomite and magnesite in diamond from Kaminsky et al. (2015).

may provide an appreciable source of carbon to the deep mantle, therefore it is imperative to thoroughly explore their stabilities at lower mantle conditions.

### 1.2.4 Magnesite

In order to act as a carbon carrier in the deep mantle, solid carbonate minerals must be stable under high-pressures and temperatures. Carbonates contained in slabs are mainly calcite/aragonite ($CaCO_3$), magnesite ($MgCO_3$), and dolomite [$(Ca, Mg, Fe)CO_3$]. Among these carbonates, magnesite ($MgCO_3$) is the most likely carbonate phase to be preserved within subducted oceanic crust that reaches the lower mantle. Experimental studies reveal that calcite/aragonite is converted to dolomite and magnesite in the presence of pyroxene at pressures around 4.5 GPa (Kushiro, 1975). Around 5 to 8 GPa dolomite decomposes into magnesite and calcite (Luth, 2001; Sato and Katsura, 2001; Morlidge et al., 2006), hence dolomite and calcite have less potential to transport carbon to Earth's lower mantle, promoting magnesite as the predominant carbonate phase in deeply subducted slabs.

Alone, magnesite is stable as a solid phase throughout all pressure and temperature conditions of the Earth's mantle. Solopova et al. (2015) reported incongruent melting of magnesite between 2100 and 2650 K at pressures from 12 to 84 GPa. The high-pressure polymorph magnesite-II was first reported by Isshiki et al. (2004) and its structure as tetracarbonate (i.e., containing tetrahedral $CO_4$ group instead of the trigonal planar $CO_3$) with monoclinic symmetry (space group *C2/m*) was confirmed recently by Binck et al. (2020) (Fig. 1.7).

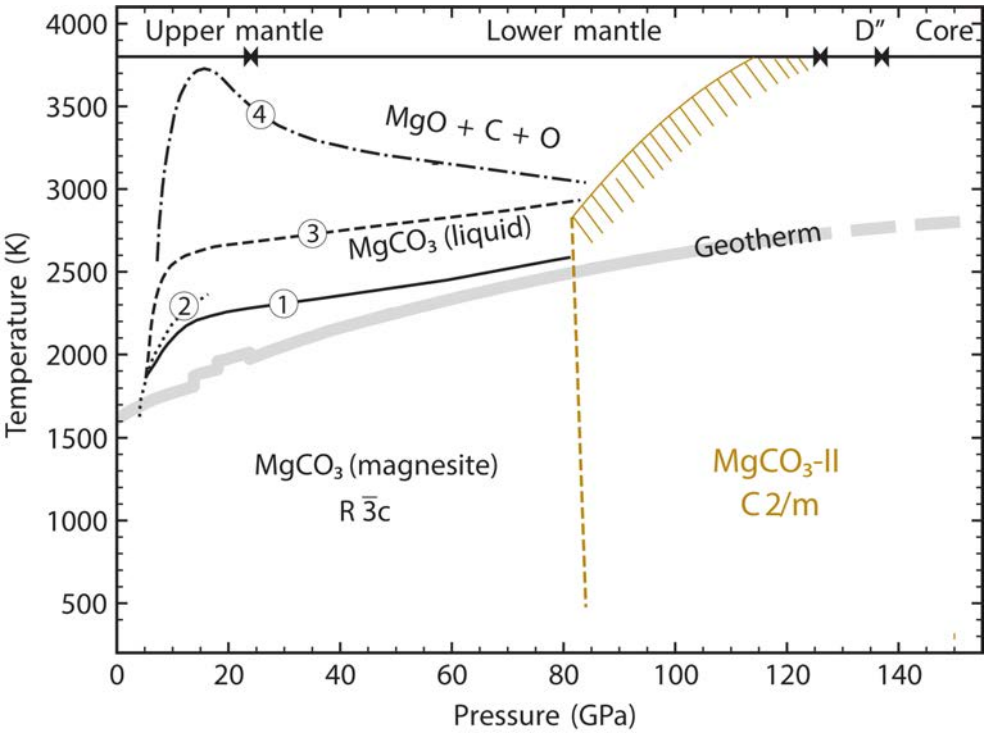


Figure 1.7: Phase relations in the $MgCO_3$ system modified after Binck et al. (2020). The dashed yellow line corresponds to the phase boundary between magnesite and magnesite-II. The gray solid line is the mantle geotherm from Katsura et al. (2010). The solid (1) and dashed (3) lines represent liquidus and decomposition for magnesite as reported by Solopova et al. (2015). The dotted line (2) represents the liquidus for magnesite as reported by Katsura and Ito (1990). The dash-dotted line (4) represents the decomposition of $MgCO_3$ as reported by Fiquet et al. (2002). The broad dashed yellow band presents a boundary above which decomposition was not observed, but solid or liquid $MgCO_3$-II.

However, magnesite may also chemically interact with basaltic crust within the subducting slab, as well as with the surrounding mantle. This requires an extension of investigations to reactions in the magnesite-silicate system. At lower mantle conditions, two binary systems containing magnesite with silicate have been investigated: the **$MgCO_3$-$MgSiO_3$** relevant for pyrolitic mantle and the **$MgCO_3$-$SiO_2$** relevant for the $SiO_2$-rich subducted basalt. Although both studied systems are iron-free and thus still very simplified, they have allowed to define the temperature limits for the stability of magnesite.

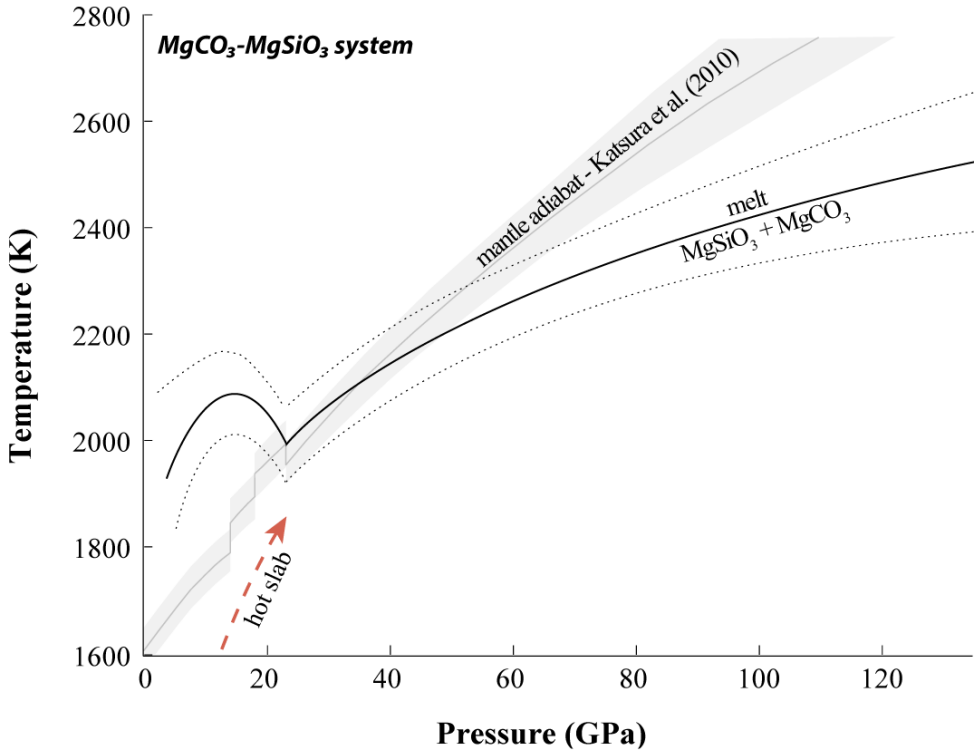


Figure 1.8: Melting curve of the $MgCO_3$-$MgSiO_3$ modified after Thomson et al. (2014), with associated 95% confidence intervals (gray dotted lines). Thick gray line: mantle adiabat from Katsura et al. (2010) and hot subducting slab (gray arrow) from (Syracuse et al., 2010)

Investigations of the **$MgCO_3$-$MgSiO_3$ system** were first reported by Katsura and Ito (1990) using multi-anvil experiments between 8 and 15 GPa and temperature up to 2100 °C and at 26 GPa at 1600 °C. Later, Thomson et al. (2014), explored this system further using laser-heating diamond anvil cell experiments and in situ melting criteria such as plateau in temperature vs laser power curve (Lord et al., 2009, 2010; Asanuma et al., 2010; Fischer et al., 2013) up to ∼80 GPa. Results obtained in this study are presented in Fig. 1.8 and show that along the mantle geotherm, at pressures between ∼16 to 23 GPa the system magnesite + enstatite/bridgmanite is below the solidus. At 23 GPa, due to the ilmenite-structured $MgSiO_3$ to bridgmanite transition a cusp appears along the solidus. At pressure ≥23 GPa, the eutectic temperature increases consistently to reach 2350 K at 80 GPa, but melting will begin at ∼35 GPa, as the eutectic melting curve and the mantle geotherm cross (Fig. 1.8). In this system, only the solidus curve has been investigated, and no information is provided on the possible reaction between magnesite and bridgmanite.

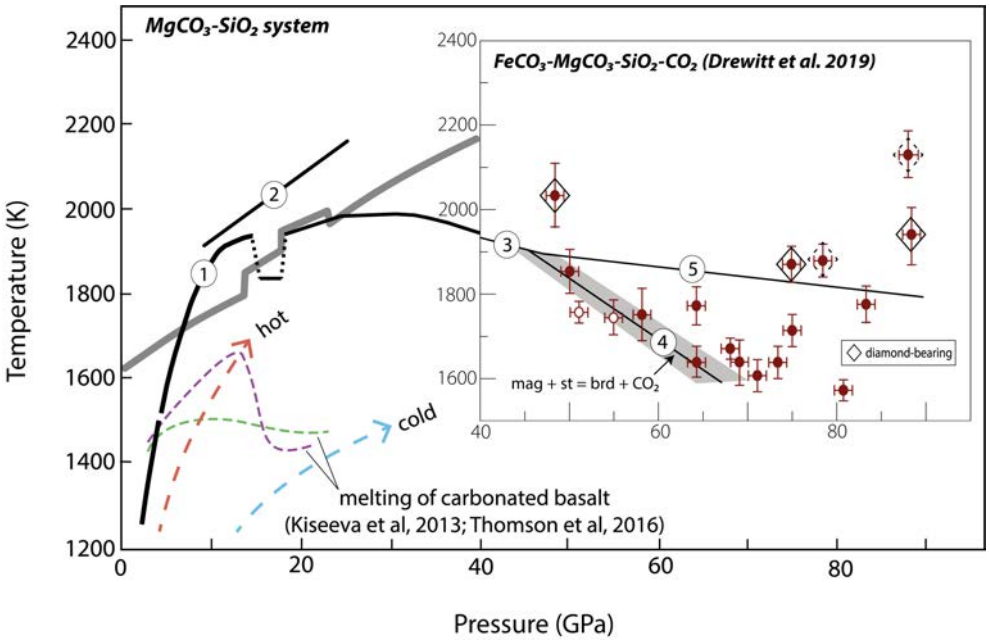


Figure 1.9: Pressure–temperature diagram showing decarbonation reaction boundaries in the $MgCO_3 + SiO_2$ and $MgCO_3 + FeCO_3 + SiO_2 + CO_2$ (FMSC) systems modified after Drewitt et al. (2019). (1) Solidus curve of the $MgCO_3$-$SiO_2$ modified after Litasov and Shatskiy (2019), and (2) Kakizawa et al. (2015) from 4–26 GPa. (3) magnesite + stishovite = bridgmanite + diamond + $O_2$ (4) magnesite + stishovite = bridgmanite + $CO_2$ (5) $CO_2$-V = diamond + $O_2$. The melting curves of carbonated MORB are from Kiseeva et al. (2013) (green curve) and Thomson et al. (2016a) (purple curve). The gray line is the mantle adiabat from Katsura et al. (2010), and hot and cold model geotherms at the surface of subducted oceanic crust from Syracuse et al. (2010).

Numerous experimental studies have investigated the **$MgCO_3$-$SiO_2$** system (Johannes, 1969; Haselton et al., 1978; Koziol and Newton, 1995; Takafuji et al., 2006; Litasov et al., 2008; Seto et al., 2008; Kakizawa et al., 2015; Maeda et al., 2017; Litasov and Shatskiy, 2019; Drewitt et al., 2019). The solidus curve was studied in a broad range of pressure from 0.2 to 32 GPa (Johannes, 1969; Haselton et al., 1978; Koziol and Newton, 1995; Litasov et al., 2008; Kakizawa et al., 2015; Litasov and Shatskiy, 2019) (Fig. 1.9). At pressure above 25 GPa, the eutectic melting temperatures in Kakizawa et al. (2015); Litasov and Shatskiy (2019) differ with: 2275 K (2000 °C) at 26 GPa in Kakizawa et al. (2015) and at 2000 ± 50 K at 28 GPa in Litasov and Shatskiy (2019). The composition of the eutectic in these studies however is close, with 96 mol% of $MgCO_3$ at 26 GPa (Kakizawa et al., 2015) and 91 mol% of $MgCO_3$ at 28 GPa (Litasov and Shatskiy, 2019). In Litasov and Shatskiy (2019), the formation of stishovite has been reported due to the incongruent melting of bridgmanite, which reacts with the carbonate–silicate melt forming stishovite, although this reaction was not detected in Kakizawa et al. (2015). The decomposition of magnesite in the pres-

ence of $SiO_2$ has been reported at lower mantle conditions from using laser-heating diamond anvil cell experiments from 26 to 152 GPa (Takafuji et al., 2006; Seto et al., 2008; Maeda et al., 2017; Drewitt et al., 2019) by the following reaction: $MgCO_3 + SiO_2 \rightarrow MgSiO_3 + CO_2$ and $MgCO_3 + SiO_2 \rightarrow MgSiO_3 + C$. These results proposed one of the possible mechanisms of super-deep diamond formation in the lower mantle. The most recent investigation by Drewitt et al. (2019), presented in Fig. 1.9, in the $MgCO_3 + FeCO_3 + SiO_2 + CO_2$ system (FMSC) showed that the deepest depths in which magnesite is stable in contact with silicates is at mid-lower mantle depths (∼65 GPa) under very cold subduction geotherm conditions (∼1600 K) before decomposing in the absence of melting and forming diamonds.

Both of these systems provide valuable information on the stability of magnesite at lower mantle conditions. However, most of them have primarily considered simplified iron-free systems with magnesite reacting with free $SiO_2$. Even in studies where iron has previously been included in the experimental system (e.g., Drewitt et al. (2019)) its potential to influence redox-sensitive phases such as carbonates remains unclear. Surviving subducted solid carbonates entering the lower mantle (≥660 km) will inevitably be in contact with a metal-saturated environment, as the lower mantle is expected to contain an average of ∼1 wt% metallic-Fe ($Fe^0$) (Frost and McCammon, 2008) (see above section 1.1.3. Therefore the nature of the carbon-bearing phase, whether oxidized as carbonate or carbon-rich melt or whether reduced and immobile form as graphite or diamond, in the lower mantle depends primarily on the redox conditions. In an effort to model such redox interactions, experimental investigations of the $MgCO_3 + Fe^0$ reaction were conducted at lower mantle conditions, revealing that magnesite's redox-breakdown is a viable sub-solidus mechanism to form diamonds via the reaction: $MgCO_3 + 2\,Fe \rightarrow C + MgO + 2\,FeO$ (Dorfman et al., 2018; Martirosyan et al., 2019; Zhu et al., 2019). These observations show how important experimental studies investigating carbonate's physical and chemical behaviors in multi-component and nature-like systems under controlled pressure, temperature, and $fO_2$ is a necessity to better constrain the fate of subducted magnesite in the deep mantle.

## 1.3 Dissertation outline

In the last decade, with the support of the Deep Carbon Observatory (DCO) community, a great number of studies have been published, aiming to better constrain the distribution, movements, and stable forms of carbon in the different Earth's reservoirs. Assuming that carbonate minerals are the major phases to transport carbon into the deepest Earth reservoirs through subduction, their physical and chemical interaction at high-pressure and high-temperature is essential to better constrain the carbon flux to the Earth's lower mantle and deeper. To investigate minerals' physical and chemical behavior at conditions of the Earth's deep interior, it is necessary to simulate and maintain the extreme pressures and temperatures achieved at these depths. High-pressure and high-temperature techniques used in this dissertation are presented in Chapter 2, with the different analytical measurements performed to examine the run product from the experiments.

Chapter 3 presents the main work of this thesis. Magnesite's stability was investigated in co-existence with an iron-containing lower mantle assemblage at shallow to mid-lower mantle conditions from 25 to 73 GPa and temperatures covering all subduction geotherms (1300 K to 2000 K) using a combination of multi-anvil apparatus and laser-heated diamond anvil cell experiments. Processes such as melting, sub-solidus decarbonation, and diamond formation in which Fe is likely to play a crucial role were examined. The experimental results obtained are used to re-assess the fate of subducted magnesite in the lower mantle and the carbon storage in the deep mantle.

Chapter 4 presents the work that conceived a portable and versatile laser heating system available at the University of Potsdam and a new technical advancement allowing imaging with reflecting optics, and radiospectrometric temperature measurements. This new development reconciles the on-axis laser heating and reflective objectives at synchrotron facilities, but also provides a great economical alternative for laboratory laser heating systems to access more accurate temperature measurements free of spectral distortion. The work carried out in this chapter contributes to the discussion of one of the key challenges in laser heating systems and possible improvements. Ultimately, Chapter 5 summarizes the thesis's outcome in the context of the current geoscientific debate and presents some considerations that need to be taken into account for potential future research drawn from the results from this work.

# 2 Experimental and analytical methods

As part of this thesis, a total of 9 multi-anvil experiments (5 successful) and 37 laser-heated diamond anvil cell experiments (LH-DAC) (20 successful) were performed. A broad range of analytical methods was used in order to investigate the run products of these experiments, including scanning electron microscopy (SEM), electron probe microanalysis (EPMA), field electron gun-EPMA (FEG-EPMA), in situ X-Ray diffraction (XRD) at synchrotron facilities, Raman spectroscopy, Focused Ion Beam (FIB) and transmission electron microscope (TEM). This chapter provides a summary of the different experimental setups and analytical techniques employed to investigate run products after high-pressure (HP) and high-temperature (HT) experiments.

## 2.1 Starting materials

To investigate the magnesite-silicate interaction, a mixture of natural magnesite ($Mg_{0.99}Ca_{0.01}CO_3$) (with <0.5% of trace elements) and silicate starting material was used for our experiments. Synthetic silicate glass was used in most of the experiments, as well as natural olivine $(Mg, Fe)_2SiO_4$ in two of the LH-DAC experiments. The synthetic silicate-glass composition was purposefully designed to reflect the composition of the major lower mantle mineral bridgmanite (see section 1.1.2). The bridgmanite analog was preferred over a basaltic (or MORB) composition because of its simpler chemical composition. To obtain a chemically homogeneous starting material, glasses are often favored. However, the production of Mg-rich glass can be difficult using conventional methods due to the very fast crystallization rate during quenching of olivine-bearing melts (Richet et al., 1993). Consequently, to avoid crystallization and to vitrify such glasses, an extremely high cooling rate is necessary.

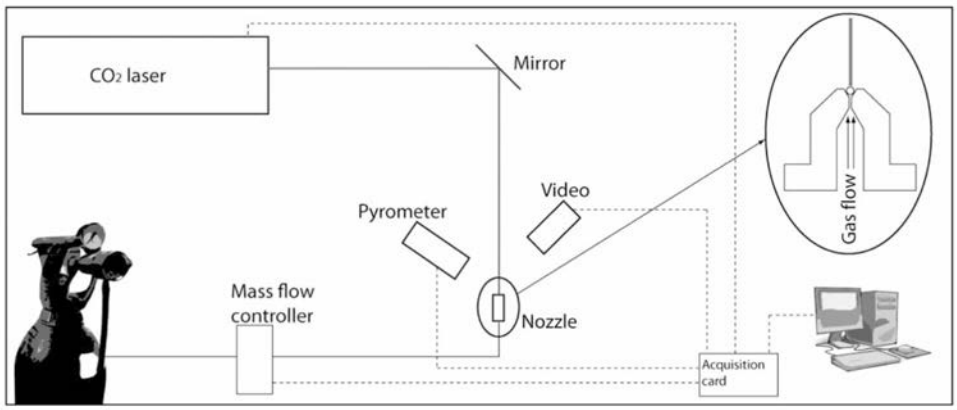


Figure 2.1: Schematic description of the aerodynamical levitation system taken from (Auzende et al., 2011). Further descriptions can be found in Hennet et al. (2002).

The aerodynamical levitation method is recognized to be an excellent way to synthesize such volatile-free glasses (Hennet et al., 2002; Auzende et al., 2011). This device consists of a nozzle enabling the levitation of a sample bead in a gas stream, to counteract gravity (Fig. 2.1). The choice of the levitating gas mixture allows control of the atmosphere during synthesis. Heating is accomplished by a 125 W $CO_2$ laser-focused on the sample by mirror giving a 1 mm spot size, and temperature is measured by an optical pyrometer. A rapid quench is obtained by turning off the laser power, after holding high-temperatures for a few minutes to allow mixing within the molten sample.

Our synthetic silicate glass was synthesized with the aerodynamic levitation system at the ICMN (Orléans, France) by Dr. Louis Hennet. Normal argon (2-3 ppm $O_2$) was used as levitating gas, to assure a reducing atmosphere and to minimize the amount of ferric iron ($Fe^{3+}$) in the glass. In addition, following the former idea of investigating the elemental redistribution of trace elements between magnesite and silicates in our experiments, three silicate glasses were synthesized with the same major elements composition but doped with either Sr, La or Eu (∼5600 ppm, ∼4000 ppm, and ∼5500 ppm respectively, Table 2.1) added using $SrCO_3$, $Eu_2O_3$and $La_2O_3$ powder respectively. The recovered samples were obtained in the form of glass balls of ∼1.5 mm diameter.

| | **glass** | **glass:Sr** | **glass:La** | **glass:Eu** | **olivine** | **magnesite** |
|---|---|---|---|---|---|---|
| **$SiO_2$** | 55.51(0.30) | 57.47(0.36) | 58.55(0.35) | 55.11(0.23) | 40.87(0.18) | - |
| **$Al_2O_3$** | 0.42(0.03) | 0.45(0.03) | 0.45(0.04) | 0.42(0.03) | - | - |
| **FeO** | 13.71(0.28) | 13.48(0.36) | 12.04(0.33) | 13.16(0.37) | 8.19(0.10) | 0.05(0.03) |
| **MgO** | 29.37(0.24) | 27.40(0.23) | 27.85(0.36) | 29.88(0.27) | 49.10(0.21) | 46.95(0.56) |
| **CaO** | - | - | - | - | 0.06(0.00) | 0.92(0.32) |
| **MnO** | - | - | - | - | 0.12(0.02) | 0.01(0.01) |
| **$CO_2$** [a] | - | - | - | - | - | 51.97(0.37) |
| **SrO** | - | 0.67(0.07) | - | - | - | - |
| **$La_2O_3$** | - | - | 0.48(0.07) | - | - | - |
| **$Eu_2O_3$** | - | - | - | 0.64(0.08) | - | - |
| **Total** | 99.01 | 99.53 | 99.43 | 99.27 | 99.04 | |
| **Si** | 1.00 | 1.02 | 1.03 | | 1.01 | - |
| **Al** | 0.01 | 0.01 | 0.01 | | - | - |
| **Fe** | 0.21 | 0.2 | 0.18 | | 0.17 | 0.00 |
| **Mg** | 0.79 | 0.73 | 0.73 | | 1.80 | 0.99 |
| **Ca** | - | - | - | - | 0.00 | 0.01 |
| **Mn** | - | - | - | - | 0.00 | 0.00 |
| **C** | - | - | - | - | - | 1 |
| **Sr** | - | 0.01 | - | - | - | - |
| **La** | - | - | 0.0 | - | - | - |
| **Eu** | - | - | - | 0.0 | - | - |

Table 2.1: Upper table: Starting composition silicate starting materials measured at the EPMA (wt%). Glass correspond to the $(Mg, Fe)SiO_3$ analogue. [a]Calculated from the total deficit from the analyses. The numbers in parentheses next to the measurement refer to the standard deviation ($1\sigma$). Lower part: Cations per formula unit are calculated on the base of 3 oxygens for magnesite and silicate glass and 4 oxygens for olivine.

| | MG11 | MG13 | MO11 |
|---|---|---|---|
| Composition | Mgs + glass | Mgs + glass | Mgs + olivine |
| Ratio | 1:1 | 1:3 | 1:1 |
| $MgCO_3$ (mol%) | 51.75 | 26.34 | 48.25 |
| silicate glass (mol%) | 48.25 | 73.66 | - |
| olivine (mol%) | - | - | 36.52 |

Table 2.2: Starting composition (mol%). Mgs= magnesite

In total, three magnesite-silicate mixtures were used as starting materials: MG11 (when Sr or La was added it is referred to as MG11:Sr, and MG11:La), MG13, and MO11 (Table 2.2). In MO11, approximately 10 wt.% of Pt-black (platinum powder) was added to the mixture to serve as laser coupler (see section 2.2.2). All starting materials were powder mixtures, ground in an agate mortar with acetone for 20 min to achieve homogenization and to assure a grain size <5 $\mu$m. To minimize water absorption, the starting material mixtures were stored in an oven at 120 °C prior to the experiment. All starting materials were nominally $H_2O$-free, nevertheless minor adsorption of water during the preparation of experiments is unavoidable. The starting materials were characterized in composition and homogeneity using electron probe microanalysis (EPMA) (see section 2.3.2). The chemical compositions of the samples are available in the following Tab. 2.1. In the appendix A.1, a description of several attempts of not used starting materials is provided.

## 2.2 High-pressure experiments

To investigate the physical and chemical behavior of material inside Earth's and planetary interiors, bringing materials to high-pressure (HP) and high-temperature (HT) experiments is essential. Over the last decades, experimental devices and techniques have been developed and improved to better simulate the extreme conditions expected within planetary bodies. HP experiments reside on the ability to reproduce these very high-pressures in laboratory facilities. Pressure (P) is defined as the amount of force (F) applied on the surface of an object by the unit of area (A) such as $P = \frac{F}{A}$. The increase of pressure can either be done by increasing the force applied or by decreasing the area, which will directly impact the sample size.

Each high-pressure apparatus have its own advantages and unique applications. Large-volume press devices such as multi-anvil presses (MAP) allow for static compression of a relatively large sample (mm to cm), a quasi-hydrostatic pressure environment, a uniform temperature field, and precise control of pressure and temperature gradient throughout the sample. MAP can simulate pressures and temperatures from the upper mantle to mid-lower mantle pressure, with the highest pressure reported are: for tungsten carbide (WC) anvil up to 65 GPa, at room temperature and 48 GPa at 2000 K (Ishii et al., 2017) and up ∼120 GPa (at room temperature) using sintered diamond anvils (Yamazaki et al., 2019). However, those pressure ranges are still not available commonly and most of the MAP does not get at more than 26 to 28 GPa routinely. To bring samples routinely to higher pressures, such as the ones relevant from the lower mantle to the core ($\geq$ 25 GPa), experiments need to be miniaturized to fit in the micrometer sample chamber of the diamond anvil cell (DAC) apparatus. One of the most valuable aspects of DAC comes from the transparency windows offered by the diamond anvils, allowing in situ investigations of phase transition and physical properties at HP and HT using spectroscopy techniques.

### 2.2.1 Multi-anvil apparatus

The multi-anvil experiments presented in this thesis (Chapter 3) were carried out using the 1000-tonne (Hymag) or 1200-tonne (Sumitomo) 6–8 Kawai-type multi-anvil apparatus - first introduced by (Kawai and Endo, 1970) - at the Bayerisches Geoinstitut (BGI, University of Bayreuth, Germany) through a project collaboration with Dr. Catherine McCammon and Dr. Serena Dominijanni. Pressurization is achieved by a hydraulic press composed of first-stage anvils forming a cubic space featuring 6 wedge-shaped, in which is placed a set of eight-corner-truncated WC cubes also called second-stage anvils (Fig. 2.2). The truncations on each tungsten carbide cube, form an inner cavity where the octahedral assembly, containing the capsule, is placed (Fig. 2.3). Pyrophyllite gaskets are placed on the edges of each truncation to support the truncation and seal the high-pressure region to create a quasi-hydrostatic pressure on the sample.

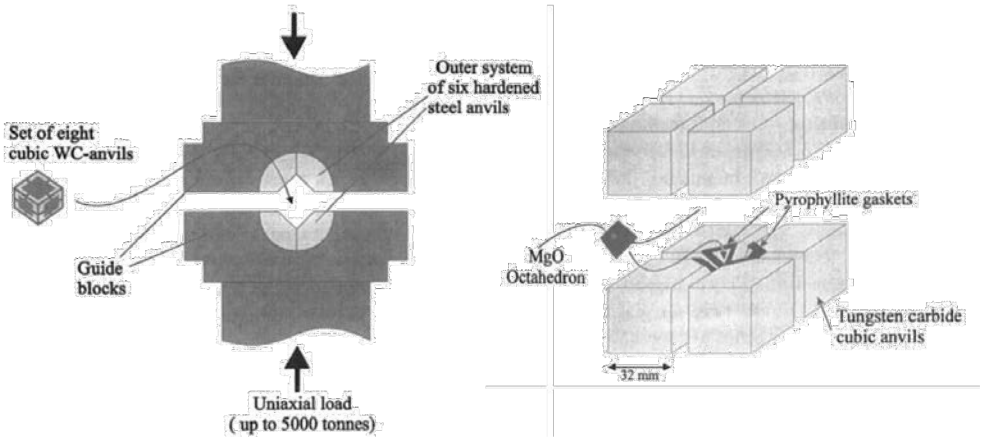


Figure 2.2: Details of the 6-8 type multi-anvil apparatus taken from Rubie (1999). Two steel guide blocks containing the six first-stage anvils guided together by the hydraulic press (left), will compress a set of eight tungsten carbide (WC) inner anvils, containing the octahedral assembly (right). Pyrophyllite gaskets are attached on the edge surrounding the truncations of the WC anvils.

MAPs can achieve commonly a wide range of pressure (3 to 28 GPa), by varying the truncation edge length (TEL) and the octahedral edge length (OEL). The assembly size is described by this relation OEL/TEL, e.g., 14/8 assembly, employs a 14 mm OEL with an 8 mm TEL reaching up to 16 GPa using a 1000-tonne press at BGI. In this thesis, a 7/3 cell assembly configuration was used to reach 25 GPa. The starting material mixtures were contained in a folded rhenium capsule of ∼0.8 diameter and ∼1 mm length. The capsule was placed in the center of a layered sleeve composed of a layer of MgO and the $LaCrO_3$ furnace. Two MgO spacers were positioned above and below the capsule to keep it in the center. Everything was contained in an octahedral assembly made of $Cr_2O_3$-doped MgO acting as a pressure medium. To prevent heat dissipation through the WC anvils, which would increase anvil breakage, a $ZrO_2$ lining is placed between the furnace and the assembly for thermal insulation. A schematically illustrated cross-section of the assembly is presented in Fig. 2.3.

High-temperatures were achieved for 1 to 2 hours by running an electrical current through the $LaCrO_3$ semi-conductive furnace. The temperature was kept constant within ∼20 °C and monitored using either a D-type ($W_{97\%}Re_{3\%}$-$W_{75\%}Re_{25\%}$) thermocouple placed horizontally through the wall of the furnace in direct contact with the capsule, or in the case of thermocouple failure, by using the heating power (W) vs temperature (°C) calibration from the presses obtained from previously performed similar experiments with an accuracy of ±100 °C. The samples were quenched by switching off the electrical power and decompressed overnight (∼15 hours). Pressure and temperature uncertainties are estimated at ±1 GPa and ±100 K (Rubie, 1999;

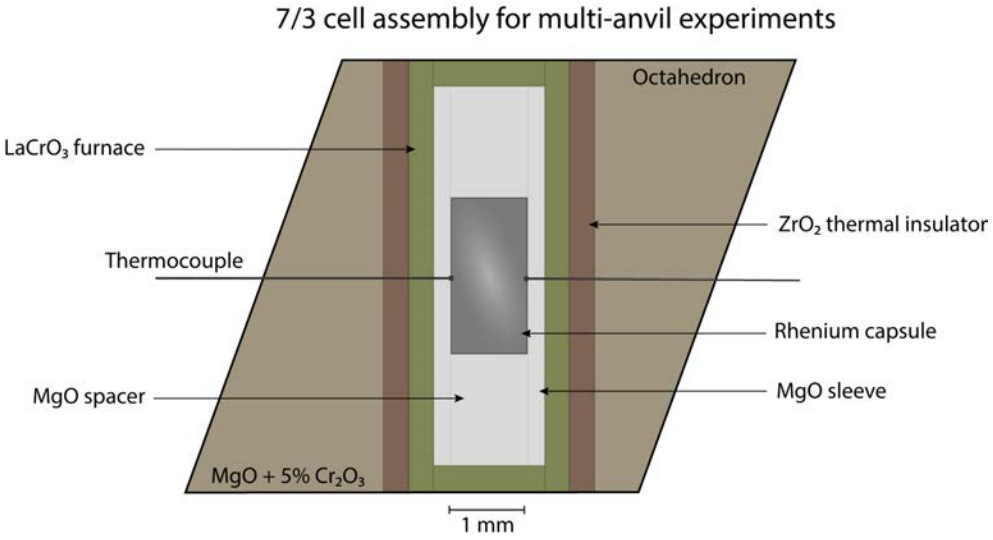


Figure 2.3: Schematic cross-section of a standard 7/3 cell assembly for multi-anvil experiments.

Keppler and Frost, 2006). More details on the calibration specificity of BGI's multi-anvil presses can be found in Rubie (1999); Frost et al. (2004); Keppler and Frost (2006).

### 2.2.2 Laser-heated diamond anvil cell

The diamond anvil cell (DAC) technique was first introduced by Weir et al. (1959) and is still today the only HP device capable of generating static pressures up to 1 TPa (Dubrovinskaia et al., 2016), reproducing the entire pressure range of Earth's interior, and larger planetary bodies (Mao et al., 1990). Several DAC designs exist, reflecting the broad range of applications and measurements possible. The two most commonly used are the piston types e.g., Mao Bell type Mao and Bell (1977), and the plate types e.g., Merrill–Bassett-type (Merrill and Bassett, 1974) or standard-plate type from Boehler (2006). Although designs and operating systems can differ, the basic principle is very similar. High-pressure is achieved by uniaxially compressing two flattened (culet) gem-quality diamond anvils coaxially aligned. The pressure range achievable is directly linked to the diameter of the culet. The higher the target pressure is, the smaller the culet's size needs to be, affecting at the same time the sample size. The sample is contained within a chamber drilled in a gasket, that has been pre-indented to a thickness generally $\sim$25 $\mu$m. The gasket materials can vary depending on the target pressure such as steel, tungsten, or rhenium, but also

depending on the measurement techniques. X-ray transparent beryllium gasket is used when the incident X-ray beam needs to pass through the gasket as for some X-ray Raman spectroscopy techniques.

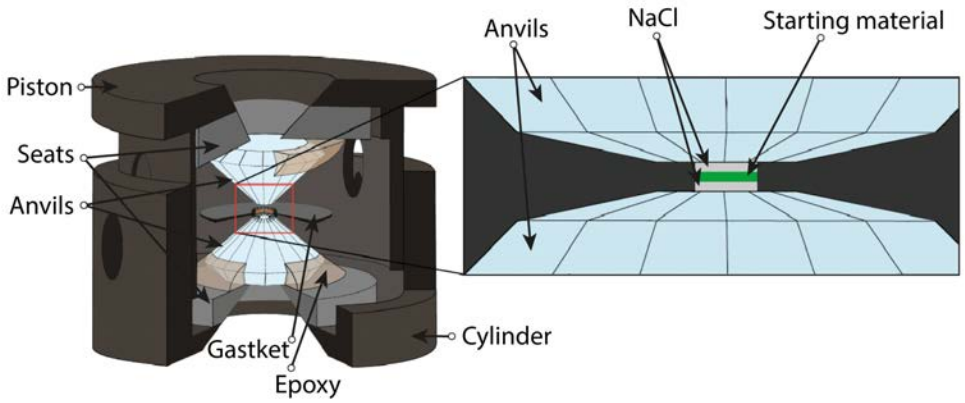


Figure 2.4: Cartoon sketch of a BX90 type diamond anvil cell modified after Shen and Mao (2016)

In this work (Chapter 3), we used screw-driven BX90 diamond anvil cells developed by Kantor et al. (2012) with 70° Bohler-Almax (Boehler and Hantsetters, 2004) diamond anvils and seats (Fig. 2.4). This DAC design gives a wide axial opening angle that is the most suitable to perform single and powder X-ray diffraction. To reach pressure simulating the ones from the Earth's lower mantle, culet sizes of 300 to 200 $\mu$m were used. The sample chamber of 80 to 130 $\mu$m diameter - depending on the culet size - was drilled in rhenium gaskets after a pre-indentation to a thickness of 35 to 45 $\mu$m, allowing to load of the sample plus a pressure medium. The sample consisted of 15 to 20 $\mu$m thick compressed platelets of the starting material, sandwiched between two NaCl layers (Fig. 2.4). NaCl was used as a pressure medium and thermal insulator, permitting quasi-hydrostatic conditions and preventing non-homogeneous strains. Other commonly used pressure media are inert gas e.g., argon, neon, and helium as well as solid phases e.g., KCl, MgO, or NaCl.

### Pressure measurements

Pressure measurement in DAC experiments rely on the use of calibrated standard phases. The most common one consists in measuring the R1 fluorescence wavelengths of a small crystal ruby (Piermarini et al., 1975; Mao et al., 1986; Chijioke et al., 2005) placed in the sample chamber and excited by a visible laser. Other internal standard phases can be used e.g., Au or Pt (Holmes et al., 1989), as well as the material used

as pressure media i.e., NaCl (Dewaele et al., 2004; Ono et al., 2006; Fei et al., 2007; Sakai et al., 2011; Dewaele, 2019) by measuring the change of volume with in situ X-ray diffraction (see 2.3.1) and fitting it to its equation of state (EOS).

In the present work, to limit contamination and/or possible reaction between pressure standard and the sample, as well as the number of peaks during X-ray diffraction (XRD) measurements (see Section 2.3.1) no internal pressure standard was used. Instead, the pressure was evaluated using the shift of the diamond Raman peak from the diamond anvil at the culet surface (Hanfland et al., 1986) using the quasi-hydrostatic calibration scale from Akahama and Kawamura (2006). This technique relies on the correlation between the first-order Raman band position and the stress at the culet surface of the diamond anvils following the analytical expression:

$$P(GPa) = K_0 \frac{\Delta\upsilon}{\upsilon_0} \left[1 + \frac{1}{2}(K_0' - 1)\frac{\Delta\upsilon}{\upsilon_0}\right] \tag{2.1}$$

with $\Delta\upsilon$ is the wavenumber measured from the high frequency edge, $\upsilon_0$ represent the edge frequency at ambient P ($\upsilon_0$ =1334 ±1 $cm^{-1}$), $K_0$ is the bulk modulus and $K_0$' is it derivative of a hydrostatically compressed elastic material; $K_0$ = 547(11) GPa and $K_0$' = 3.75(20). The estimated error from the calibrated scale of Akahama and Kawamura (2006) is ±2 GPa below 250 GPa.

Pressures were routinely measured before and after heating using Raman spectroscopy (see Section 2.3.1). Pressure measured from the NaCl medium differed by ±2 GPa from the diamond anvil post-heating pressure. An increase of pressure is expected during heating (thermal pressure) (Fiquet et al., 1996; Andrault et al., 1998), and can be estimated to be about 10% higher than the pre-heating pressure (Fiquet et al., 2010). However, considering the modest temperatures achieved in this study (1300 K to 2100 K), no corrections were made for thermal pressure. The pressures reported in this work are the ones after heating and are within <4% of the pre-heating pressure.

**Laser-heating**

To reach high-temperatures in DAC two heating methods can be used: (1) the resistive heating method by building a heater inside the sample chamber or (2) using a laser heating (LH) system. The laser-heated (LH) diamond anvil cell (DAC) technique,

since its introduction in the 1970s (Ming and Bassett, 1974), and is often preferred for HT, since the resistive heating technique is only possible at temperatures under 1200 K, limiting its applications for planetary interiors (Duffy, 2005). The LH methods commonly employ solid-state near-infrared (NIR) laser beam ($\lambda$= ~1.064 $\mu$m) to heat metallic, semiconducting materials and Fe-bearing samples. Heating is achieved due to the interaction between the photons of the laser and the free (or bounded) electrons of the materials, causing the electrons in the conduction band to enter higher energy states. The collision of these excited electrons with lattice phonon creates the thermal energy (Salamat et al., 2014; Smith et al., 2018; Anzellini and Boccato, 2020). Fe-free samples or wide-bandgap materials (i.e., that have a larger energy range (≥2 eV) in which no electronic states can exist than conventional semiconductors (0.6 to 1.5 eV)), can be difficult to heat with solid-state lasers due to their low absorption of NIR radiation. A common practice to overcome this problem is to mix a (metallic) laser absorber directly into the sample e.g., inert metallic foils with high melting points such as black platinum (Pt powder) or gold. Thereby, it provides indirect heating to non-absorbing samples.

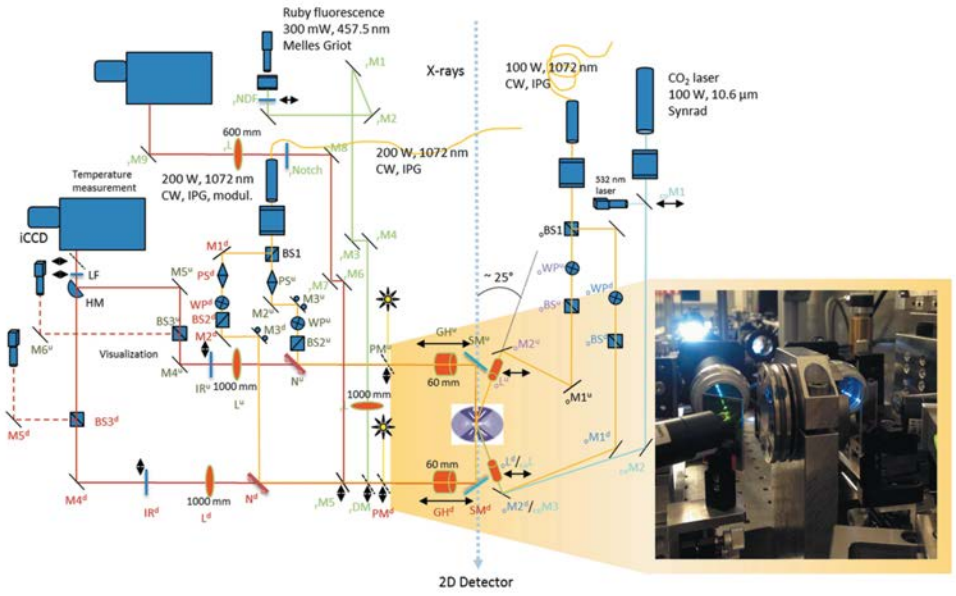


Figure 2.5: Sketch of the laser heating systems (NIR and $CO_2$) at the Extreme Conditions Beamline at PETRA III at DESY, Hamburg taken from Konôpková et al. (2021). Superscripts 'd' and 'u' refer to 'downstream' and 'upstream', respectively. Subscript 'r' denotes the ruby fluorescence part, 'o' the off-axis path, and 'co' the $CO_2$ laser path. SM – Semrock mirror, GH – geoHEAT, DM – dichroic mirror for 457 nm, N – dichroic mirror for 1072 nm, L – lens, IR – laser filter, M – mirror, BS – beamsplitter, WP – waveplate, PS – Shaper.

Alternatively, the use of $CO_2$ gas lasers ($\lambda$= ~10.6 $\mu$m), permits direct coupling with the material. Their wavelength is in the same order as the lattice phonon in covalent crystals and can be absorbed by existing lattice vibrations, and the resulting vibration develops thermal energy (Smith et al., 2018; Anzellini and Boccato, 2020). The long wavelength and the absorption mechanism of $CO_2$ laser contribute to other advantages: they provide a larger focused spot (~50 $\mu$m diameter), and more uniform heating throughout the entire thickness of the sample. Unlike NIR lasers, for which the laser radiations are primarily absorbed in the sample's surface, resulting in a smaller focused spot, typically of 15 to 30 $\mu$m diameter (Salamat et al., 2014). This also creates a significant axial and radial thermal gradient when using NIR lasers. To minimize the axial temperature gradient double-sided laser heating systems are now used in laboratories and synchrotron facilities. To minimize the radial temperature gradient a focal $\pi$-shaper is often implemented, that converts the shape of the Gaussian intensity distribution of the focused laser beam into a flat-top spot focused beam (similar to a Greek letter $\pi$) (Laskin and Laskin, 2011; Prakapenka et al., 2008).

LH of our DAC experiments was achieved by using a double-sided YAG fiber laser emitting at 1072 nm and a spot size of 20 $\mu$m (FWHM) (Konôpková et al., 2021) installed at the Extreme Conditions Beamline (ECB) (Liermann et al., 2015) at the PETRA III in Hamburg (Germany) (Fig. 2.5). The temperature was held stable for 5 to 55 minutes, after which the sample was quenched by turning off the laser emission. State-of-the-art, NIR laser heating systems employing as Nd:YAG, Nd:YFL or Yb-doped fiber laser are well suited for minutes to hours-long DAC heating (Prakapenka et al., 2008). The stability of laser heating samples depends, among other factors, on the stability of laser light, the homogeneity of absorption by the samples, and the good insulation of the heated sample from the highly thermally conductive diamonds.

### Temperature measurements

The heating temperature is generally determined radiospectrometrically (Campbell, 2008) from the emitted thermal signal, collected from the center of the heating spot on both sides of the sample. The spectra obtained are used to calculate the temperature by fitting the thermal signal emitted I($\lambda$,$\epsilon$,T) to Planck's law with a gray-body distribution:

$$I(\lambda, \epsilon, T) = \epsilon \frac{2\pi hc^2}{\lambda^5} \frac{1}{\exp\left(\frac{hc}{\lambda k_B T}\right) - 1} \tag{2.2}$$

where h is the Planck constant, c the speed of light, $k_B$ the Boltzmann constant, T the temperature corresponding to the collected radiation, and $\lambda$ the wavelength of the measured emitted signal. The emissivity ($\epsilon$) is wavelength-dependent, but its variation can be considered negligible when the gray-body approximation ($\epsilon$<1) is assumed. To obtain a reliable temperature measurement, the spectrometer needs to be calibrated, by collecting the radiated intensity of a tungsten lamp of known temperature placed at the DAC position. In addition, filters such as band-pass, notch, and/or neutral density filters can be added before the spectrometer to filter parasitic signals from the laser or to attenuate the emitted light during high-temperatures that could saturate the detector.

The temperatures reported in this work were determined in the spectral range from 640 to 850 nm and fitted using the software T-Rax by C. Prescher (github.com/CPrescher/T-Rax). The temperatures reported in our LH-DAC experiments are temporal averages of the temperature measurement series over the heating duration. Temperature uncertainties at ECB are estimated to be in the order of 10% of the temperature value (Konôpková et al., 2021). Accurate temperature measurement is extremely important in LH-DAC experiments, but several factors are critical. A precise alignment of the laser spot and the X-ray is necessary when associated with in situ measurements. Another, widely discussed systematic error in these temperature measurements is the chromatic aberration from the objectives, diamonds, and other refractive optical components. This is presented in Chapter 4 where an alternative is proposed to drastically reduce chromatic aberration in radiospectrometric temperature measurements in both laboratories and for synchrotron LH systems.

## 2.3 Analytical methods

### 2.3.1 Phase analyses

#### Synchrotron in situ X-Ray diffraction in LH-DAC

In situ X-ray diffraction (XRD) has been routinely used to probe HP and HT phases in LH-DAC experiments. It is a non-destructive analytical technique that allows the determination of the crystal structure and phase identification and physical properties of materials. XRD is the coherent elastic scattering of X-ray photons (at a given wavelength $\lambda$) by the electrons of atoms arranged in a periodic crystal lattice. In other terms, it is the diffraction of electromagnetic radiation, such as an X-ray beam, that interacts with a crystalline material composed of atoms that are arranged in a regularly-spaced crystal lattice. The planes in the crystal lattice are separated by a specific distance (d) that can be calculated with Bragg's law such as $\lambda = 2d*sin(\theta)$ by knowing the incident and reflection angles ($\theta$) of the X-ray beam at a given wavelength ($\lambda$) (Bragg, 1914).

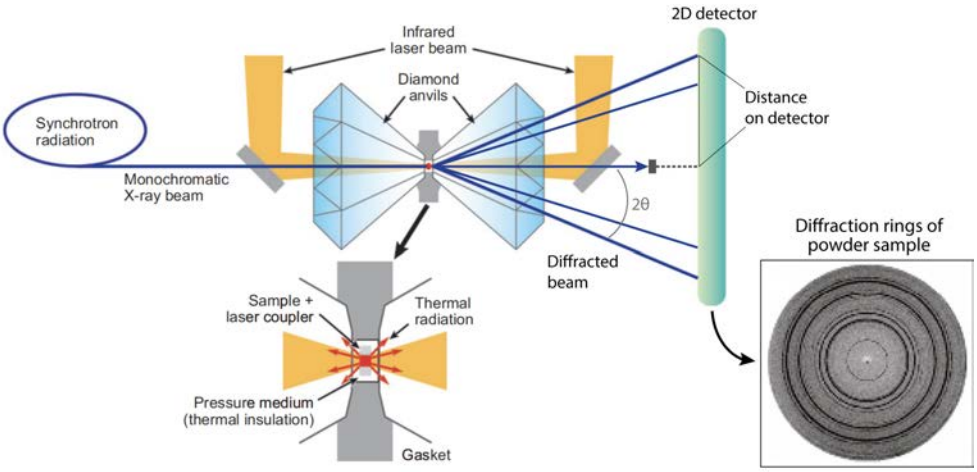


Figure 2.6: Illustration of the experimental setup for in situ angle-dispersive high-pressure powder x-ray diffraction in the laser-heated diamond anvil cell modified after (Shim, 2008). A part of the incident monochromatic X-ray beam is elastically scattered following Bragg's law. The reflection angles $2\theta$ are measured from the collected diffractograms.

In this thesis (Chapter 3), we performed powder angle-dispersive X-ray diffraction to identify the co-existing phases in the polycrystalline heated spot of our LH-DAC experiments at the Extreme Conditions Beamline (ECB) at the PETRA III, Hamburg, Germany. The monochromatic X-ray beam was focused on the sample by Kirkpatrick Baez (KB) Mirrors to 2 x 2 $\mu m^2$ FWHM) and 42.7 keV. The diffraction patterns were measured as rings on a high-resolution area detector (Perkin Elmer, XRD1621). The sample-detector distance was calibrated from the diffraction pattern of a $CeO_2$ standard material. Diffraction data were processed using Dioptas software (Prescher and Prakapenka, 2015) with which the 2D diffraction images were integrated to produce intensity vs $2\theta$ diffractograms. The detailed description of the Extreme Conditions Beamline P02.2 can be found in Liermann et al. (2015).

**Raman spectroscopy on samples recovered from LH-DAC experiments**

Raman spectroscopy is a non-destructive technique that is commonly used in geosciences for phase identification, structure, and molecular interaction. It relies on the inelastic scattering produced when monochromatic light (a laser) interacts with the vibrational modes of molecules. Most of the incident photons are elastically scattered (Rayleigh scattering), at the same frequency and wavelength as the incident laser light. Meanwhile, a small fraction of the photons interact with the vibration modes of the molecule or crystal structure resulting in an inelastic scattering, the so-called Raman scattering (Fig. 2.7). These interactions will cause either to gain or loss of vibrational energy, thus producing anti-Stokes radiation or Stokes radiation, respectively. Anti-stokes radiations show a positive Raman shift whereas stokes radiation shows a negative Raman shift (Fig. 2.7). Therefore, the differences in the Raman shifts corresponding to the frequency of the Raman-active vibrational mode in a compound can be detected.

In this work, Raman spectroscopy was specifically used to detect the presence of diamond in the recovered LH-DAC experiments (Chapter 3). A HORIBA Jobin Yvon Confocal LabRAM HR 800 equipped with a Peltier-cooled multichannel CCD detector at the University of Potsdam was used. An Nd:YAG laser with a wavelength of 532 nm (green) provided the light source to excite the sample. The slit width was set to 100 $\mu$m and the confocal pinhole to 200 $\mu$m.

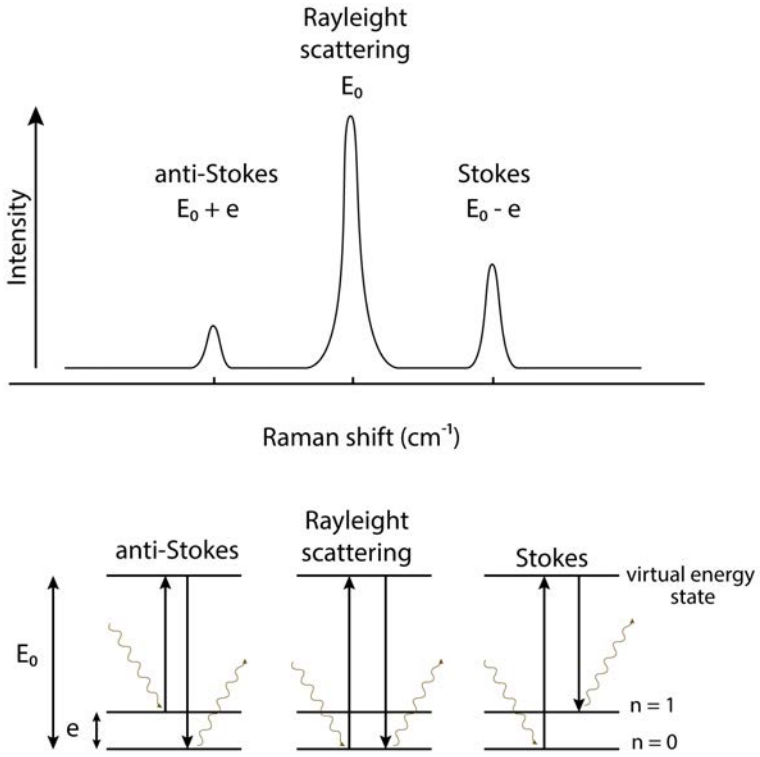


Figure 2.7: Schematic representation of energy level for elastic (Rayleigh) and inelastic (Raman) scattering and the representation as a Raman spectrum.

### 2.3.2 Chemical analyses

**Scanning electron microscopy (SEM) and Electron probe microanalysis (EPMA)**

Electron-based analytical tools such as scanning electron microscopy (SEM) and electron probe microanalysis (EPMA) are non-destructive analytical techniques based on the same operating principle. In these techniques, an accelerated and focused electron beam is generated to scan the sample. When the incident electron beam hit the sample with sufficient energy it liberates both matter and energy from the sample. The electron-sample interaction generates different signals comprising: (1) back-scattered electrons (BSE) used for imaging purposes, (2) secondary electrons (SE), and (3) X-ray emission (Fig. 2.8). The SE images inform about the topography of the sample, meanwhile, the BSE provides compositional imaging information about the sample. This is possible because heavy elements (high atomic number, Z) backscatter electrons more strongly than light elements (low Z), and the intensity contrast between phases is used to distinguish phases with different chemical compositions in the analyzed sample.

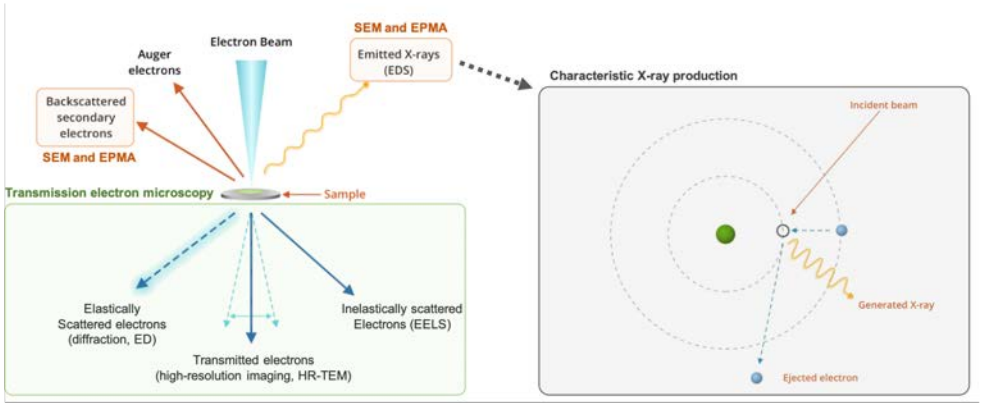


Figure 2.8: Schematic representation of the different electron beam-matter interactions. Annotated on the image the different analyses used in this thesis: SEM/EPMA and TEM with electron diffraction (ED), high-resolution transmitted (HR-TEM) and EELS. Images sourced at https://myscope.training/ and modified.

X-rays are generated by the inelastic collisions of the electron beam with the electrons in the inner shells of atoms in the sample; when an inner-shell electron is ejected from its orbit, it leaves a vacancy, then this vacancy is filled by a higher-shell electron releasing some energy, in the form of X-ray (Fig. 2.8). These emitted X-rays have specific energies depending on the element and are called characteristic X-rays, their intensities can be measured with an energy dispersive spectrometer (EDX) providing qualitative compositional information in SEM or by wavelength dispersive spectroscopy (WDS) in EPMA instruments providing quantitative chemical measurements. EPMA are commonly equipped with four or five-wavelength dispersive (WD) spectrometers. Each of them consists of a crystal with a known interplanar spacing (d) that enables detecting photons of a specific wavelength. Quantitative analysis is obtained by comparing intensities of the characteristic X-rays of standard materials with known composition. A detailed description of the method and instrumentation of SEM and EPMA can be found in Reed (2005).

In this study, SEM was used for textural observations and preliminary phase identification of recovered run products from our multi-anvil experiments (Chapter 3) using a JEOL JSM-6510 operating at 15 or 20 kV installed at the University of Potsdam. One multi-anvil experiment (#5) was analyzed using a field-emission scanning electron microscope (ZEISS Ultra Plus) installed at GFZ Potsdam, using an acceleration voltage of 20 kV. Prior to SEM/EPMA analyses samples were placed in epoxy resin, polished to expose the sample surface, and coated with carbon to prevent the accumulation of electrostatic charge at the surface during measurements. All EMPA measurements presented in this work were performed with a JEOL JXA-8200 at the

University of Potsdam with the support of Christina Günter for chemical characterization of the starting materials (section 2.1; Tab 2.1) and for chemical characterization of run product of the multi-anvil experiments (section 3.1.1). Although SEM and EPMA are commonly used techniques in Earth sciences, their use is limited when considering the very small and thin samples recovered from LH-DAC experiments, in which multiple phases coexist within a few tens of micrometers. Such samples are more often analyzed using a field electron gun EPMA/SEM (section 2.3.2 or a TEM section 2.3.2) but still necessitate a polished surface that is better achieve using FIB milling during extraction of the analytical area (section 2.3.2).

**Focused ion beam milling: Preparation of LH-DAC experiments**

Focused ion beam (FIB) milling is nowadays mainly used to prepare the recovered LH-DAC samples for nanometer scale analyses with TEM (section 2.3.2). It is especially useful for the micro-volume and very thin recovered LH-DAC experiments. The basic operational principle of a FIB instrument is to remove material with nanometer precision, by bombarding it with a highly energetic ion beam, known as 'sputtering'. The advanced technology of the dual-beam instruments combined a FIB column and an SEM column to allow simultaneous milling or deposition with high-resolution imaging respectively (Fig. 2.9). A more detailed description of the FIB techniques can be found in Wirth (2009) and in Miyahara et al. (2008) and Marquardt and Marquardt (2012) for LH-DAC experiments application.

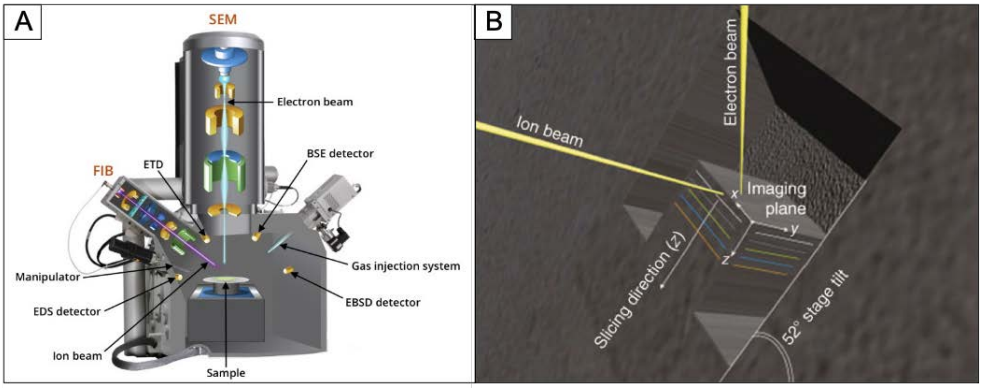


Figure 2.9: A) Schematic representation of a dual-beam FIB-SEM instrument (https://myscope.training/). B) Typical sample geometry and beam orientation during milling after Uchic et al. (2007).

The FIB preparation in this work was achieved by Anja Schreiber at the PISA facility (GFZ, Postdam), on an FEI Helios G4 UC Dual Beam using high-energy gallium ions to cut into the sample. The preparation consisted, in the first step, of drilling the sample out of their rhenium gasket with the FIB. The discs obtained of approximately 150-170 $\mu$m in diameter were glued onto an SEM holder and coated with amorphous carbon. To access the laser-heated region, the sample was sectioned parallel to the compressional axis. When the center of the heated region was revealed, a 2 $\mu$m thick Pt layer was deposited to protect the sample surface from the $Ga^+$ ion beam. FIB lamellae of about $\sim$30 $\times$ $\sim$20 (length $\times$ width) were extracted and fixed on a copper grid and then thinned. The foil's thickness depends on the analytical methods used; for FEG-EPMA analysis, a lamella of at least several micron thicknesses is required (Jennings, 2020). A thick foil of 3 microns was then analyzed by running an EDX map with FEG-EPMA and with using an FEI Quanta 3D (Dual Beam). Afterward, several foils were thinned to achieve electron transparency ($\sim$100 nm) for STEM analyses.

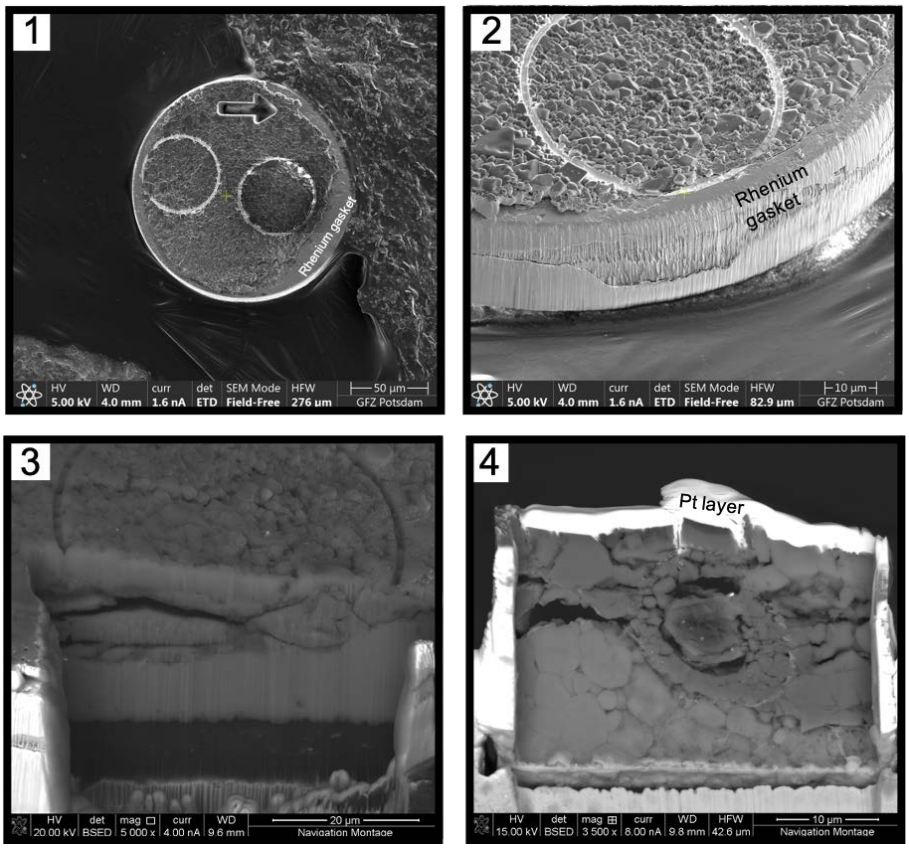


Figure 2.10: SE images displaying a typical LH-DAC recovered sample in the FIB. 1) area of interest is getting identified and marked on the NaCl surface, the arrow allows the orientation of the sample. 2) tilted view showing the side of the sample with the rest of the rhenium gasket before opening to access the heated area. 3) opening from the side. 4) FIB lamella fixed on the TEM copper grid.

### Field emission gun electron microprobe microanalysis (FEG-EPMA)

As discussed earlier (see section 2.3.2), EPMA is widely used for standardized sample size (mm to $\mu$m) but when measuring smaller samples, a field emission gun EPMA instrument is more appropriate, as the beam can be better focused. FEG-EPMA is suitable for LH-DAC samples and has been reported for LH-DAC samples in previous studies (Tateno et al., 2014; Blanchard et al., 2017; Jennings, 2020).

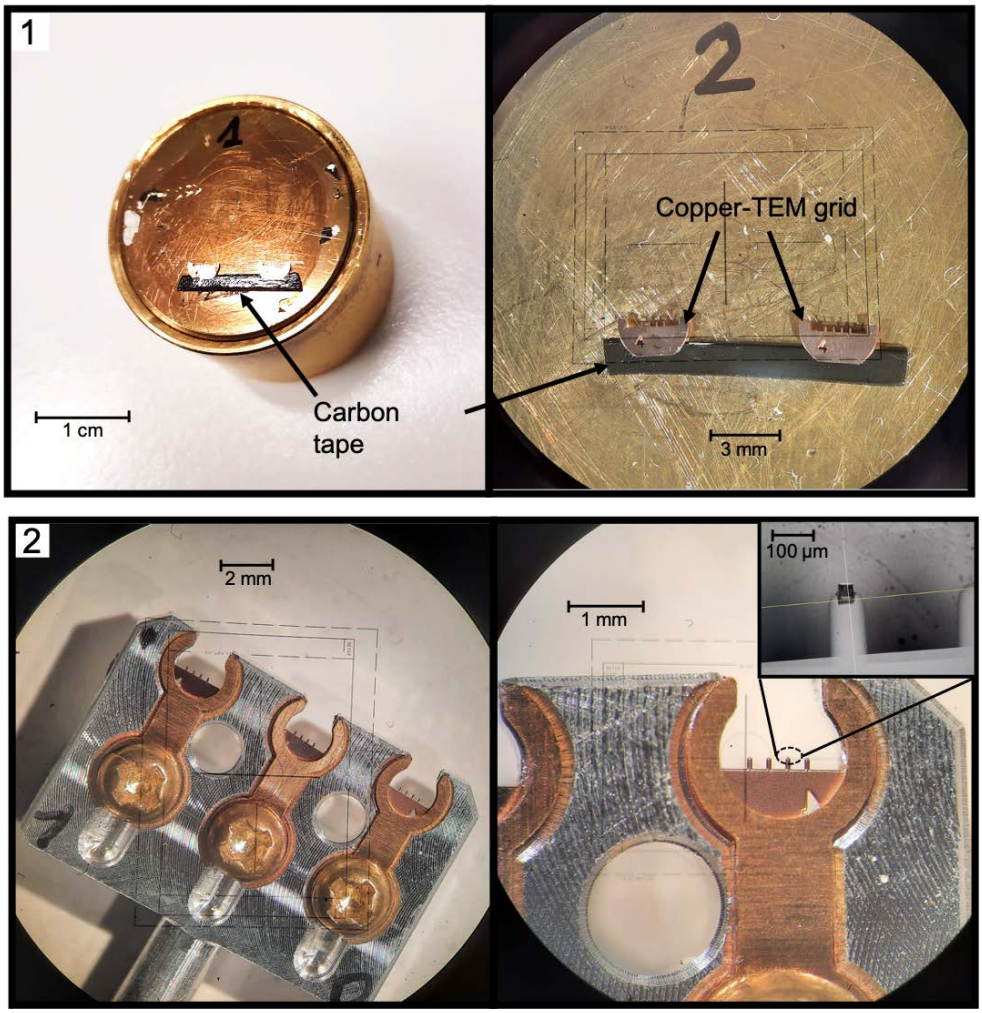


Figure 2.11: Photo of the FEG-EPMA sample holders used for measurements. (1) Copper-TEM grids are fixed on the EPMA mounts with carbon tape. (2) The FIB-EBSD sample holder containing the foils fixed on the EPMA mount.

The thick foils (>3 $\mu$m) were placed in the FEG-EPMA (JEOL Hyperprobe JXA-8530F) at GFZ Potsdam. Samples were in a copper-TEM grid that was either directly stuck on the microprobe sample holder by a piece of Carbon-tape or contained in a FIB foil holder made for the FIB-EBSD machine and then taped on the EPMA holder. No carbon coating was used for these measurements.

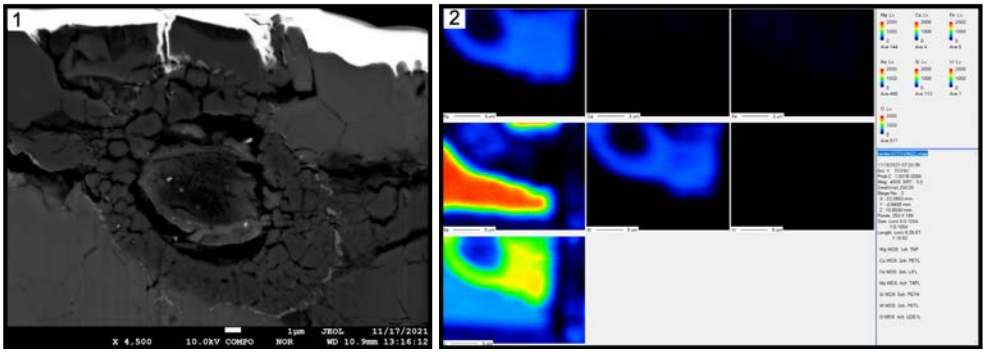


Figure 2.12: (1) BSE image showing the heating center of the LH-DAC experiments (ON22) (2) Elemental maps obtained with the FEG-EPMA.

Samples were examined with an acceleration voltage of 10 kV and a beam current of 10 nA. X-ray maps of Si, Mg, Fe, Ca, Na, O, and W were collected. Unfortunately, due to focusing problems and/or sample holder instability, the data obtained were not quantitative and showed poor quality (Fig. 2.12) considering the theoretical capacities of such machines on LH-DAC samples. Two samples were lost during manipulation, and significant beam damage was observed after measurements.

### Transmission electron microscopy analyses (TEM)

The TEM provides a wide range of measurements to characterize nanometer-size solid-state samples with an atomic spatial resolution. Its working principle relies on a high voltage (∼200 to 300 kV) monochromatic electron beam produced and transmitted through an electron transparency specimen (∼100 nm thickness). The interaction between the incident beam and the specimen allows for nanoscale imaging, chemical composition, oxidation state, and crystal structure investigation (Fig. 2.13). A detailed introduction of TEM can be found in Williams and Carter (1996).

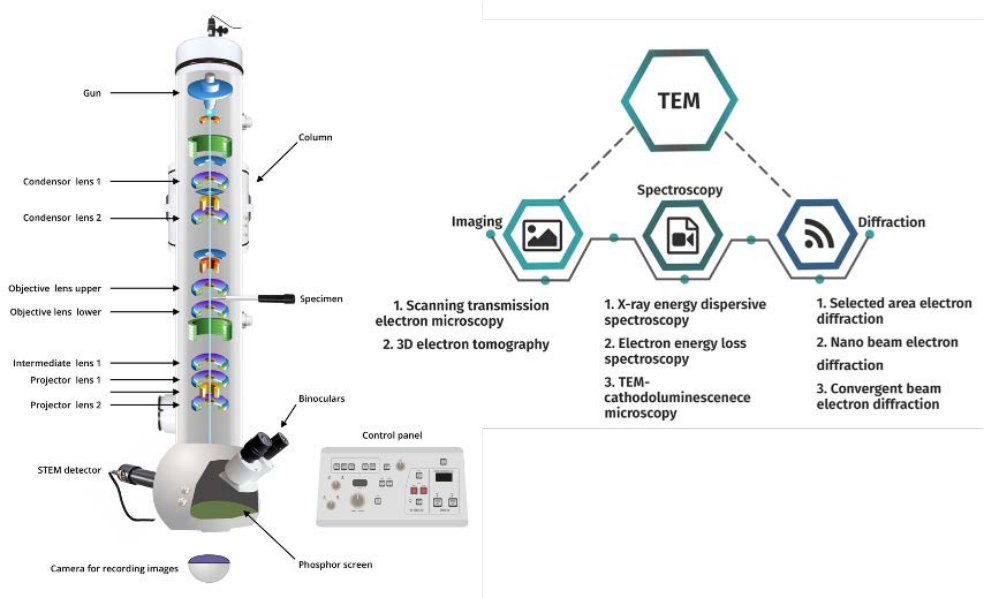


Figure 2.13: Schematic illustration of a transmission electron microscope (sourced on https://myscope.training/) and its working principle after Kumar et al. (2019).

In this work (Chapter 3), chemical and crystallographic characterization of the extracted FIB foils, after unsuccessful FEG-EPMA EDX mapping, was performed using a TEM Thermo Fisher Scientific Themis Z equipped with an aberration corrector at the probe side, a SuperX EDX 4 quadrant detector and a Gatan Imaging Filter (GIF) Continuum 1065 at 300 kV, installed at the PISA facility (GFZ, Postdam) by Dr. Vladimir Roddatis. High-resolution (HR-TEM) imagining with bright field (BF) and High-Angle Annular Dark-Field (HAADF) detectors, EDX maps, electron diffraction (ED), and electron energy loss spectroscopy (EELS) were performed.

Chemical information was obtained by HAADF imaging, a technique sensitive to the atomic number (Z), and by EDX analyses by scanning the sample with the beam (STEM) to obtain 2D elemental maps, as with SEM/EPMA. All EDX maps provided a qualitative chemical composition and were collected at 300 kV using a 50 pA electron beam and averaged multiple frame acquisition. EELS and ED measurements were used complementary to our EDX elemental mapping, to confirm the carbon phase as diamond. The spectrometer was calibrated using NiO and Cu samples to tune the peaks' position and dispersion.

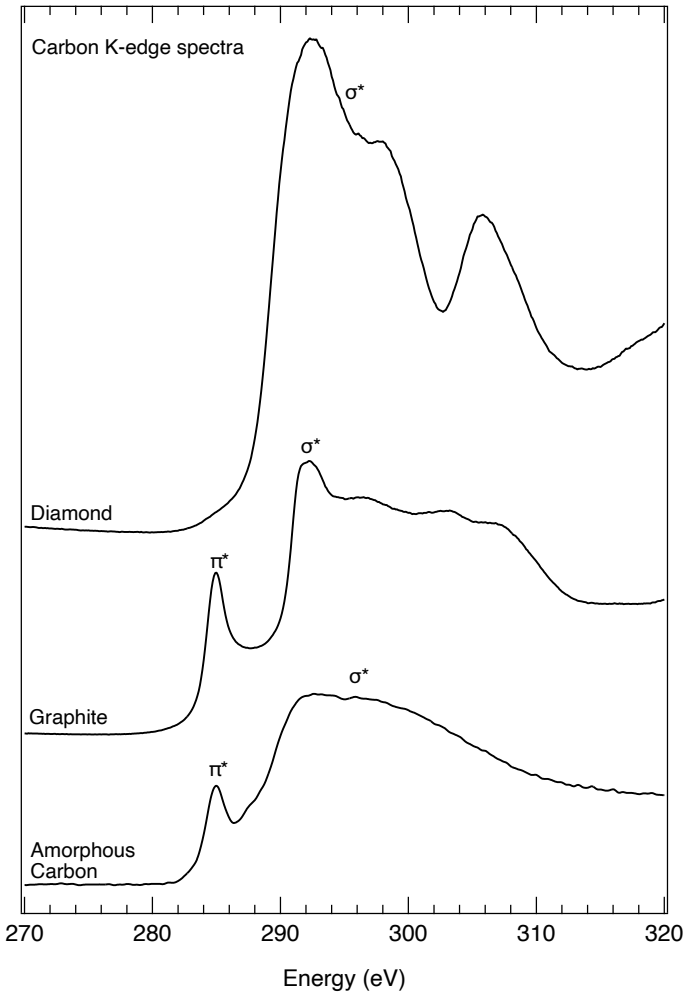


Figure 2.14: Example of Carbon K-edge spectra of different pure carbon phases obtain from the EELS DB database (https://eelsdb.eu/) Ewels et al. (2016). The diamond spectra from Serin et al. (1997) and amorphous carbon from Lajaunie et al. (2017).

The EELS method detects the loss in the kinetic energy of inelastically scattered electrons (Fig. 2.8). The spectrum region above 50 eV (core-loss spectrum) represents the inelastic scattering of inner shell electrons leading to the 'ionization edges' spectral feature. The fine structure of this edge provides structural and chemical information, sensitive to low-Z elements such as carbon. The EELS measurements were performed on areas containing a high carbon content in EDX maps in order to identify the carbon phase present in the sample. In Fig. 2.14 different carbon K-edges of different carbon-bearing phases are plotted. Diamond show more unique edge shapes than graphite and amorphous carbon. Indeed, the latter are both displaying a lower energy peak at ∼285 eV, which is not present for diamonds. The difference in the K-edge can be explained by the difference of orbital hybridization bond ($sp^3$, $sp^2$, sp); for example, the $sp^2$ bonding in graphite results in the 285 eV peak, identified as transition to the

$\pi^*$ anti-bonding molecular orbital, and a second peak at ∼290 eV as the transition to $\sigma^*$ orbital (Weng et al., 1989). Whereas, in diamond, the carbon atoms bonding is described as tetrahedrally directed $sp^3$ hybrid orbitals, with the first peak identified to result of the transition to the molecular orbital of $\sigma^*$ character (Weng et al., 1989).

The electron diffraction measurement relies on the part of the electron that is elastically scattered while being transmitted through the specimen producing a diffraction pattern that provides information on the crystal structure of the phase. The diffraction pattern obtained from an nm-sized area exhibits spots in a periodic arrangement. Each spot corresponds to a point in the reciprocal lattice of the crystal, and their location and intensity inform about the crystallographic structure of the phase analyzed. The central spot is the directly transmitted beam and the distance and angles between the others diffraction spots give direct information on the lattice spacing, and angles between lattice planes. Then ED helps to evaluate the potential space group of a phase for phase identification. However, in the case of HP phases, amorphization during FIB-milling will cause the loss of the structure of the high-pressure phases, e.g., bridgmanite (Marquardt and Marquardt, 2012).

# 3 | Reevaluating the stability of magnesite in the Earth's lower mantle

As introduced in section 1.2, carbonates entrapped in subducting slabs have significant potential to transport carbon from the Earth's surface to its deep interior, and magnesite is likely to be the major carbonate carried into the deep mantle. In this chapter, the stability of magnesite in co-existence with the most abundant lower mantle mineral, bridgmanite $(Mg, Fe)SiO_3$ is examined. In particular, we assess the processes of decarbonation, melting, and diamond formation at lower mantle conditions, in which Fe is likely to play a crucial role. We conducted high-pressure experiments with two experimental techniques: (1) large-volume experiments using multi-anvil apparatuses were conducted to better assess the presence of melt at the top of the lower mantle conditions (25 GPa and 1600 to 2000 K), and (2) LH-DAC experiments were conducted to assess the magnesite-silicate interaction over a wider range of pressures (from top to mid-lower mantle conditions; 33 to 75 GPa) and temperatures (covering all subduction geotherms; 1300 to 2000 K). Our system aims to serve as an analog for reactions that occur between the Fe-bearing mantle and carbonated subducted slabs.

## 3.1 Experimental and analytical details

### 3.1.1 Multi-anvil experiments

Multi-anvil experiments were performed at 25±1 GPa and 1600-2000 K for 1 to ∼3 hours using multi-anvil apparatus installed at the Bayerisches Geoinstitut (Germany) using 7/3 mm WC anvils (also see Chapter 2, section 2.2.1). Each experiment contained one capsule except for run #1, #2, #3 and #4 in which two capsules (#4$^a$ and #4$^b$) were placed in one assembly. One (failed) experiment was conducted at pressure 32-33 GPa using the IRIS-15 press, a 15-MN Kawai-type multi-anvil press (Ishii et al., 2016), also at the Bayerisches Geoinstitut from the group of Prof. Tomoo Katsura and with the help of Dr. Artem Chanyshev. This pressure point was not investigated further due to the very challenging sample preparation.

| Run n° | P (GPa) | Temp. (K) | Dur. (min) | Starting material | Comments |
|---|---|---|---|---|---|
| #1$^{a+b}$ | 32-33 | 2000 | 60 | MG11:Sr + MG11:La | Failed; capsule opened |
| #2$^{a+b}$ | 25 | 2000 | 5 | MG11:Sr + MG11:La | Failure during heating |
| #3$^{a+b}$ | 25 | 2100 | 50 | MG11:Sr + MG11:La | Failure during heating |
| #4$^{a+b}$ | 25 | 2000 | 60 | MG11:Sr + MG11:La | |
| #5 | 25 | 1800 | 135 | MG11:La | |
| #6 | 25 | 1900 | 135 | MG11:La | |
| #7 | 25 | 1800 | 135 | MG11:Sr | |
| #8 | 25 | 1723 | 180 | MG11:La | Failed |
| #9 | 25 | 1600 | 120 | MG11:La | |

Table 3.1: Experimental conditions details for all multi-anvil experiments made in this work. Pressure and temperature uncertainty in MAP is ±1 GPa and ±100 K, respectively (Rubie, 1999). $^{a+b}$ indicate that two capsules were placed inside a single experiment. Starting material details can be found in section 2.1.

After the experiments, the recovered samples were mounted in epoxy, polished, carbon-coated, and examined at the University of Potsdam for textural features and preliminary phase identification with SEM and for quantitative major element compositions with an EPMA JEOL JXA-8200 (section 2.3.2). A 15 keV and 15 nA beam and a ZAF matrix correction were used. The beam diameter varied depending on the phases being analyzed; 2 µm for silicate minerals, 5 µm for carbonate minerals, and 5 to 7 µm for average melt composition measured in the dendritic quenched-melt (QM) texture. The EPMA standards used for silicate phase measurements were either garnet and diopside or clinopyroxene and orthopyroxene for Al, Fe, Mg, Ca,

and Si, albite for Na, strontianite for Sr, and lanthanum-phosphate for La. For the carbonate phase and quenched-melt measurements, standards were dolomite for Ca and Mg, siderite for Fe, strontianite for Sr, lanthanum-phosphate for La, and albite for Na. $CO_2$ concentrations were not quantified but calculated from the deficit of the analytical totals.

### 3.1.2 LH-DAC experiments

LH-DAC experiments were performed from 33 to 75 GPa and 1300 to 2050 K using BX90 diamond anvil cells and diamond anvils of 300 or 200 µm culets depending on the target pressure. Compressed thick starting material platelets (15 to 20 µm) were loaded between two insulating layers of NaCl, in a rhenium gasket indented to 35 to 45 µm thick (section 2.2.2). Each cell was placed in an oven at ∼120-150 °C overnight prior to compression to minimize water absorption before closing. One experiment (ON34) was performed at 43 GPa and 1300 K without magnesite, containing only a compressed platelet of silicate glass in between insulating NaCl layers. This experiment served to investigate the run products issued from the glass crystallization itself. The experimental conditions and analytical techniques are reported in Table 3.2.

In situ phase identification was made using X-ray diffraction (XRD) at the Extreme Conditions Beamline (ECB) at the PETRA III (section 2.3.1). After releasing the pressure, Raman spectroscopy (section 2.3.1) measurements were performed to detect the presence of diamond, following the same methods described in Drewitt et al. (2019). Ramam 2D maps, covering the entire area of the sample chamber, were made using a grid of 2 x 2 $\mu m^2$ or 4 x 4 $\mu m^2$ steps, with 10 to 20 sec acquisition per spectrum. Spectra for diamond detection were acquired with a 532 nm laser and a 1800 gr/mm grating in 1300 to 1400 $cm^{-1}$ spectral range. The processing of the Raman 2D maps was designed to search for the first-order diamond band at 1332 $cm^{-1}$. For each point on the maps, the diamond band integral was calculated using the spectral range between 1320 to 1340 $cm^{-1}$, and a baseline correction was applied by subtracting the background intensity obtained from 1360 to 1380 $cm^{-1}$ spectral range. Afterward, several samples were prepared for transmission electron microscopy (TEM) using a FIB (section 2.3.2 and 2.3.2).

| Run n° | P (GPa) | Temp. (K) | Dur. (min) | Analytical methods |
|---|---|---|---|---|
| | | **MG11** | | |
| ON01 | 41 | 1750 | 23 | Raman + in-situ XRD + STEM |
| ON02 | 41 | 1450 | 36 | Raman + in-situ XRD + EDX FIB |
| ON03 | 41 | 1600 | 26 | Raman + in-situ XRD |
| ON08 | 44 | 1900 | 35 | Raman + in-situ XRD |
| ON19 | 51 | 1700 | 21 | Raman + in-situ XRD |
| ON20 | 51 | 1400 | 14 | Raman + in-situ XRD |
| ON25 | 62 | 1650 | 13 | Raman + in-situ XRD + STEM |
| ON26 | 62 | 1700 | 18 | Raman + in-situ XRD |
| ON27 | 62 | 1350 | 5 | Raman + in-situ XRD + STEM |
| ON28 | 56 | 1400 | 13 | Raman + in-situ XRD |
| ON29 | 56 | 1900 | 10 | Raman + in-situ XRD + STEM |
| ON31 | 66 | 1400 | 14 | Raman + in-situ XRD + EDX FIB |
| ON32 | 66 | 1650 | 17 | Raman + in-situ XRD + EDX FIB |
| ON33 | 66 | 1500 | 16 | Raman + in-situ XRD |
| | | **MG13** | | |
| ON21 | 33 | 1650 | 14 | Raman + in-situ XRD + EDX FIB |
| ON22 | 33 | 1350 | 11 | Raman + in-situ XRD + STEM |
| | | **M011** | | |
| ON06 | 68 | 1850 | 33 | Raman + in-situ XRD |
| ON07 | 68 | 2000 | 29 | Raman + in-situ XRD |
| ON11 | 40 | 2050 | 36 | Raman + in-situ XRD |
| ON13 | 40 | 2000 | 55 | Raman + in-situ XRD |
| | | **$(Mg, Fe)SiO_3$ glass** | | |
| ON34 | 43 | 1300 | 14 | Raman + in-situ XRD + EDX FIB |

Table 3.2: Experimental conditions details for LH-DAC experiments presented in this work sorted by starting materials: **MG11**: ($MgCO_3$ + $(Mg, Fe)SiO_3$ glass (1:1); **MG13**: ($MgCO_3$ + $(Mg, Fe)SiO_3$ glass (3:1) and **MO11**: ($MgCO_3$ + olivine (1:1). Starting material details can be found in section 2.1 and analytical details can be found in section 2.3. Pressures were determined by Raman shift of the single peak of the diamond anvil at the diamond culet surface with uncertainties estimated to be ±2 GPa below 250 GPa Akahama and Kawamura (2006). Reported pressures are those measured from the diamond anvil post-heating, which typically differed by <4 % to the pre-heating pressure. The temperature reported is the temporal average of recorded temperature over the heating duration and rounded to the nearest 50 K. Uncertainties are estimated to be 10 % of the temperature value Konôpková et al. (2021).

## 3.2 Results

### 3.2.1 Multi-anvil experiments

All of the 5 successful multi-anvil experiments were above the solidus and revealed the occurrence of quench melt. The quenched-melt is easily identified in experiments #4, #5, #6, and #7 by its dendritic texture (Fig.3.1 and Fig. B.1 in appendix for #5). In these experiments, chemical measurements revealed that the La or Sr dopants were only detectable in the quenched melt (Table B.1 in appendix B.1). This diagnostic feature was used to confirm the ambiguous texture observed in experiment #9 as quenched-melt (Fig.3.1). None of the experiments showed sub-solidus assemblages indicating that the solidus line must be lower than the lowest temperature achieved in this study (#9, 1600 K at 25 GPa).

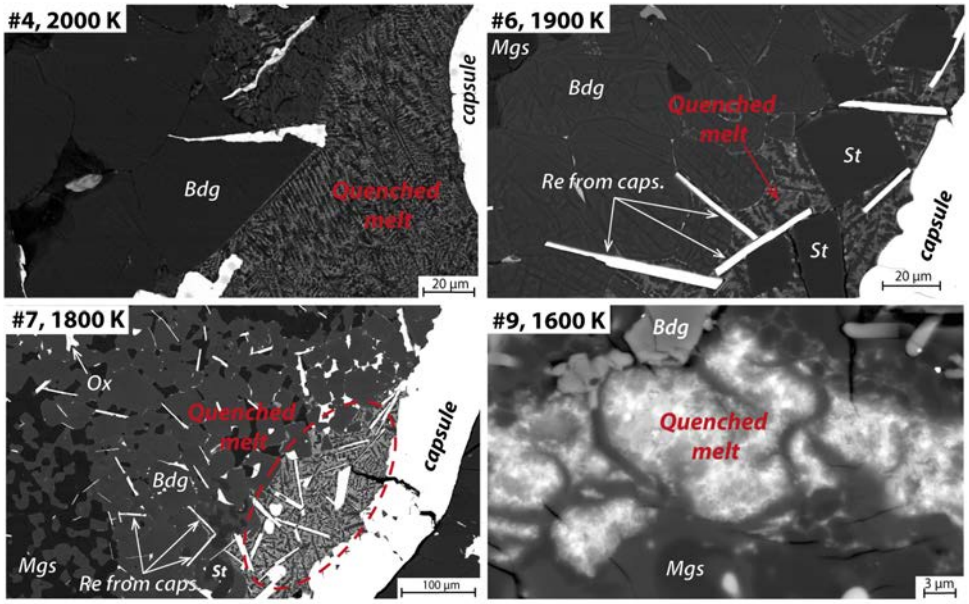


Figure 3.1: Back-scatter electron (BSE) images of experimental products from multi-anvil quench experiments. Bdg: bridgmanite, Mgs: magnesite, St: stishovite, capsules are made of rhenium. Additional images of run #1, #2, #3, #8 and #5 can be found in the appendix B.1 (Fig. B.1 and B.2)

Silicate mineral grains were found to be larger in the proximity of the melt pockets than elsewhere in the capsule (Fig.3.1, run #6). This is particularly evident in the case of stishovite grains, indicating that stishovite growth is enhanced by melt. No bubbles were observed, suggesting that no $CO_2$-fluid was produced. Rhenium shards are observed in all capsules.

Representative major element compositions obtained by EPMA are presented in Fig. B.3, in Table B.1, and details measurements in appendix B.1. The results of the chemical analysis revealed that the run product contained an assemblage of ferromagnesite [$(Mg_{0.88-0.95}, Fe_{0.04-0.06})CO_3$], bridgmanite [$(Mg_{0.86-0.92}, Fe_{0.10-0.13})SiO_3$], stishovite ($SiO_2$) and quenched-melt (Fig.3.1, Table B.1 in appendix B.1). In two experiments (#6 and #7), $ReO_2$ and (Fe,Re,Mg)-oxide were found in the vicinity of the melt pockets, likely from an interaction between the rhenium capsules and the carbonate-rich melt produced.

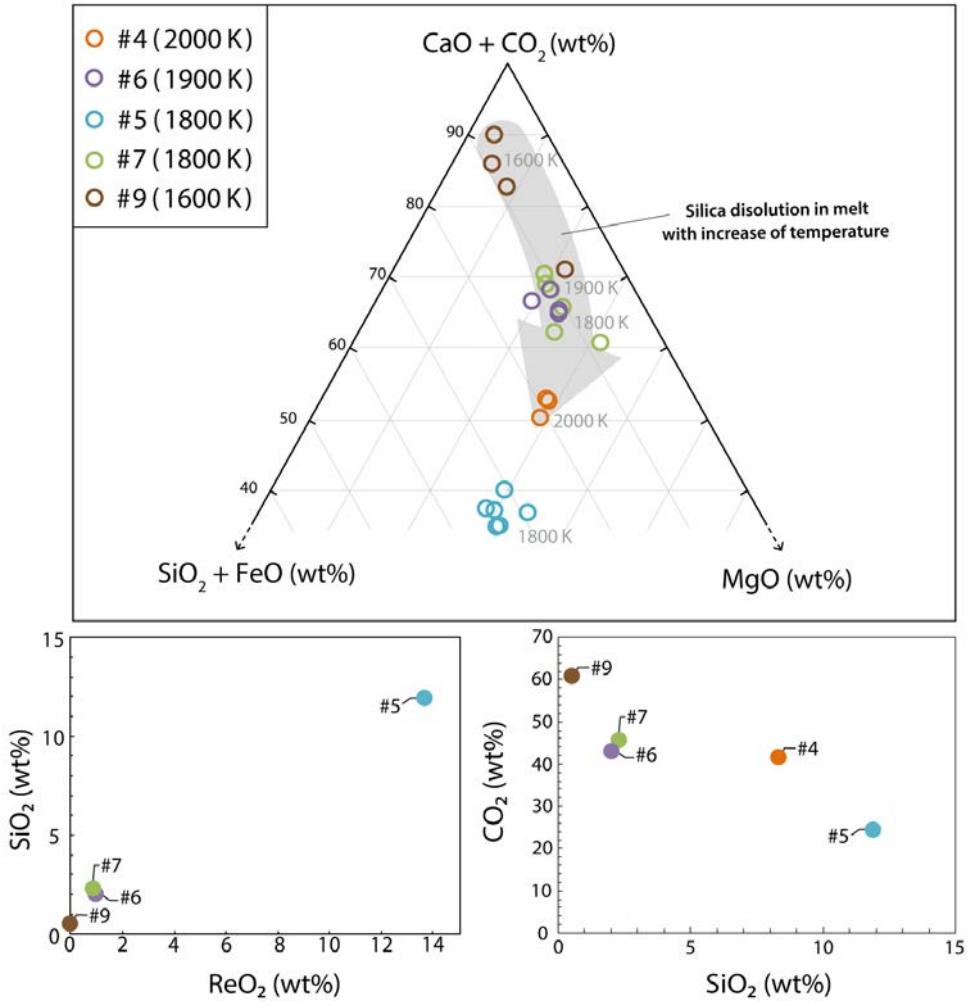


Figure 3.2: Composition of quenched-melt from EPMA analyses.

The composition of the quenched-melt evolves with increasing temperature (Fig.3.2) from essentially silica-free and carbonate-rich ($SiO_2$ = 0.55 wt% and $CO_2$ = 60.58 wt%) at 1600 K the lowest temperature investigated in run #9, with a concentration of $CaCO_3$ = 13.25 wt%, MgO = 8.85 wt%, and FeO = 6.63 wt%. To become

enriched of silica at 2000 K in run #4 containing 8.36 wt.% of $SiO_2$, $CaCO_3$ = 6.39 wt%, MgO = 26.26 wt% ; FeO = 9.53 wt%, and $CO_2$ = 41.36 wt% (Fig.3.2, Table B.1 in appendix B.1). Run #5 is an exception to this trend and shows an even higher enrichment of $SiO_2$, as well as in $ReO_2$ reaching 13.7 wt.% (Fig. 3.2). These values are inconsistent with the other experimental results.

### 3.2.2 LH-DAC experiments

#### Evidence of phase crystallization

Results obtained from the diffraction patterns of our LH-DAC experiments exhibited peaks corresponding to bridgmanite, stishovite, NaCl (pressure medium), and in some cases magnesite. Bridgmanite was observed in all runs including the reference experiment that did not contain magnesite in the starting material (ON34, Fig. S3.4). Consequently, bridgmanite formed from our silicate starting material. Stishovite is produced by exsolution as a result of low Fe solubility in bridgmanite that cannot accommodate all Fe available. Instead, it breaks down into a mixture of bridgmanite + stishovite + ferropericlase [$(Mg, Fe)O$] (Dorfman et al., 2021, 2012; Tange et al., 2009). No diffraction peaks of ferropericlase could be identified, even in ON34. As well as no decarbonation products, i.e, diamond or $CO_2$ were identified, mainly due to peaks overlapping in multi-phase systems, which complicates the analyses of run products by in situ XRD analyses. Furthermore, the X-ray focus size, the small volume of material being probed, and the relatively low scattering power of carbon and oxygen create an extremely challenging environment to detect carbon-bearing phases, as also stated in previous studies (Drewitt et al., 2019; Mao and Boulard, 2013).

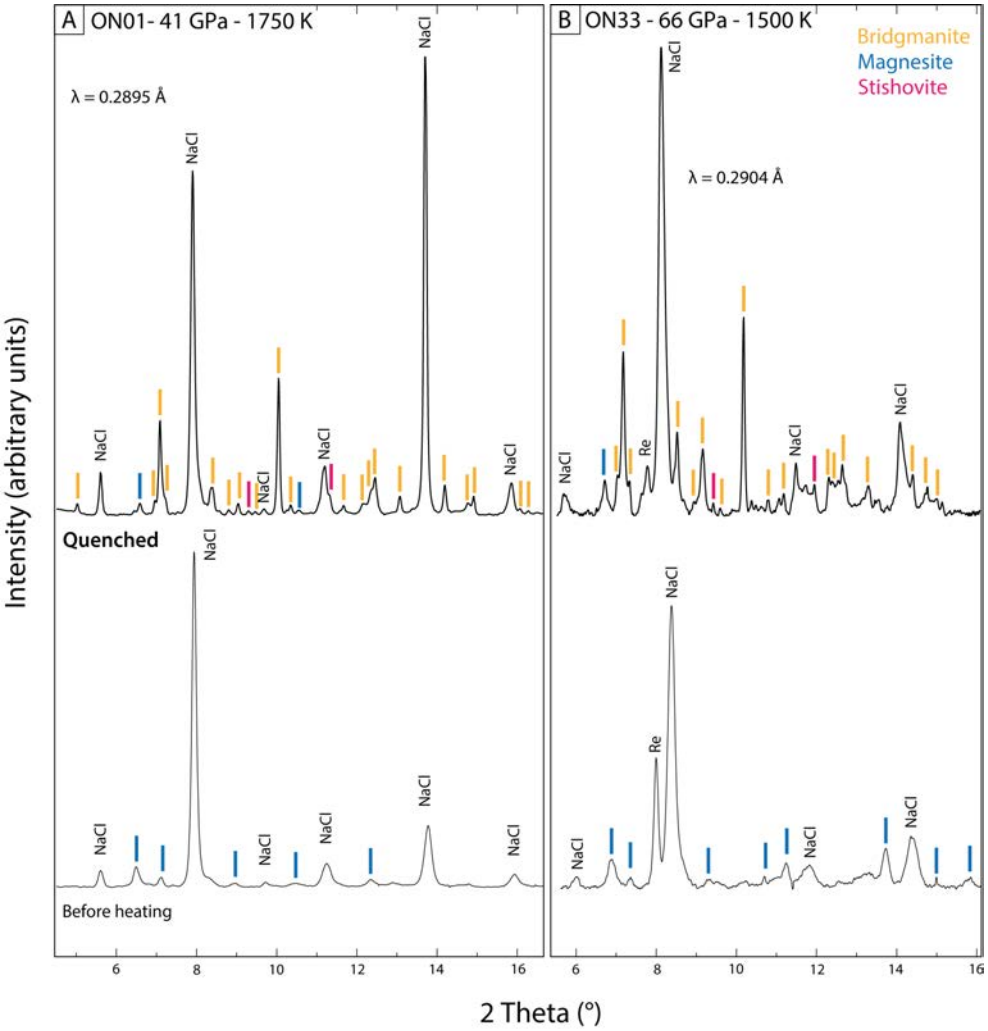


Figure 3.3: Selected X-ray diffraction patterns after background subtraction obtained before heating and after temperature quench. (a) run ON01 and (b) run ON33. Phases are indicated by colored ticks at the peak position, yellow = bridgmanite, blue = magnesite, and pink = stishovite. The wavelength of the X-ray beam is indicated by $\lambda$.

### Detection of diamonds

Decomposition of magnesite has been shown to be a viable mechanism to form diamonds and/or $CO_2$ (Drewitt et al., 2019; Maeda et al., 2017; Seto et al., 2008; Luth et al., 2022). However, these phases are challenging to be detected using in situ XRD analyses due to the X-ray focus size, the small volume of material being probed, and the relatively low scattering power of carbon and oxygen, as also stated in previous studies (Drewitt et al., 2019; Mao and Boulard, 2013). To facilitate the detection of diamonds in recovered experiment products from LH-DAC, Raman spectroscopy was

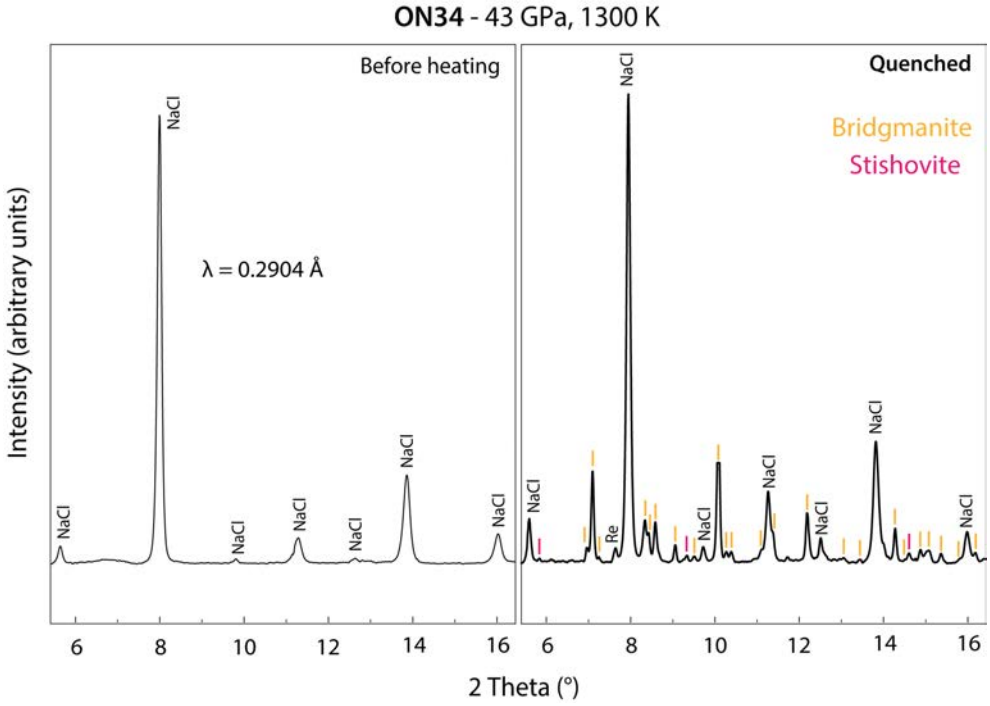


Figure 3.4: Selected X-ray diffraction patterns after background subtraction obtained before heating and after temperature quench. (a) run ON01 and (b) run ON33. Phases are indicated by colored ticks at the peak position, yellow = bridgmanite, blue = magnesite, and pink = stishovite. The wavelength of the X-ray beam is indicated by $\lambda$.

used, following the protocol described in (Drewitt et al., 2019). Maps covering the entire area of the sample chamber were made using a grid of 2 × 2 µm$^2$ or 4 × 4 µm$^2$ steps, with 10 to 20 sec acquisition per spectrum. Spectra for diamond detection were acquired with a 532 nm laser and a 1800 gr/mm grating in 1300 to 1400 cm$^{-1}$ spectral range. The processing of the Raman 2D maps was designed to search for the first-order diamond band at 1332 cm$^{-1}$. For each point on the maps, the diamond band integral was calculated using the spectral range between 1320 to 1340 cm$^{-1}$, and a baseline correction was applied by subtracting the background intensity obtained from 1360 to 1380 cm$^{-1}$ spectral range (Fig **??**A).

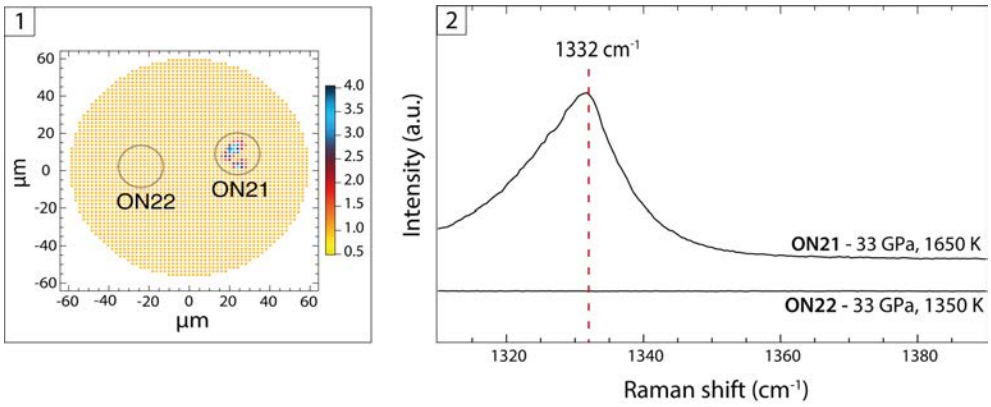


Figure 3.5: Example of Raman spectra illustrating the process of diamond detection, by investigating the presence of the fundamental diamond peak at 1332 $cm^{-1}$, with (2) the examples of two experimental points (ON21 and ON22) confirming either the presence (ON21) or the absence (ON22) of diamond within the sensitivity of the equipment.

Fig. 3.5 shows a representative example of a processed 2D map obtained by Raman spectroscopy revealing the presence of diamond in run ON21 (33 GPa and 1650 K). In contrast, no diamond peaks were detected in run ON22 (33 GPa and 1350 K) in the same Raman 2D map. Later, STEM analyses confirmed the presence of nanometer-sized diamonds in this run (ON22, Fig. 3.6), and similar observations were made in several runs (ON02, ON22, ON25, ON27, ON29, ON31, and ON32, Table 3.3). Consequently, the Raman spectroscopy routine proposed in Drewitt et al. (2019) has shown to not be sufficient to thoroughly identify the presence of nano-meter-sized diamonds in our LH-DAC experiments. Unsuccessful FIB preparation directly caused the absence of confirmation for diamond presence for samples in which Raman measurements did not detect diamonds (ON03, ON20, ON26, ON28, and ON33, Table 3.3).

### Results from TEM analyses

Textural and chemical features observed by STEM (Fig. 3.6) are similar in all investigated experiments. The location of the laser-heated reaction center can be easily identified as a round-shaped area, with an annular distribution of phases. Within the center, a mixture of nanometer-sized diamonds, and ferropericlase, or wüstite (FeO) in one run (ON29), was observed. Crystal structures of FeO and nano-diamonds were confirmed using ED and EELS (Fig. 3.6 and Fig. B.4 in appendix B.2 for FeO in ON29). An iron-depleted amorphous silicate phase, identified as being bridgmanite

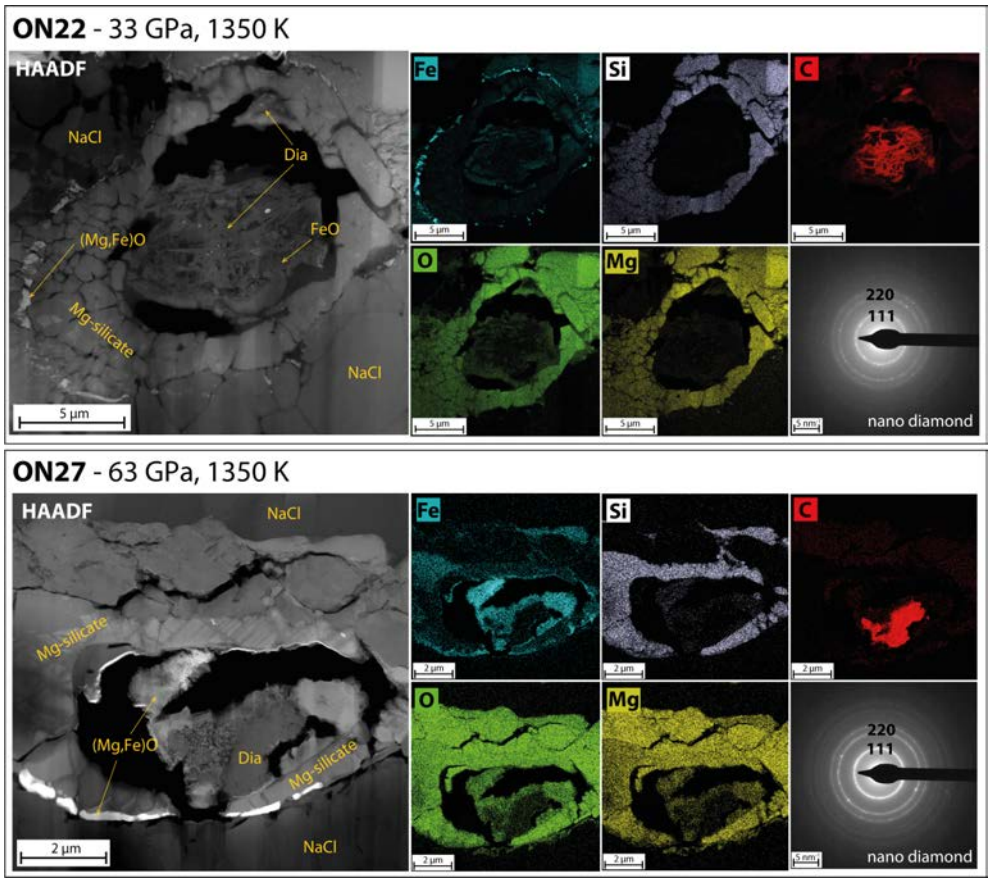


Figure 3.6: Results from ex situ analyses of recovered LH-DAC samples. HAADF-STEM images, EDX maps, and electron diffraction from nano-diamond of selected recovered samples (ON22 and ON27).

before quenching, surrounds the 'diamond-ferropericlase' center. The amorphization of the bridgmanite may have been caused by the $Ga^{+}$ beam during FIB milling (Marquardt and Marquardt, 2012). A ring of ferropericlase encloses and marks the border of the heated area. The surrounding volume consists of NaCl, and unheated starting materials, which explains the presence of magnesite peaks in the diffraction patterns after heating (Fig. 3.3). Furthermore, most of the STEM foils show void areas that are associated with cracks formed during decompression and manipulation during FIB milling. Most damages were caused by the beam used during EDX mapping at the FIB-SEM and by failed attempts of field emission gun electron microprobe (FEG-EMP) mapping, performed before STEM analyses (section 2.3.2).

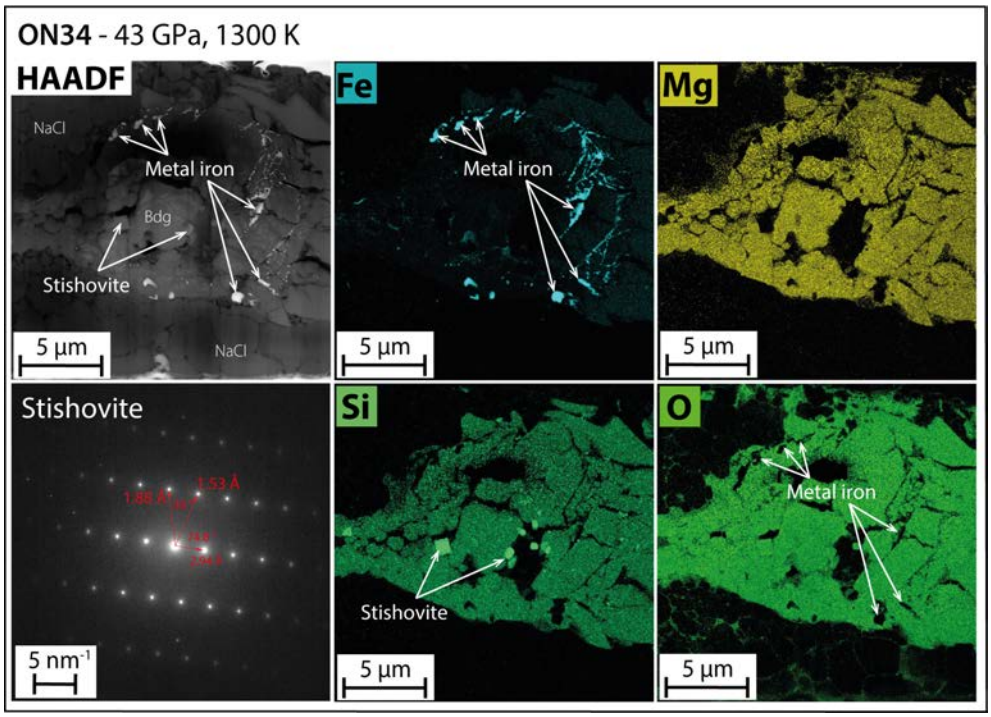


Figure 3.7: Ex situ analyses obtained by STEM of run ON34 containing only silicate glass showing the dark-field image (HAADF), chemical maps for iron, magnesium, silicon, and oxygen, and electron diffraction on stishovite grains. Elemental maps are revealing the presence of stishovite and Fe-metal as indicated by the arrows.

In the reference experiment (ON34), the STEM investigation revealed that heating of the starting glass results in the crystallization of a phase mixture of bridgmanite, stishovite, and metallic iron ($Fe^0$). Stishovite was identified from pure $SiO_2$ regions in EDX maps and confirmed by ED (Fig. 3.7). The iron metal grains were identified in elemental maps as oxygen-depleted versus iron-rich regions. Chemical analyses revealed high iron concentration and an oxygen K-edge peak too low to be an iron-oxide. Previous studies have reported the occurrence of metallic iron grains in lower mantle phase assemblages due to the Fe disproportionation reaction (Dorfman et al., 2021; Auzende et al., 2011; Frost et al., 2004). Additionally, the presence of iron metal suggests that the redox conditions are at $\Delta\log fO_2$ around 0 to -1.5 relative to the IW buffer (Rohrbach and Schmidt, 2011). Although observed in ON34, iron metal was not found in any run loaded with magnesite indicating that it reacted completely to form oxides (Fig. 3.6).

Four pressure-temperature points (ON06, 07, 11, and 13) were investigated with the MO11 starting material containing Pt as a laser coupler. None of the samples were recovered successfully for STEM investigation, and only Raman spectroscopy identified the presence of diamonds in the 4 experiments. Therefore, no additional data could be collected to evaluate the potential effects of (1) the change of starting composition in the reaction and (2) the potential effect of Pt on the Fe contained in the sample. Details of run products from the different analytical methods used for each LH-DAC experiment are provided in Table 3.3.

| Run n° | Phases in XRD | Diamond in Raman | Phases in TEM |
|---|---|---|---|
| | | **MG11** | |
| ON01 | Bdg + Mgs + Sti | yes | Dia + Bdg + Fp |
| ON02 | Bdg + Mgs + Sti | no | Dia + Bdg + Fp |
| ON03 | Bdg + Mgs + Sti | no | NA |
| ON08 | Bdg + Sti | yes | NA |
| ON19 | Bdg + Sti + Mgs | yes | NA |
| ON20 | Bdg + Sti + Mgs | NA | NA |
| ON25 | Bdg + Sti + Mgs | NA | Dia + Fp + Bdg + Mgs |
| ON26 | Bdg + Sti + Mgs | NA | NA |
| ON27 | Bdg + Sti + Mgs | no | Dia + Wus + Fp + Bdg + Mgs |
| ON28 | Bdg + Sti + Mgs | no | NA |
| ON29 | Bdg + Sti + Mgs | no | Dia + Wus + Fp + Bdg |
| ON31 | Bdg + Sti + Mgs | no | Dia |
| ON32 | Bdg + Sti + Mgs | NA | Dia |
| ON33 | Bdg + Sti + Mgs | NA | NA |
| | | **MG13** | |
| ON21 | Bdg + Sti | yes | Dia |
| ON22 | Bdg + St | no | Dia + Bdg + Fp |
| | | **M011** | |
| ON06 | Ol + Bdg + Sti | yes | - |
| ON07 | Ol + Bdg + Sti | yes | Dia + Bdg |
| ON11 | Ol + Bdg | yes | Dia + Bdg + Fp + Mgs |
| ON13 | Ol + Bdg | yes | - |
| | | **$(Mg, Fe)SiO_3$ glass** | |
| ON34 | Bdg + Sti | - | NA |

Table 3.3: Details of the run products for LH-DAC experiments. Phases: Mgs = magnesite, Bdg = bridgmanite, Fp = ferropericlase, Sti = stishovite, Dia = diamonds, Wus = Wüstite (FeO), Ol = Olivine (starting material). NA = data not available or not conclusive.

## 3.3 Discussion

### 3.3.1 The fate of deeply subducted magnesite

Results in this chapter provide new insights into the stability field of magnesite in presence of Fe-bearing lower mantle assemblages. Our experiments, plotted in Fig. 3.8 reveal the breakdown of magnesite by (1) the presence of a carbonate-rich melt in MAP experiments in a 'melting reaction' at 25 GPa and 1600–2000 K (downward triangle), and by (2) the presence of diamond in LH-DAC experiments via a 'decarbonation reaction' at 33–75 GPa and 1300–2000 K (diamond shape). These results are notably different from previous investigations utilizing simplified iron-free systems (Thomson et al., 2014; Kakizawa et al., 2015; Maeda et al., 2017; Litasov and Shatskiy, 2019), indicating that the presence of iron plays a major role in magnesite stability.

These results are notably different from the previously investigated temperatures on the iron-free $MgCO_3$-$MgSiO_3$ system from Thomson et al. (2014), which indicate eutectic melting at 25 GPa and ∼2000 K. In comparison, our results on the Fe-containing system reveal that melting occurs at temperatures 400 K lower (1600 K at 25 GPa), but do not provide sufficient insight on whether or not $MgCO_3$ induces melting if transported in the coldest subduction slabs ($\leq$1200 K at 25 GPa) (Fig. 3.8). Therefore, the presence of iron is lowering the melting temperature. A high-pressure extrapolation of our iron-bearing melting curve was made following the shape of the iron-free curve by Thomson et al. (2014) adjusted to lower temperatures (Fig. 3.8). Additionally, it has been investigated that in even more chemically complex systems, such as alkali-rich carbonated-MORB systems, the melting temperature is even lower and reaches as low as ∼1400 K if extrapolated up to 25 GPa (Thomson et al., 2016b; Kiseeva et al., 2013) (Fig. 3.8). This emphasized that the presence of alkali components has a greater effect on carbonated peridotite and eclogite solidi (Litasov and Shatskiy, 2018). Accordingly, our data combined with published data sets, support that the melting of carbonate-bearing phases contained in subducted slab may be an important mechanism for the elimination and the recycling of subducted carbonates and the generation of deep melt along all subduction geotherms with the exception of the very cold ones (Drewitt et al., 2019; Maeda et al., 2017).

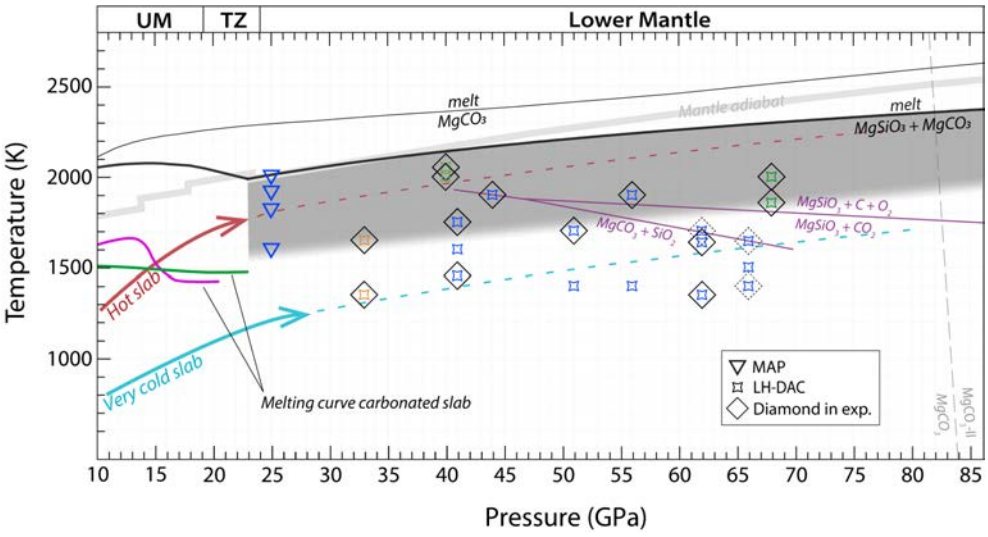


Figure 3.8: Pressure-temperature diagram of carbonates stability within subducted oceanic crust through Earth's mantle. Black line is the melting curve of $MgCO_3$ constrained by Solopova et al. (2015) and the black bold line below is the melting curve of the $MgCO_3$ + $MgSiO_3$ according to Thomson et al. (2014). Purple lines indicate decarbonation reaction of $MgCO_3$ + $SiO_2$ from Drewitt et al. (2019). Bold gray: mantle adiabat after Katsura et al. (2010). Typical slabs geotherms, red: hot slab and sky blue: very cold slab, modified from Maeda et al. (2017). The colors of the symbols refer to the starting composition: blue = MG11; orange = MG13 and green = MO11. Symbols correspond to the experimental technique used, triangle for multi-anvil and stars for LH-DAC experiments. The gray area indicates the area where melting is expected in our system. Symbols encased in a diamond shape indicate the presence of diamonds that was confirmed by Raman spectroscopy and/or TEM, the dashed diamond shape was only confirmed by EDX during FIB milling. The absence of the diamond shape indicates experiments in which diamonds were not detected during Raman measurements and not investigated by STEM due to preparation failure during FIB milling. The dashed gray line corresponds to the high-pressure transition of $MgCO_3$ to $MgCO_3$-II according to Binck et al. (2020). UM: Upper mantle and TZ: Transition Zone.

The existence of carbonate-rich melts at the transition zone to lower mantle depths is strongly linked to the P-T-$fO_2$. Experimental investigations have shown that if carbonate-rich melts infiltrate the metal-saturated ambient mantle, then carbonate-rich melts become unstable and reduced to diamond via a redox freezing process (Rohrbach and Schmidt, 2011) (see Eq. 1.4 in section 1.2.2). Therefore, the presence of carbonate-rich melts at depths exceeding 250 km remains uncertain. This hypothesis is supported by the finding of inclusions of native iron (Zedgenizov et al., 2014), Fe-carbides (Kaminsky and Wirth, 2011) and former C- and S-bearing iron melt (Smith et al., 2016) in diamonds. The redox conditions in our experiments were not purposefully controlled but the presence of Re and $ReO_2$ from the capsule and probably due to the interaction between the quenched-melt and the capsule suggests that it may have influenced the oxygen fugacity in our experiments at around +4 to

+5 log units relative to iron-wüstite (IW) (Rohrbach and Schmidt, 2011), but no evidence was made proving that the redox equilibrium was reached throughout the run product, therefore local variations have to be expected in our experiments. Nevertheless, if the redox conditions were oxidized it maintained carbon in its oxidized form, thus may have prevented diamond nucleation. Regardless, carbonate-rich melts are important agents of transport in the Earth's interior. They are able to transport significant amounts of incompatible trace and minor elements that can have economical importance such as the REEs, volatile elements ($H_2O$, halogens, and sulfur) as wells as major components such as C, as well as Mg, Ca, Fe, Na and K.

In LH-DAC experiments, the formation of diamond was observed at temperatures as low as, and even lower than, the coldest subduction geotherm at 33 GPa (1350 K) and at 62 GPa (1350 K), respectively (Fig. 3.8). The pressure and temperature conditions in which diamonds are observed differ noticeably from the ones reported in Drewitt et al. (2019) in the FMSC system (section 1.2.4) (purple lines in Fig. 3.8), and from previous studies (Seto et al., 2008; Maeda et al., 2017) using the iron-free system. These differences could be the result of the slight differences between starting bulk compositions, but it is most probably due to the unreliability of detecting diamonds when only using Raman spectroscopy as in Drewitt et al. (2019). Indeed, the investigations of the run products in their study relied only on the combination of in situ XRD analyses and Raman mapping, and no further, ex situ analyses were performed. Our analyses showed ex situ analyses, such as the TEM, are necessary to thoroughly prove the presence of diamond. The breakdown of magnesite into diamond in LH-DAC implies the presence of a reducing agent. Previous studies have shown that iron metal is a relevant reducing agent for magnesite (Dorfman et al., 2018; Martirosyan et al., 2019; Zhu et al., 2019), but these studies do not account for the presence of silicates. The results of the reference experiments (ON34, magnesite-free) show that the Fe metallic phase is produced during the crystallization of our starting silicate glass. No Fe-metal nor Fe-carbides were observed to co-exist with diamond, indicating that the Fe-metal may have formed as an intermediate phase and, then was completely consumed by reacting with $MgCO_3$ to form diamond via redox freezing (see Eq. 1.4). Whereas, the remaining $Fe^{2+}$ partitioned into ferropericlase and/or wüstite and the $Fe^{3+}$ into bridgmanite.

The temperatures of diamond formation reported here are lower than the melting temperatures reported from our MAP experiments, whereas no evidence of melting was observed in our LH-DAC experiments. Nonetheless, we expect that the shape of our iron-bearing melting curve will parallel the iron-free curve by Thomson et al. (2014), but adjusted to considerably lower temperatures. The newly derived iron-bearing melting area (gray area in Fig. 3.8) indicates that melting may occur at similar temperatures (but higher pressures) at which diamond crystallization is observed. This superimposition highlights a possible dynamic relationship between diamond crystallization and melting. Indeed, super-deep diamonds originating from depths from ≥250 km to the transition zone testify to have crystallized from melts produced by low-degrees partial melting of subducted carbonate-rich oceanic crust, as indicated by the elevated trace elements content within super-deep diamond mineral inclusions (Thomson et al., 2016a; Walter et al., 2008; Bulanova et al., 2010). In addition, oxygen ($^{18}$O) isotopic compositions from mineral inclusions in super-deep diamonds, coupled with carbon ($^{13}$C) and nitrogen ($^{15}$N) isotopic compositions from the diamond hosts, reveal that the carbon source for diamond formation is depth-dependent. Whereas sublithospheric diamonds that crystallize at depths ≤700 km (up to the shallow lower mantle) indicate a source from recycled oceanic crust, diamonds formed at depths ≥700 km lack evidence of such a source, supporting the barrier for carbon subduction at the top of the lower mantle (Regier et al., 2020).

Whether diamond formation necessarily involves redox freezing a carbonate-rich melt, or also happens as a sub-solidus reaction remains unclear from our study, further experiments are needed to localize the solidus in the investigated system. However, our data clearly demonstrate that magnesite is not stable at depths reflecting the shallow lower mantle (25 to 60 GPa). Our results show that when in contact with iron-containing silicates, magnesite is unlikely to be preserved throughout the lower mantle, even if transported in the coldest slab. Accordingly, the recycling of magnesite within the shallow lower mantle (≤40 GPa) inhibits the transport of carbonates to Earth's deeper interior.

### 3.3.2 Implications for the genesis of super-deep diamonds

One persisting uncertainty is whether or not subducted carbonates will survive within slabs to depths of at least 660 km without being reduced to diamonds at shallower depths since Fe metal is already stable at 250 km (Frost et al., 2004). The recent study of Martirosyan et al. (2022) assessed the complexities of carbonate + silicates + Fe redox interactions and evaluated their reaction kinetics at upper-mantle and hot subduction geotherm conditions (6 GPa - ∼1400 K). Their results indicate that the presence of silicates in an anhydrous and melt-free environment will slow down the redox reaction, due to the barrier that silicates constitute on Fe and O diffusion. Another recent study looked at the reaction kinetics of iron metal with different carbonates ($Na_2CO_3$, $K_2CO_3$, $CaCO_3$, $MgCO_3$, $(Ca, Mg)CO_3$, $FeCO_3$) and estimated that 45 to 70% of carbonates in subducted slabs will be preserved down to the transition zone if no melt occurs (Shatskiy et al., 2023). In such scenarios, carbonates may persist and reach the lower mantle and provide the carbon source for super-deep diamonds. Seismic imaging indicates that slabs can stagnate at the shallow lower mantle due to an increase of mantle viscosity (Fukao and Obayashi, 2013; Marquardt and Miyagi, 2015). This stagnation may promote an environment where carbonated slabs accumulate, increasing the amount of oxidized reactant over time to reduce and form super-deep diamonds, even in the coldest subduction as shown by our data. As a result, a diamond production region (Zhu et al., 2019) is expected at the transition zone/lower mantle boundary. The rate of subduction will have a great influence on the supply of oxidized carbon necessary to produce diamonds over geological time since the concentration of carbonates present in slabs is limited to ∼0.3 wt.% (Dasgupta and Hirschmann, 2010).

The influx of oxidized carbon in the form of solid carbonates or carbonate melt in this mantle region is expected to increase the fugacity locally (Stagno, 2019; Stagno et al., 2011). As more carbonates interact with the lower mantle, consuming the Fe metal nearby, that leads to an increase in the local $fO_2$. Such localized $fO_2$ disparities are revealed from carbonate inclusions in sublithospheric diamonds (Brenker et al., 2007; Kaminsky, 2012; Bulanova et al., 2010), reflecting a higher oxidation state within the diamond production region, from IW to around IW +2 to +3 (at ∼25 GPa) where magnesite and diamond can co-exist (Stagno et al., 2011; Dominijanni, 2022). Hence, a metal-free mantle region may exist if the supply of oxidized phases surpasses the metallic iron redox capacity locally.

The re-mobilization of such diamonds by mantle upwelling to lower depths ≤250 km (lower $fO_2$) will form carbonate-melt via the redox melting, the inverse process of redox freezing (Eq. 1.4) (Rohrbach and Schmidt, 2011). Those carbonate melts, because of the low viscosity, are able to migrate rapidly upwards and then transport carbon back to the surface in a rising mantle plume, such as within ocean-island basalts (OIB) or carbonatites (Hammouda and Keshav, 2015; McCammon et al., 2020; Dasgupta and Hirschmann, 2010).

## 3.4 Conclusion

We combined a multi- experimental and analytical study using multi-anvil apparatus and laser-heated diamond anvil cells to investigate the reaction between magnesite and iron-bearing lower mantle assemblages. This reaction is used as an experimental proxy to investigate the interactions of carbonate minerals contained within the oceanic crust subducting into the lower mantle. Our data demonstrate that magnesite is not stable in the Fe-bearing system at cold slab temperatures (1350 K) and shallow lower mantle conditions (33 GPa). Magnesite is thus unlikely to be the phase carrying oxidized carbon deeper into the reduced lower mantle to depths greater than 700 km. Carbon will instead be present in its immobile and reduced form, diamond, and stored over long timescales in the deep mantle where it could be re-mobilized by mantle upwelling. Furthermore, we can speculate that the reduction of carbonate minerals contained in stagnating slabs will consume the metallic iron and produce a locally oxidized mantle, creating regions where oxidized and reduced carbon phases may co-exist.

# 4 Developments in synchrotron laser heating systems

This chapter presents the work carried out in the building and the commissioning of a portable laser heating system based at the University of Potsdam. Within the time of this thesis, I participated in its development, operation, and in its application during X-ray spectroscopy measurements at synchrotron facilities (Mergner et al., 2021; Albers et al., 2022, 2023; Müller et al., 2022; Kupenko et al., 2022). Throughout this time, I participated in the discussion about the accuracy of radiospectrometry measurements and was closely involved in the development of the 90° off-axis parabolic mirror as an imaging objective for laser-heating system (Spiekermann et al., 2021)

## 4.1 Introduction

The laser-heated (LH) diamond anvil cell (DAC) technique, since its introduction in the 1970s (Ming and Bassett, 1974), has become a routinely used tool for experimental investigation of material under the extreme conditions of the Earth's and planetary interiors (Boehler, 2000; Salamat et al., 2014). A short summary of the LH-DAC technique is given in section 2.2.2. One of the major advantages of the LH-DAC technique comes from the transparency or the low attenuation of the diamond anvils over a wide range of wavelengths, including X-rays. It permits not only in situ heating inside the DAC using lasers but also makes available a wide range of in situ spectroscopy techniques at university laboratories and at third-generation synchrotron radiation light sources. This feature enables to probe in situ, at high-pressure and high-temperature, the physical and chemical properties of solids and melts. A wide range of X-ray techniques can be applied in LH-DAC experiments, including Raman

scattering (Zhou et al., 2004; Lin et al., 2004; Goncharov and Crowhurst, 2005), Nuclear Magnetic Resonance (Meier et al., 2019) or Brillouin scattering (Li et al., 2006; Kurnosov et al., 2019). At synchrotron radiation facilities this includes X-ray diffraction (section 2.3.1) (Watanuki et al., 2001; Prakapenka et al., 2008; Petitgirard et al., 2013; Liermann et al., 2015), X-ray absorption (Kantor et al., 2018; Boccato et al., 2017), Inelastic X-ray spectroscopy (Sakamaki et al., 2016; Mergner et al., 2021), X-ray fluorescence (Petitgirard et al., 2012), Mössbauer spectroscopy (Kupenko et al., 2012) and X-ray emission spectroscopy (XES) (Spiekermann et al., 2019), both using permanent or using portable LH systems. This versatility of the LH-DAC technique has made it extensively used in various scientific fields, from solid-state physics to engineering, chemistry, and geosciences.

Nowadays, several LH systems are available at synchrotron facilities worldwide as permanent installations (Watanuki et al., 2001; Prakapenka et al., 2008; Petitgirard et al., 2013; Liermann et al., 2015; Meng et al., 2015; Kantor et al., 2018; Anzellini et al., 2018; Stan et al., 2018; Konôpková et al., 2021) or using portable systems (Dubrovinsky et al., 2009; Shen et al., 2010; Kupenko et al., 2012; Smith et al., 2018; Fedotenko et al., 2019). Several requirements are necessary when adding an LH system in the X-ray path of synchrotron beamline setups. A high flux beam with an extremely low divergence focused to a diameter of a few micrometers is necessary to probe the small sample inside the heated spot in the DAC. A micrometer precise alignment of the X-ray beam with the heating spot is also important to probe the reaction at the measured temperatures. Lastly, during laser heating, the heat produced is transferred to the DAC, then to its holder, leading to thermal expansion of the DAC and further misalignment. Water-cooled DAC holders help to limit this effect, but regular checking and re-alignment might be necessary over the time of heating.

LH systems were first introduced at X-ray diffraction beamlines (Shen et al., 2001) and evolved to be now routinely used with XRD in all fields of high-pressure sciences. There is now an increasing interest to apply LH-DAC with spectroscopy measurements available at synchrotron facilities. Recently the coupling of LH-DAC and X-ray absorption (XAS) has been achieved by Kantor et al. (2018). Meanwhile, interest has increased to apply it to X-ray emission spectroscopy (XES) and nuclear inelastic scattering (NIS), as they allow for a unique insight into the matter at extreme pressure (Lin et al., 2007; Murphy et al., 2013; Prescher and Prakapenka, 2015; Liu et al., 2018; Weis et al., 2019; Spiekermann et al., 2019). However, due to the uniqueness of each technique, specific challenges need to be taken into account when building a

laser heating system.

Here, I describe a portable and versatile near-infrared (NIR) LH system that is optimized for those X-ray spectroscopy measurements, such as XES and NIS, that benefit from a 90° scattering angle measurement geometry. Despite this optimization and portability, the system shares the basic characteristics of stationary double-sided on-axis LH systems as the ones installed at XRD beamlines. Later, a new development was introduced to the system, using a parabolic mirror as a reflective imaging objective, that demonstrates the possibility of more accurate radiospectrometric temperature measurements with on-axis laser heating at synchrotron facilities.

## 4.2 A portable laser heating system for synchrotron X-ray spectroscopy

The portable NIR fiber LH system was by design optimized for X-ray applications at PETRA III (P01) (Wille et al., 2010) such as X-ray emission spectroscopy (XES) and nuclear inelastic scattering (NIS) spectroscopy (Spiekermann et al., 2020).

### 4.2.1 Requirements for X-ray emission spectroscopy

XES and NIS are powerful tools in the determination of material properties at high-pressure. The first allows to probe the local structure and electronic spin configuration (Lin et al., 2005, 2007; Spiekermann et al., 2019). The second yields the phonon density of states of Mössbauer-active isotopes such as $^{57}$Fe and provides, among other parameters, the mean sound velocity (e.g., Debye velocity, $V_D$ - Chumakov et al. (2009)), which together with density and bulk modulus are the necessary parameters for calculating the compressional and shear wave sound velocities of materials at extreme pressures (Prescher and Prakapenka, 2015; Kupenko et al., 2015; Mergner et al., 2021). Both XES and NIS signals are preferably collected through the radial opening of diamond anvil cells near $90 \pm 25°$ with respect to the incident X-ray beam. However, the combination of XES or NIS with laser heating remains limited to a few beamlines due to the limitation of some of the requirements needed for the combination of both and was mostly carried out using portable LH system (Dubrovinsky et al., 2009; Murphy et al., 2013; Kupenko et al., 2015; Aprilis et al., 2017; Weis et al.,

2019; Fedotenko et al., 2019; Mergner et al., 2021) or using LH systems available at XRD beamlines (Lin et al., 2007; Rueff et al., 2008).

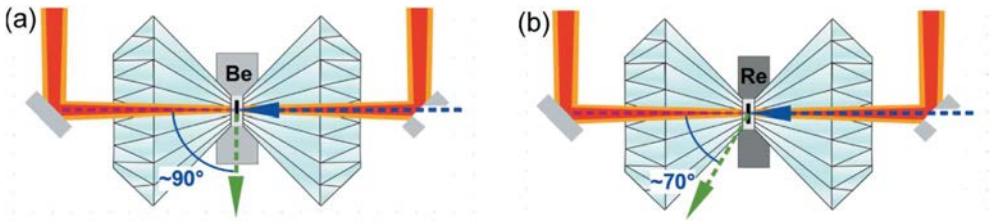


Figure 4.1: Sketches of the two near 90° signal collection for XES and NIS with on-axis heating and observation (red and orange paths, respectively), X-ray beam (dashed blue arrows), and scattered signal (green arrows). (a) through an X-ray transparent Be gasket as used here for NIS measurements. (b) collection at 70°, passing a rhenium gasket through the downstream diamond. The special gasket preparation needed for this setup can be found in (Albers et al., 2023).

The two near 90° measurement geometries of XES and NIS are demonstrated in Fig. 4.1, where the X-ray beam enters the DAC through one diamond (upstream, in the sense of the X-ray beam) and the emitted signal is collected either at 70° when rhenium gasket is used or at 90° with an X-ray transparent beryllium gasket. To allow data collection at ∼70° with a rhenium gasket and using a Von Hàmos spectrometer as in the case of XES measurements, a special gasket preparation needs to be performed to remove the wall/bulge of the gasket created during the indentation, before drilling the sample chamber (details can be found in Albers et al. (2023)). This preparation ensures an enlarged solid angle for the signal to get to the spectrometer with minimal attenuation of the signal. In the case of NIS measurements, the signal is collected at 90°, through a beryllium gasket. For this, two avalanche photo-diode detectors (APDs) are inserted through the radial opening of a panoramic DAC as close as possible to the sample (∼4 mm) (Appendix C, Fig. C.1), which allows coverage of a significantly larger solid angle (Kupenko et al., 2015). Both XES and NIS benefit from the measurements at near 90° since the emitted signal only passes through ∼500 $\mu$m of one diamond (and the beryllium gasket for NIS), which increases consequently the intensity of the detected signal.

### 4.2.2 Design of the laser heating system

The LH system is built on a 140 cm × 48 cm horizontal breadboard and weighs about 40 kg in total, excluding the laser and motor control unit. The laser beam of a single 100 W 1070 nm class 4 fiber laser (model YLR-AC100 from IPG Photonics) is split by a polarizing beamsplitter (BS) to achieve double-sided heating. For independent control of the intensity of each side, each beam passes through a motorized $\lambda/4$ phase-shifting plate (PP, or plate rotators) and a polarizing beamsplitter. The two laser beams, from each side (upstream and downstream relative to the X-ray beam, see Fig. 4.2), are coaxially coupled to the optical observation paths by dichroic mirrors (M) for on-axis alignment. The downstream side laser is directed by a 45° mirror to be focused by an objective (geoHEAT 60NIR or Mitutoyo M Plan Apo 20× or similar objectives) inside the DAC. The upstream side can be equipped with three different objectives: a geoHEAT 60NIR objective associated with 45° mirror, perforated with a pinhole of 300 $\mu$m diameter allowing the X-ray beam to pass trough without losses (Fig. 4.2b), or by Mitutoyo M Plan Apo 20× or similar objectives or by a parabolic mirror (Fig. 4.2c) (see below section 4.4).

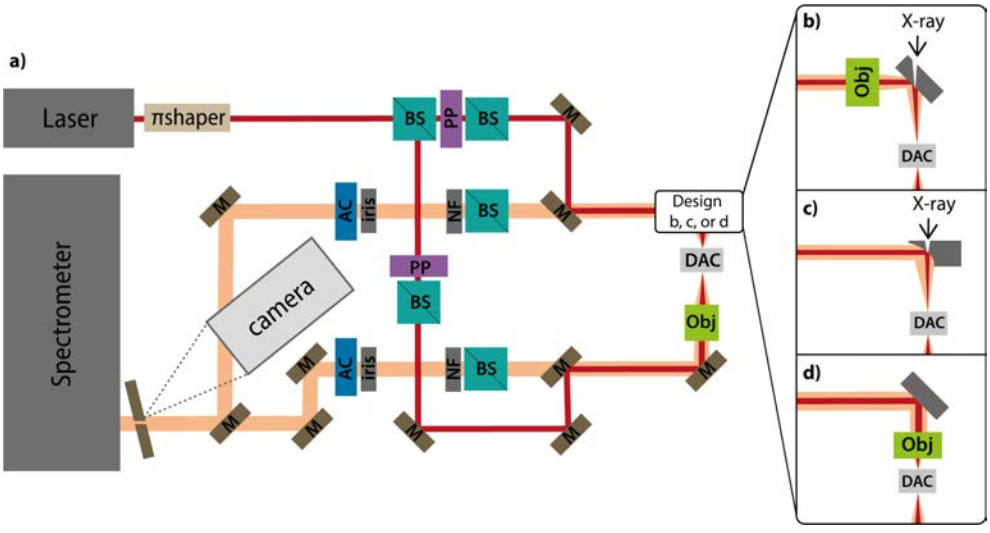


Figure 4.2: Schematic representation of the laser-heating system. Optical paths are shown in beige and the laser path in red. Different designs for upstream focusing are presented, at synchrotron facilities b) using a geoHEAT 60NIR objective and a perforated 45° mirror c) a parabolic mirror, or as a stationary system d) using Mitutoyo M Plan Apo 20× or similar objectives. Obj: objective, AC: achromat lens, M: mirror, BS: beamsplitter, PP: phase-shifting plate, NF: notch filter.

The design b (Fig. 4.2) adopts two geoHEAT 60NIR objectives and is mostly used in synchrotron laser heating. These objectives are optimized for laser light at 1070 nm and the observation wavelength range from 600 nm to 900 nm, with a focal distance of 60 mm. Meanwhile, a design closer to a laboratory LH system is provided in design d (Fig. 4.2), utilizing Mitutoyo M Plan Apo 20 or similar objectives, inserted directly on each side of the DAC and in between the 45° mirrors and the DAC. This modification allows greater optical magnification and better imaging quality.

The possible objective changes in this LH system are at the base of its versatility (Fig. 4.2). In all cases, the collimated light, from the objectives, is directed from each side to two achromatic doublet lenses (AC) with a focal distance of 500 mm on the upstream side and 400 mm on the downstream side, then directed onto a germanium mirror placed at the entrance of the spectrometer, which was perforated with two pinholes of ∼40 mm diameter (Fig. 4.2) to collect the light from the laser hot spot simultaneously from both sides for temperature measurements. The mirror at the entrance of the spectrometer is titled by ∼17°. A camera observes the germanium mirror in front of the spectrometer and has a tilt of ∼34°. The tilt of the mirror and the camera eliminates the need for a beamsplitter in the path.

The DAC rests on a motorized x,y, and z stage, for independent alignment of the laser and the observation optics. An aluminum stage beneath the breadboard makes it mountable in the experimental end-station motorized stage, which allows the alignment of the entire system to the X-ray beam at the beamline. Piezo motors (Newport GmbH) control the other optical elements of the system (e.g., mirrors, plate rotators, iris, ...) that can be used remotely and incorporated into the beamline control system.

## 4.3 Imaging and temperature measurement in laser heating systems

There are two essential requirements for a laser heating (LH) system: (1) good sample imaging with high spatial resolution and (2) a reliable temperature measurement during heating (Jeanloz and Kavner, 1996). In laboratories, the sample imaging is achieved by lens objectives (refractive) or reflective objectives such as the Schwarzschild objectives but only refractive lenses can work as an on-axis heating

(i.e., where the image and IR laser share the same focusing path) (Fig. 4.3A). This on-axis geometry allows for more compact systems, and higher user-friendliness due to the fact that once the laser beam is aligned with the sample image, it does not need further alignments. At synchrotron facilities, the incident X-ray beam is aligned coaxially to the axis of the DAC. Therefore, on-axis heating is achieved by the combination of a lens objective and an X-ray transparent or perforated mirror tilted at 45° (Fig. 4.3B). This design, with an achromatic or apochromatic objective, is most common at XRD beamlines (Prakapenka et al., 2008; Meng et al., 2015; Aprilis et al., 2017; Fedotenko et al., 2019; Konôpková et al., 2021) but is also suitable for X-ray spectroscopy techniques if the upstream tilted mirror is sufficiently X-ray transparent or even perforated (Spiekermann et al., 2020; Kupenko et al., 2012). However, due to geometrical restrictions, the use of reflective Schwarzschild objectives requires off-axis heating (Fig. 4.3C) (Petitgirard et al., 2013), where the laser can be moved independently from the imaging optics. Therefore, commonly used reflective and refractive objectives cannot be exchanged without a major re-arrangement of optical elements.

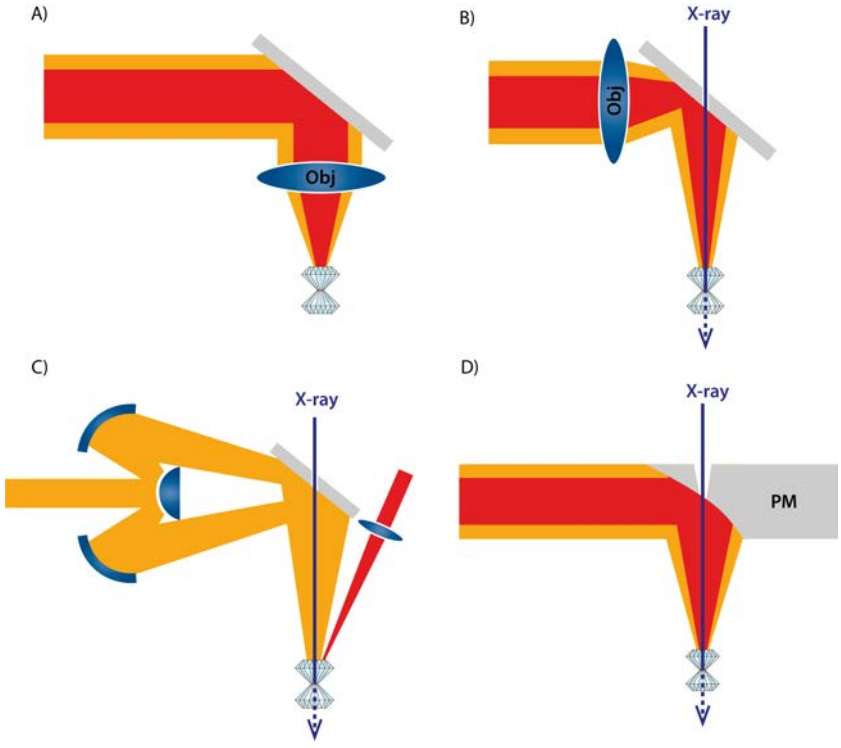


Figure 4.3: Sketches of different objective disposition for LH: (A) common laboratory geometry with an apochromatic objective for optical observation and on-axis laser focusing (B) Common synchrotron geometry with an apochromatic objective combined with a 45° tilted mirror and an X-ray beam (C) Reflective objective (Schwarzschild) combined with 45° tilted mirror. (d) Perforated parabolic mirror for use both in laboratory and synchrotron. The red path represents the laser beam and the orange path, the observation.

One of the recurrent problems of LH systems lies in providing accurate temperature estimation. The temperature is determined by radiospectrometry of the thermal emission of the hot spot (see section 2.2.2). This approach has various sources of errors. One possible source of error is the deviation of the thermal emission spectrum of a heated sample from the theoretical black body distribution (Deng et al., 2017), which is fitted to the recorded spectrum and in which the temperature is entered as a variable. Another type of error is directly related to spatial resolution. Laser heating spots have a high thermal gradient over a few micrometers, both radially and axially, and may result in the superposition of temperature signals (Campbell, 2008; Benedetti and Loubeyre, 2004). This effect can be reduced by achieving a high spatial resolution, using a short focal length objective. A third possible source of error is the possible temporal averaging of oscillating temperature, e.g. due to oscillations in laser power (Childs et al., 2020). Lastly, the most important error is due to spectral distortion by optical elements, in the first place by the chromatic aberration of lens objectives (Dewaele et al., 2003; Walter and Koga, 2004).This spectral distortion introduced by refractive objectives can be severe (Mezouar et al., 2017; Giampaoli et al., 2018). If present, the chromatic aberration will overprint any other possible distorting effect, and most critically will affect the accuracy of the calculated temperature that is sensitive to the wavelength distribution of the radiation, making it a major source of error for temperature measurement in LH-DAC experiments.

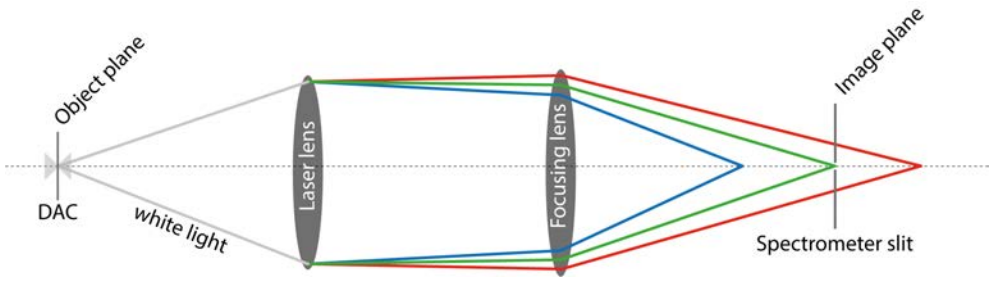


Figure 4.4: Schematic representation of chromatic aberration from a refractive lens system modified after (Walter and Koga, 2004) showing the $\lambda_{green}$ light focused at the spectrometer slit, the $\lambda_{blue}$ light has a shorted focal length and $\lambda_{red}$ light has a longer focal length.

Any refractive lenses in the optical path, that transmit light, would potentially introduce a chromatic dispersion. Indeed, the focal distance of refractive objectives depends on their wavelength-dependent refractive index (Walter and Koga, 2004). Therefore, refractive objectives present in an LH system, are chromatically dispers-

ing the light, also referred to as chromatic aberration. Wavelengths of the emitted light, from the heated spot in the DAC, are not focused on the detector plane and are missing from the spectrum (Walter and Koga, 2004) leading to an erroneous temperature calculation. This effect is schematically described in Fig. 4.4, where the $\lambda_{green}$ light is focused at the detector plane, whereas the shorted $\lambda_{blue}$ and the longer $\lambda_{red}$ wavelengths, are not focused on the detector plane due to the different focal lengths. Solutions exist to minimize these aberration effects, generally by using special apochromatic lenses or by introducing an iris in front of the objective, to reduce its aperture but this is at the expense of spatial resolution (Giampaoli et al., 2018).

On the other hand, reflective objectives, which utilize mirrors, are free from chromatic aberration and are therefore favorable for temperature determination (Petitgirard et al., 2013; Giampaoli et al., 2018). However, the commonly used reflective Schwarzschild objectives are not well suited for focusing of high-power lasers. Instead, the heating laser has to be focused and directed to the sample by separate additional optical elements. This situation has led to the separation of the synchrotron LH system into two categories, either the reflective off-axis or the refractive on-axis LH systems. This separation is the reason for the long-standing debate about the influence of chromatic aberration in LH systems using refractive objectives and on their reliability to provide accurate temperature measurements (Giampaoli et al., 2018; Mezouar et al., 2017; Petitgirard et al., 2013). A small reflective objective that allows for on-axis laser heating could bridge this gap. It could replace lens objectives in on-axis heating LH systems, at least on one side of an LH system, and result in wide-range temperature determinations with very low overall chromatic aberration.

The 90° parabolic mirror (PM), is a good candidate for such a compact on-axis heating reflective objective (Fig. 4.3D) and has not been described for imaging of DAC samples. Earlier attempts to use a PM for imaging in DAC may have been inhibited by the precise alignment required for non-aplanatic optical element (Laskin, 2021). However, the PM introduces, for the first time, on-axis laser heating, for fiber or $CO_2$ lasers, with reflective imaging and radiospectrometry free from chromatic aberration.

## 4.4 A parabolic mirror as imaging objective

The PM is an off-axis silver-coated 90° from Thorlabs (MPD01M9-P01) with a focal length of 33 mm and a 12.7 mm diameter. The PM replaces both the refractive objective and the 45° mirror in the upstream side of the LH system (Fig. 4.2d) by simultaneously focusing and deviating the laser beam and light (Fig. 4.3D). For alignment, the PM is fixed on a kinematic stage that allows precise x, y, and z movements and rotation.

### 4.4.1 Perforation for use at synchrotron facilities

To perform in situ laser heating at synchrotron facilities, the X-ray beam has to reach the sample with minimal attenuation, especially for X-ray spectroscopy measurements that mainly operate far below 20 keV (Kantor et al., 2018). To eliminate attenuation the PM was perforated in its central part, using an electric-discharge machine coaxially to its focusing axis. The perforation has a conical form with a hole at the mirror surface of 220 $\mu$m diameter (Fig. 4.5) and about 1 mm diameter in the backside.

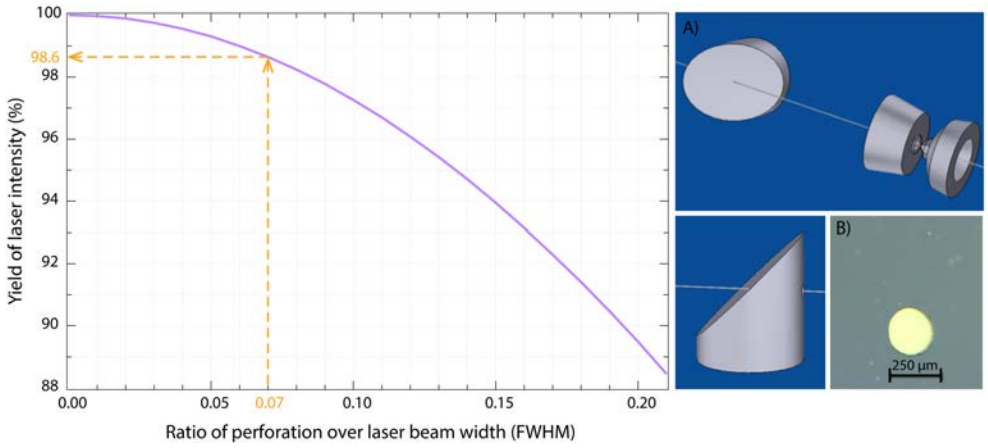


Figure 4.5: Ratio of perforation diameter over FWHM of the laser beam. At 0.07 ratio, indicating a hole of 220 $\mu$m diameter, the laser intensity is 98.6% indicating a loss of 1.4% due to the perforation. a) 3D model of the perforation of the PM. b) Photo of the surface of the PM showing the perforation of the mirror.

The perforation damaged the mirror exposing the aluminum substrate and leading to absorption and/or diffuse scattering of the laser beam. In order to quantify the amount of laser intensity lost due to the perforation, calculations were obtained by comparing the distribution of the 2D Gaussian intensity of identical width, of the

full one and the one excluding the central perforation. This calculation considers a $TEM_{00}$ laser beam of 3.2 mm diameter, and a perforation of 220 $\mu$m diameter, giving a diameter ratio of ~0.07 (3.2 ÷ 0.220 = 0.068). As well, it was assumed for this calculation that the perforation is located at the center of the beam, therefore it provides the maximal laser loss that can be expected from the perforation. From this parameter, the maximum intensity lost from the laser is expected to be around 1.4% (Fig. 4.5). This calculation also indicates that an even larger perforation could be afforded (≥400 $\mu$m) costing a loss of only 5% (ration= 0.13) and will facilitate the alignment with the X-ray beam. The use of a beam shaper ($\pi$-shaper, section 2.2.2) could also a widening of the collimated laser beam and lower this loss. Finally, minimum off-centering of the laser beam from the center of the mirror, where the perforation is, will also reduce this loss.

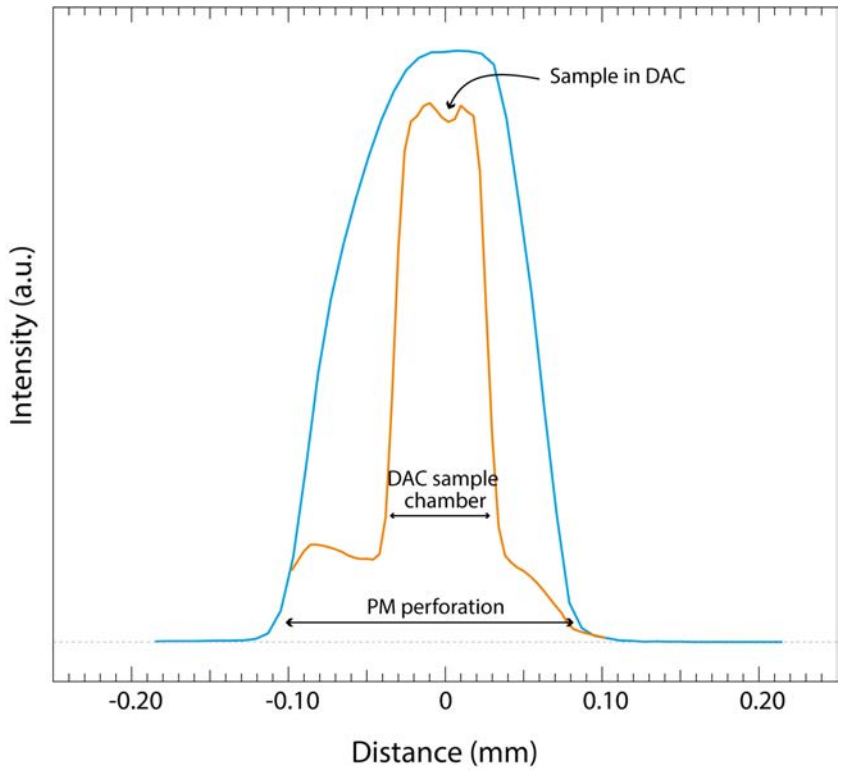


Figure 4.6: (a) Transmission scan obtained at the P01 beamline (PETRA III) using the LH system equipped with the PM. The red line is the scan obtained without a DAC, with the X-ray going through the perforation of the PM. The blue line is the scan obtained with a DAC containing a Fe-sample, ready for laser heating. Due to the attenuation by ~4 mm of diamond in the DAC, the curves were recorded with different gains of the diode and then scaled. The X-ray focus was 7 × 5$\mu m^2$ FWHM.

The alignment of the LH system with the X-ray is done in two steps. Firstly, the DAC is aligned within the LH system. Then the entire LH system can be moved and tilted from a motorized stage fixed to the aluminum construction beneath the breadboard, allowing alignment to the X-ray relative to the LH system. Translation scan profiles, in which PM and DAC are scanned horizontally across the focused X-ray beam, are then used for the alignment (Fig. 4.6) and are shown in Fig. 4.6.

### 4.4.2 Imaging and laser focus

Fig. 4.7 shows a comparison of images of a triangular Pt foil in NaCl, in a not-pressured DAC (a,b, and c) or transmission electron microscope sample grid (d, e, and f), taken with the PM, the achromatic objective placed at the downstream side of the LH, and from binocular at its highest magnification. Both images (achromatic objective and PM) have similar features visible in both images, which indicates that the PM provides a similar image quality to the apochromatic objective. The magnification achieved by using the PM is around 15×. When using two 20× Mitutoyo objectives are used the magnification can reach between 12× to 25×. However, with two geoHeat 60NIR objectives magnification only reaches 8.3 to 6.7×.

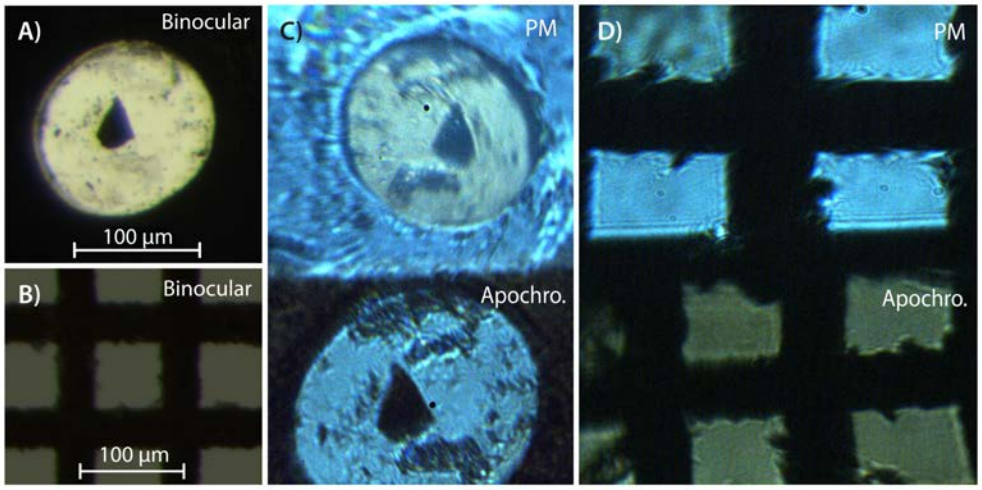


Figure 4.7: Photographs of platinum foil in the DAC (A and C) and TEM sample grid (B and D), recorded with a Leica M205 binocular (A and B), and with the LH system equipped with a PM and an apochromatic objective (C and D).

The laser focus quality of the PM was determined by measuring the IR laser spot size, using an optical beam profiler ($\pi$-shaper) (Fig. 4.8). The Gaussian fitted to the intensity distribution indicates a full width at half maximum (FWHM) of 9 $\mu$m (green line Fig. 4.8). This measurement is in good agreement with the calculated focal spot size or beam "waist" size ($2\omega_0$) of ~8.45 $\mu$m. The calculated size of the waist (i.e., when its diameter is at its minimum) of a focused Gaussian laser beam can be estimated following:

$$2\omega_0 = \frac{4f\lambda M^2}{\pi D} \tag{4.1}$$

where the focal length (f) of the PM is 33 mm, the laser wavelength $\lambda$= 1064 nm, $M^2$ is the beam quality factor of 1.04, and D=5.5 mm the diameter of the collimated laser beam at $1/e^2$ intensity. To overcome the small size of the laser spot as well as to provide the flat-top profile to reduce the radial temperature gradient (see section 2.2.2), a $\pi$-shaper is placed before the beamsplitter (Fig. 4.2) and produces a larger, more homogenous beam distribution of 21 $\mu$m (FWHM) (green line Fig. 4.8).

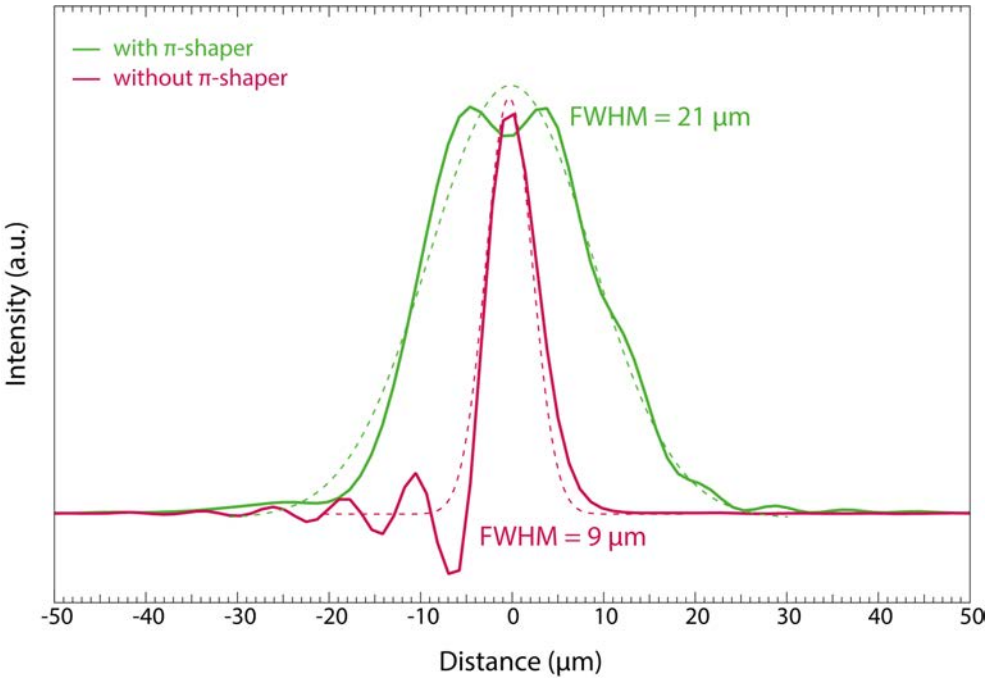


Figure 4.8: Laser focus profiles without and with a beam shaper ($\pi$-shaper). Dashed lines are Gaussian fits, used to derive FWHM values.

As stated earlier, the spatial resolution of optics in the LH system is an important factor for accurate temperature measurements. To characterize the spatial resolution of a system following the methods described in Kantor et al. (2018). A scan of a sharp edge, placed at the sample position in the focus of the system illuminated from the back, across the image provides intensity variations from which the linear resolution can be derived. The spatial resolution of the PM was found to be about 4 $\mu$m, regardless of the monochromatized light used (500, 650, or 800 nm using band pass color filters) and is the result of the diameter of the spectrometer entrance pinhole and the magnification of the system.

Although the implementation of PM in LH systems for both imaging and on-axis laser focusing has significant advantages, through our testing and playing, one of the limitations that occurred to us, is due to the image distortion and the difficulty of alignment. When using a single PM, the image plane will be tilted, resulting in a distortion of the image with part of it not focused (Malone et al., 2006). We tried to reduce this distortion by tilting the mirror at the entrance of the spectrometer. The other parameter for good image with PM is a precise rotational alignment, in the fraction of a degree, needed (Howard, 1979; Liu et al., 2011). However, the translational and tilt kinematic alignment stage used in our system does not allow enough degree of precision.

### 4.4.3 Temperature measurements

The light emitted from the hotspot, from each side, is collected in two spectra, for temperature calculations. To do so, first, the background, which was measured before heating, is subtracted from all measurements. Then the spectra are divided by the response function of the optical system to a calibrated spectrum of known temperature, obtained from a calibrated tungsten lamp. To finish, a Planck distribution function is fitted to the spectra. The fit process of the temperature is done using the software T-Rax by C. Prescher (github.com/CPrescher/T- Rax). The acquisition time of the temperature can be adapted during the measurements to avoid saturation but is usually set between 2 to 4 seconds.

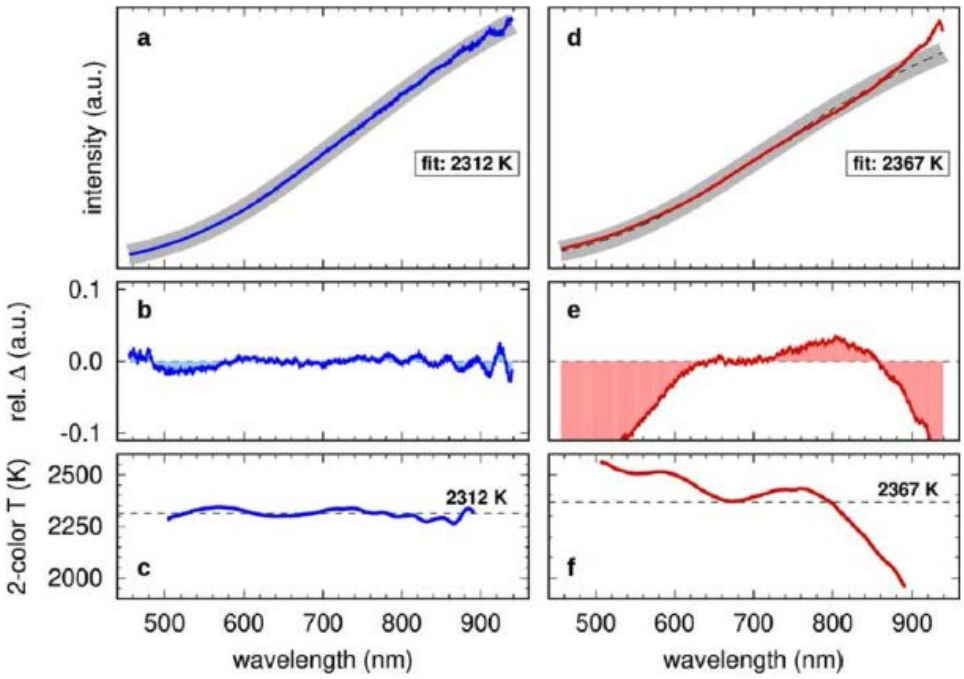


Figure 4.9: Comparison of radiospectrometric temperature determination with the parabolic mirror (a, b, and c) and the apochromatic objective (d, e, and f), and the influence of spectral distortion due to chromatic aberration on temperature determination taken from Spiekermann et al. (2021). (a,d): Spectrum, Planck fit, and resulting temperature estimate. (b,e): Relative difference of spectrum and fit, the difference is area-shaded for illustration. (c,f): Plot of two-color temperature (spacing of 100 nm). Dashed lines represent temperature determined from Planck fit.

One of the goals of using reflective objectives is to strongly reduce the chromatic aberration of the lens objectives. To demonstrate the performance of the PM and how strongly chromatic aberration is reduced by its use, the fitted temperature spectra (between 455 and 945 nm) from each side of the system, one with the PM and the other with an apochromatic objective, of a hot spot is shown in Fig. 4.9. Temperature fitted 500 to 900 nm from these two spectra are 2312 K and 2367 K. Even though all spectra visually agree well with the fit, the edge regions, from 450 to 500 nm and from 900 to 945 nm present some distortion effects, limiting the usability of these regions for temperature fitting. The lower edge part can be explained by inaccuracy in the background subtraction from the weak signal. Oscillation in the higher edge part of the spectra results from the detector coating. However, the range of the fitting can still be considered large (∼400 nm) compared to other LH systems.

In Fig. 4.9, the relative difference (rel. $\Delta$) and a two-color plot, of the same spectra are also shown. Indeed, to properly estimate the uncertainties or accuracy of the spectral temperature measurement a visual fitting agreement is not enough

and can be misleading. Therefore additional investigations such as the two-color technique are necessary to monitor wavelength-dependent distortion. This reveals the inaccuracies in the temperature calculation (Benedetti and Loubeyre, 2004; Giampaoli et al., 2018). The relative difference (rel. $\Delta$), between the spectra and the fits (Fig. 4.9b and e), shows, in the case of the PM an oscillation, mostly at the edges regions, but no systematic deviation. However, with the apochromatic objective, the deviation is more significant, and only in the region between 600 to ∼850 nm the deviation is minimal. The two-color technique is described in Giampaoli et al. (2018) and is based on a series of Wien's or Planck functions from pairs of spectral intensities separated by a fixed spectral difference such as:

$$T_{two-color}(\lambda) = \frac{(\frac{1}{\lambda}) - (\frac{1}{\lambda+\delta})}{Wien(\lambda) - Wien(\lambda+\delta)} \tag{4.2}$$

where $\delta$ is a chosen distance between the two selected wavelengths (here $\delta$= 100 nm) to calculate the temperature. The resulting plots are shown in Fig. 4.9 c and f. Ideally, in the absence of spectral distortion, the two-color plot should be flat, indicating a similar result to the temperature from a Planck fit, regardless of the wavelength window. This is well illustrated in Fig. 4.9c with the PM as objectives, and the average temperature of the two-color plot (2313 K) is very close to the Planck fit of the temperature. This is expected when using reflective objectives. Opposed to that, the side using the apochromatic objective shows a typical variation of temperature of several hundreds of kelvins, which are the result of spectral distortion, due to the chromatic aberration of the lens. Similarly, the average temperature of the two-color plot shows large deviation from the single Planck fit to the entire spectrum.

Here, the reported wavelength range for temperature measurement is larger than the one commonly used of 600 and 800 nm. The apochromatic objectives are also optimized for these wavelengths, and therefore, the two-color temperature variation is smaller. Furthermore, on off-axis LH systems, using an iris between DAC and imaging objective to reduce the numerical aperture, can suppress the chromatic aberration of an achromatic lens (Mezouar et al., 2017; Giampaoli et al., 2018; Kantor et al., 2018), at the price of the spatial resolution. However, this solution is not a viable solution for on-axis LH system, using common refractive objectives, since the iris will block the laser beam that needs to pass through the objective.

### 4.4.4 The future capabilities of the parabolic mirror

The PM is a new lightweight and cost-effecient innovation for LH systems, in laboratories or at synchrotron facilities, for temperature measurements free from chromatic aberration and a wider temperature range. However, its greatest potential lies in its future application when using $CO_2$ lasers (see section 2.2.2).

$CO_2$ lasers have several advantages, due to their longer wavelength ($\lambda$= ~10.6 $\mu$m) they have (1) the ability to heat optically transparent minerals, oxides, and organic materials (Salamat et al., 2014) directly removing the requirement to add of metallic couplers in the experiment (2) a larger focal size leading to a heating spot of ~50 $\mu$m diameter and (3) unlike NIR lasers in which the laser radiation is absorbed primarily at the surface, $CO_2$ lasers have higher penetration depths throughout the entire thickness of the sample, removing the need for double-sided laser heating. Accordingly, using a $CO_2$ LH system is ideal when considering synchrotron techniques that rely on data collection in the transmitted signal (downstream) such as XRD. It enables the placement of all optical elements on only one side of the DAC (upstream) and removes all optical elements from the other side (downstream), often placed in the path of the emitted signal, which can affect the data quality.

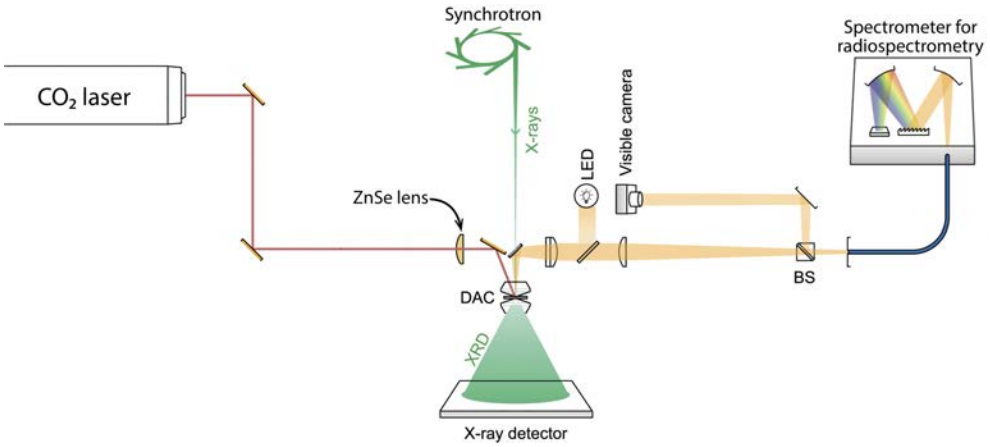


Figure 4.10: Simplified diagram of the $CO_2$ laser heating system in place at the HP-CAT 16-ID-B diffraction beamline (University of Nevada Las Vegas, USA) modified after Smith et al. (2018), demonstrating the off-axis laser relative to the X-ray.

Even though $CO_2$ LH systems have been implemented with XRD measurement techniques in several beamlines since the 1990s (Brister and Bassett, 1995; Fiquet et al., 1996), and are available at most XRD beamlines (Petitgirard et al., 2013; Murakami et al., 2009; Smith et al., 2018; Konôpková et al., 2021), their use remains limited to very few specialized research groups. NIR LH systems are often preferred for LH-DAC experiments when combined with synchrotron X-ray measurements. The main reason for this withholding comes from the need for special optics, such as ZnSe focusing lenses (Kurnosov et al., 2019; Smith et al., 2018) since typical optical glasses absorb $CO_2$ laser light strongly, requiring the observation path to be separated from the laser one. This aspect makes on-axis geometry, wherein the laser radiation enters coaxially to the X-ray unachievable. Therefore, most of the $CO_2$ LH systems have used an off-axis geometry, with the incident laser beam entering the DAC with some angle ($\sim$30 to 40°), as displayed in Fig. 4.10. However, this geometry imposes constraints, with the major one being the very challenging alignment of the laser into the DAC, due to the refraction of the beam from the diamonds, reducing the user-friendliness of such LH systems.

This is why, the (perforated) PM opens the way for a new generation of LH systems at synchrotron facilities when applied to $CO_2$ laser since it can be placed on-axis, as a focusing lens for $CO_2$ laser and for imaging, abolishing the separated paths and the special ZnSe objective previously needed to focus the $CO_2$ laser. This promising future for $CO_2$ LH system with PM at XRD beamlines, will open a new path for low background scattering high-pressure and high-temperature XRD experiments in DAC, by removing all optical elements in the diffracted signal.

## 4.5 Summary

The versatile, portable NIR LH system, optimized for near-90° scattering angle, has been developed at the University of Potsdam, in tight collaboration with Dr. Georg Spiekermann. The versatility of this system comes from its different designs that allow for: (1) laboratory laser heating with high magnification using two apochromatic objectives, (2) in situ X-ray spectroscopy techniques such as XES and NIS at synchrotron facilities, that have been used by different groups and for different projects and led to the acquisition of new data (Mergner et al., 2021; Albers et al., 2022, 2023; Müller et al., 2022; Kupenko et al., 2022) and finally, (3) the new development,

adopting a parabolic mirror as a reflective objective for both in laboratory and synchrotron radiation facilities, was initiated, with great future promises. With the PM, the separation of synchrotron LH systems in "exclusively reflective" and "exclusively refractive" can be overcome, as the PM can be installed instead of a refractive objective and its bending mirror.

### 4.5.1 Work achieved with the laser heating system

The demand for in situ X-ray emission spectroscopy at extreme pressure and temperature is growing. This LH system was the first portable one with which high-pressure and temperature XES measurements were reported (Weis et al., 2019), and one of the few LH systems worldwide allowing for laser-heated NIS measurements. The possibility given by this LH system has led to recently published and upcoming data sets providing new constraints in the understanding of the deep Earth's interior.

Utilizing this LH system, NIS measurements were done at the high-resolution dynamics beamline (P01) at PETRA III. The resulting studies, led by Dr. Ilya Kupenko (University of Münster and European Synchrotron Radiation Facility, ESRF), on the sound velocities have revealed (1) a new possible candidate material, B2-structured FeSi, for the ultra-low velocity zones (ULVZs) by Mergner et al. (2021) and (2) now explore the possible presence of carbon and other light elements in the Earth's inner core by investigating the stability, elastic and plastic properties at core temperatures of Fe-Si-C alloys by Müller et al. (2022) and $Fe_7C_3$ by Kupenko et al. (2022).

The combination of laser heating and XES utilizing a wavelength-dispersive von Hámos spectrometer shows a promising combination for XES measurements. The recent in situ investigations of siderite ($FeCO_3$) at lower mantle conditions have shown the formation of tetrahedrally coordinated $Fe_2^{2+}Fe_2^{3+}C_4O_{13}$ with both ferric and ferrous iron at high-spin state, proposing it as a Fe-bearing carbonate present in subducted slabs (Albers et al., 2022). Finally, this system has the great potential to investigate samples at extreme conditions using less established measurement techniques such as valence-to-core XES (Weis et al., 2019; Spiekermann et al., 2019; Albers et al., 2023), HERFD-XANES and X-ray Raman scattering spectroscopy (Sternemann and Wilke, 2016; Weis et al., 2019) for future applications.

# 5 | Conclusive remarks and outlook

The first objective of this thesis is to investigate to which depths magnesite contained in subducting slabs can carrie and whether or not carbonate minerals can be a reservoir of oxidized carbon into the deep lower mantle.

The first objective of this thesis is to investigate whether or not magnesite contained in subducting slabs is a possible carrier and reservoir of oxidized carbon into the deep lower mantle. To answer this, the stability of magnesite with iron-bearing lower mantle assemblages was re-assessed from high-pressure and high-temperature experiments. The data obtained from the multi-anvil apparatus and laser-heated diamond anvil cells are complementary and show that already at the upper-most lower mantle conditions, magnesite is not stable when in contact with lower mantle silicate, at cold slab temperatures (1350 K) and upper-most lower mantle conditions (33 GPa). However, differences are observed depending on the techniques used. In multi-anvil experiments (25 GPa), the presence of magnesite induces the formation of carbonate-rich melt at temperatures corresponding to all geotherms except the coldest one (1500 to 2000 K). On the other hand, the formation of diamonds in laser-heated diamond anvil cell experiments demonstrates magnesite decomposition at temperatures relevant to and lower than the coldest slab geotherm (1350 K at 33 GPa). This difference observed in the speciation of carbon (carbonate-melt versus diamond) in run products is interpreted to be due to the difference in the redox conditions ($fO_2$) of each experimental apparatus; oxidized in multi-anvil experiments and reduced in LH-DAC experiments. This highlights that the $fO_2$ is, therefore, one of the key parameters controlling the form, mobility (e.g., oxidized and mobile or reduced and immobile), and the residence time of carbon in the deep Earth. Along with fugacity-

controlled reactions, such as redox melting and/or freezing (see section 1.2.2) that offer a transition medium between oxidized and reduced forms of carbon. Accordingly, the requirements to further constrain the deep carbon cycle and the different (re)cycling processes, rely on a better understanding of the stable carbon-bearing phases and their abundances at pressure, temperature, and $fO_2$ values of redox conditions of the Earth's interior. Therefore, to provide new insight into the fate of subducted carbonates, future experimental investigations should obviously integrate the $fO_2$ as a controlled parameter, consider more chemically complex systems with a wide range of carbonates and silicate compositions, and should include reaction kinetics.

This work reveals several points that require further assessment. From the experimental point of view, most of the experiments performed were done in LH-DACs and only a few were done using multi-anvil apparatuses. To complete our data set, future work should include (1) a wider range of temperatures at 25 GPa to locate the solidus curve in the investigated system and (2) the addition of solid-state buffers in experiments, that cover a broad range of redox conditions, as well as an LH-DAC experiment at conditions similar to the multi-anvil experiments (25 GPa). This will aid to connect together the two experimental set-ups more robustly. Extension of this work with large-volume press experiments would be also beneficial, allowing for investigations of complex multi-phase systems, elemental partitioning, and partial melting in a more reachable way than the ones possible by LH-DAC experiments. However, achieving pressure $\geq$25 GPa more routinely is still limited. Therefore, technical advancements in multi-anvil apparatuses, reaching higher pressure routinely will also benefit the community to get a more complete picture of the processes occurring in the deepest Earth's mantle portions. Furthermore, a recent innovation to probe internally the $fO_2$ in LH-DAC experiments using Fe-Ir redox sensor has been proposed in Dominijanni (2022). This is the first step for better determination $fO_2$ in LH-DAC experiments and opens future investigations of mantle processes under known redox conditions under extreme conditions.

Recent studies have revealed that Fe-bearing carbonate phases present complex chemical and physical behavior. They transform into tetrahedrally coordinated phases at mid-lower mantle pressure ($\sim$40 GPa for Fe-rich composition and $\sim$80 GPa for Mg-rich compositions) (Boulard et al., 2011; Cerantola et al., 2017; Boulard et al., 2020; Albers et al., 2022). The transformation to high-pressure structures impacts their thermodynamic properties, and, therefore, they might be another phase to be taken into account as oxidized carbon reservoirs and fluxes in the lower mantle. In

addition, the $Fe^{2+}$ spin transition in these iron-bearing phases, shifts the chemical equilibrium toward a Fe-rich composition, which also will impact their physical properties. Whether these phases are present and remain stable in subducting slabs still needs to be investigated.

The recent advancements made in laser-heating systems presented in Chapter 4, have allowed overcoming one of the technical challenges of probing spin transitions in situ in LH-DAC at high-pressure and high-temperature conditions, as for $FeCO_3$ (Albers et al., 2022, 2023). As in situ XES becomes more and more available in the future and at diverse synchrotron beamlines, the effect of the Fe spin transition in the Earth's mantle will be better understood. Furthermore, the use of a parabolic mirror in $CO_2$ LH systems has also been considered by several groups working at synchrotron facilities. If this is successful, more routinely and user-friendly $CO_2$ LH will be available in the near future at Extreme conditions synchrotron beamlines, providing more globally the several advantages of $CO_2$ laser heating for diamond anvil cells experiments.

# A | Appendix Chapter 2

## A.1 Unused starting materials

**Doped magnesite:** Following the former idea that for the doped silicate glass (See section 2.1), an attempt to synthesize Sr,La and Eu doped magnesite was made, using a cold seal pressure vessel (CPV) and piston-cylinder (PC) at the High-Pressure Laboratory for Geomaterial Sciences at the GeoForschungsZentrum (GFZ) in Potsdam (Germany). Natural magnesite powder was mixed with commercially purchased powders of $SrCO_3$ for Sr doped magnesite or with $La_2(CO_3)_3 \cdot x\,H_2O$ (x = 2.0–5.0) or $La_2O_3$. Samples were loaded in platinum capsules. CPV experiments were performed between 3.9 kbar and 4.5 kbar (0.39 to 0.45 GPa) and 650 °C for 3 weeks and PC experiments were performed at 1 to 2 GPa and 600 to 1200 °C. After experiments, the CPV run products revealed in all experiments two phases with no detectable partitioning of Sr or La into magnesite, leading to the use of the PC, to reach higher temperatures to encourage faster diffusion. Those samples remained unused after we could incorporate trace elements in the silicate glass with less difficulty.

| Run | Pressure (GPa) | T (°C) | Duration | powder mixtures |
|---|---|---|---|---|
| **Cold-Pressure vessel experiments** | | | | |
| MgD2 | 0.39 | 650 | 20d | $MgCO_3$ + $La_2O_3$ |
| MgD3 | 0.45 | 650 | 20d | $MgCO_3$ + $SrCO_3$ |
| MgD4 | 0.45 | 650 | 20d | $MgCO_3$ + $La_2(CO_3)_3 \cdot x\,H_2O$ |
| **Pyston Cylinder experiments** | | | | |
| MgD5 | 1 | 1200 | 5h | $MgCO_3$ + $La_2O_3$ |
| MgD6 | 2 | 600 | 12h | $MgCO_3$ + $La_2(CO_3)_3 \cdot x\,H_2O$ |
| MgD7 | 2 | 1200 | 2d | $MgCO_3$ + $SrCO_3$ |

Table A.1: Pressure, temperature and duration conditions of doped magnesite experiments trials. h= hours, d= days

## Appendix A

**Doped basaltic glass:** A simplified basaltic composition glass containing Si, Al, Fe, Mg, Ca and doped with similar trace elements, Sr, La, and Eu (Tab A.2) was synthesized in order to increase the complexity of the system after exploration of the magnesite-bridgmanite system and to investigate magnesite interaction with a MORB composition. The synthesizing was done at the University of Potsdam in an oven first and then in atmosphere-controlled furnaces under reduced conditions to limit the amount of $Fe^{3+}$.

| Elements | Basaltic glass | Basaltic glass:Sr | Basaltic glass:La | Basaltic glass:Eu |
|---|---|---|---|---|
| $SiO_2$ | 48.56 | 48.25 | 48.35 | 48.26 |
| $Al_2O_3$ | 15.99 | 15.75 | 15.74 | 15.67 |
| FeO | 4.00 | 3.89 | 3.84 | 3.90 |
| MgO | 7.82 | 8.07 | 8.09 | 8.09 |
| CaO | 23.09 | 22.94 | 22.85 | 22.90 |
| SrO | - | 0.48 | - | - |
| $La_2O_3$ | - | - | 0.39 | - |
| $Eu_2O_3$ | - | - | - | 0.51 |
| Total | 99.61 | 99.57 | 99.41 | 99.48 |

Table A.2: Simplified basaltic glass composition measured at the EPMA (wt%).

# B | Appendix Chapter 3

## B.1 Multi anvil experiments

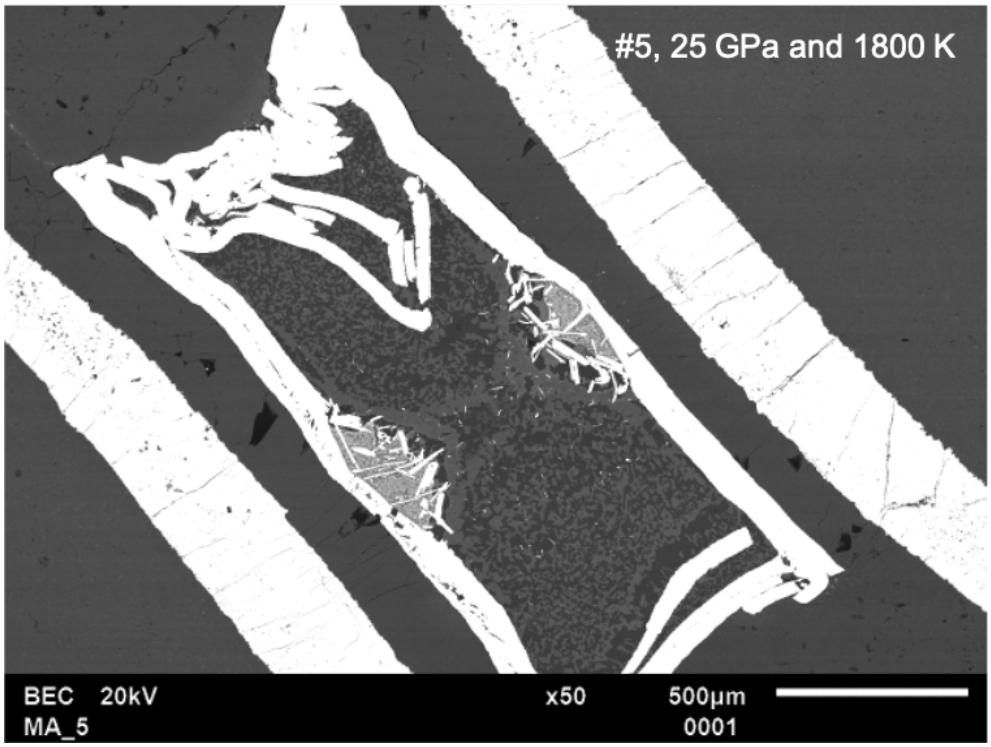


Figure B.1: Back-scatter electron images of n°#5 multi-anvil experiments.

## Appendix B

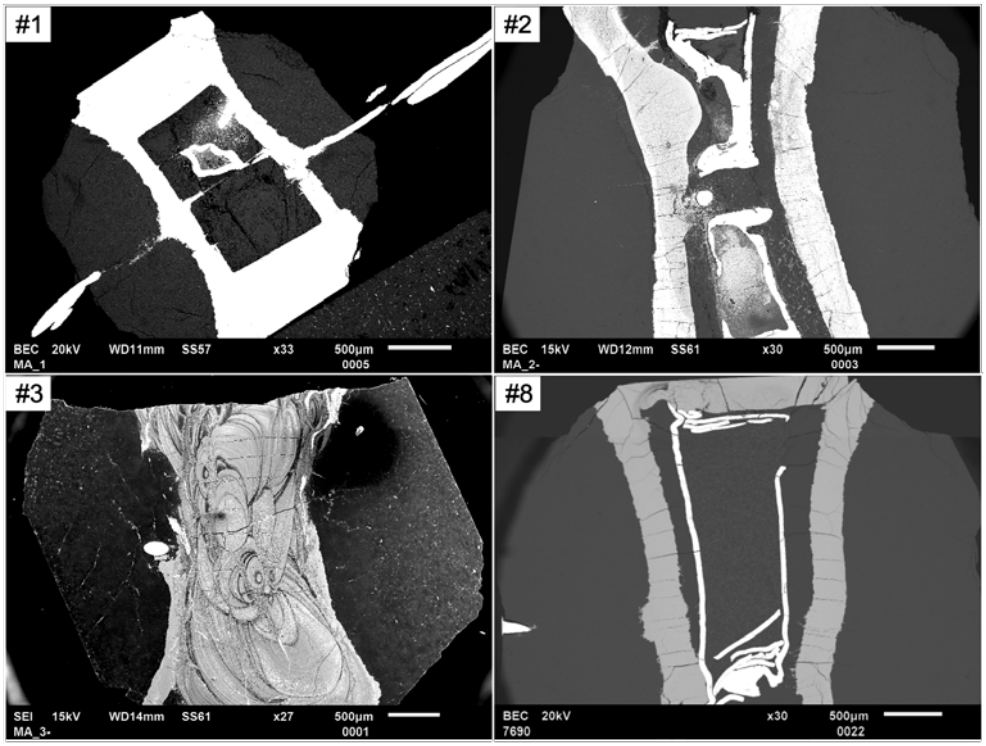


Figure B.2: Back-scatter electron images of failed multi-anvil experiments.

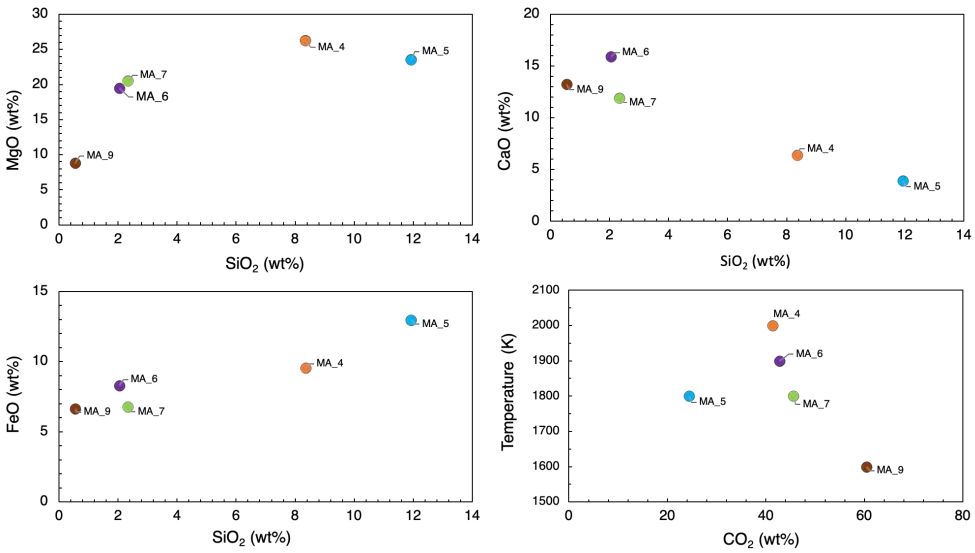


Figure B.3:

| Phase | $SiO_2$ | $Al_2O_3$ | FeO | MgO | CaO | $K_2O$ | $Na_2O$ | $ReO_2$ | $La_2O_3$ | SrO | $CO_2$ ($^a$) | Total | Mg#($^b$) |
|---|---|---|---|---|---|---|---|---|---|---|---|---|---|
| **#4, 2000 K** | | | | | | | | | | | | | |
| Bdg(46) | 56.47(1.09) | 0.51(0.08) | 7.48(1.19) | 35.90(1.38) | 0.15(0.04) | - | <0.02 | - | <0.05 | <0.01 | - | 100.57 | 89.27 |
| Mgs(19) | - | - | 4.34(0.68) | 43.94(0.85) | 0.29(0.08) | - | <0.02 | - | <0.1 | <0.01 | 51.35 | | 94.32 |
| St(1) | 89.64 | 0.22 | 1.13 | 7.08 | <0.01 | - | <0.02 | - | <0.05 | <0.01 | - | 98.17 | |
| QM(3) | 8.36(1.51) | 0.01(0.02) | 9.53(0.28) | 26.26(0.59) | 6.39(0.41) | - | 0.43(0.08) | - | 5.0(1.28) | 2.66(2.31) | 41.36(1.33) | | 72.54 |
| Fp(5) | 0.15(0.23) | 0.06(0.02) | 26.73(1.64) | 74.27(1.95) | <0.01 | - | <0.02 | - | 0.00 | 0.00 | | 101.3 | 83.21 |
| **#6, 1900 K** | | | | | | | | | | | | | |
| Bdg(34) | 55.65(1.06) | 0.68(0.05) | 9.00(1.06) | 33.64(1.21) | 0.16(0.11) | <0.01 | - | <0.1 | <0.2 | <0.05 | - | 99.43 | 86.66 |
| Mgs(16) | - | - | 5.39(0.40) | 43.17(1.56) | 0.37(0.11) | - | <0.02 | <0.1 | <0.05 | 0.00 | 50.90(1.41) | | 92.92 |
| St(6) | 97.45(1.83) | 0.22(0.07) | 0.36(0.20) | 0.72(0.87) | <0.01 | 0.00 | - | <0.1 | <0.05 | <0.05 | - | 98.79 | |
| QM(4) | 2.04(0.83) | - | 8.30(0.46) | 19.46(2.14) | 15.9(1.53) | 1.6(0.29) | - | <0.2 | 8.70(1.40) | <0.1 | 42.73(2.05) | | 53.35 |
| (Re,Fe,Mg)O (1) | 1.87 | - | 33.00 | 1.91 | 1.29 | <0.02 | - | 51.37 | 1.83 | <0.1 | - | 91.38 | 8.97 |

Table B.1: Chemical composition of run products of multi-anvil press experiments in wt%. $^a$Calculated from the total deficit from the analyses. Numbers in parentheses next to the phase names are the number of analyses averaged. The number in parentheses next to the measurement refers to the standard deviation ($1\sigma$). $^b$Mg number, Mg# =[Mg/(Mg+Fe+Ca)]×100 . Phases: Bdg = bridgmanite, Mgs = magnesite, Sti = stishovite, QM = quenched melt, Mw = magnesiowüstite.

| Phase | $SiO_2$ | $Al_2O_3$ | FeO | MgO | CaO | $K_2O$ | $Na_2O$ | $ReO_2$ | $La_2O_3$ | SrO | $CO_2$ ($^a$) | Total | Mg#($^b$) |
|---|---|---|---|---|---|---|---|---|---|---|---|---|---|
| **#5, 1800 K** | | | | | | | | | | | | | |
| Bdg(38) | 54.34(3.11) | 0.62(0.17) | 7.38(1.23) | 33.26(1.78) | 0.05(0.08) | <0.02 | - | 0.45(1.15) | <0.05 | <0.05 | - | 96.51 | 88.70 |
| Mgs(34) | - | - | 3.66(1.02) | 44.51(1.18) | 0.25(0.10) | <0.01 | <0.02 | <0.1 | <0.05 | <0.02 | 51.26(1.10) | | 95.22 |
| St(4) | 97.82(0.91) | 0.23(0.10) | 0.19(0.22) | 0.19(0.32) | <0.01 | - | - | <0.2 | <0.1 | <0.05 | - | 98.84 | |
| QM(6) | 11.93(1.19) | - | 12.92(1.06) | 23.54(1.87) | 3.94(1.04) | 0.39(0.13) | - | 13.70(2.98) | 8.72(1.96) | <0.1 | 24.37 | | 69.94 |
| **#7, 1800 K** | | | | | | | | | | | | | |
| Bdg(43) | 55.24(3.62) | 0.71(0.20) | 7.93(1.16) | 34.10(1.08) | 0.11(0.09) | 0.00 | - | <0.1 | <0.2 | <0.1 | | 98.49 | 88.26 |
| Mgs(36) | - | - | 4.76(0.75) | 44.09(1.08) | 0.29(0.19) | <0.01 | <0.02 | <0.1 | <0.04 | <0.02 | 50.69(0.80) | | 93.86 |
| St(5) | 98.00(0.93) | 0.38(0.07) | 0.30(0.13) | 0.05(0.14) | <0.01 | 0.00 | | <0.1 | <0.1 | <0.05 | | 99.06 | |
| QM(6) | 2.33(0.89) | - | 6.76(1.01) | 20.56(4.87) | 11.93(2.25) | 0.69(0.26) | - | 0.88 | 1.72(0.64) | 7.85(2.74) | 45.61 | | 61.79 |
| ReO(8) | <0.05 | 0.00 | 1.10 | <0.02 | <0.01 | <0.02 | - | 96.55(3.19) | <0.1 | 0.00 | | 97.93 | - |
| (Re,Fe,Mg)O(7) | 1.46(0.36) | 0.00 | 28.71(1.15) | 3.39(0.25) | 1.25(0.31) | <0.02 | - | 55.78(1.71) | 0.49(0.63) | 0.38(0.48) | | 91.74 | 16.66 |
| **#9, 1600 K** | | | | | | | | | | | | | |
| Bdg(20) | 55.89(2.53) | - | 8.17(0.88) | 32.13(2.30) | 0.13(0.04) | <0.01 | - | <0.1 | <0.2 | <0.1 | - | 96.62 | 87.28 |
| Mgs(21) | - | - | 5.50(1.38) | 41.32(1.14) | 0.19(0.10) | <0.01 | - | <0.1 | <0.2 | <0.1 | 52.64 | | 92.75 |
| St(4) | 95.89(2.05) | - | 0.49(0.07) | 0.08(0.00) | <0.01 | <0.01 | - | <0.1 | <0.2 | <0.1 | - | 96.68 | |
| QM(4) | 0.55(017) | - | 6.63(0.97) | 8.85(7.97) | 13.25(4.32) | 2.18(0.75) | - | 0.00 | 7.34(2.92) | 0.69(0.13) | 60.48(1.80) | | 35.91 |
| La-Silicate(4) | 40.60(9.83) | - | 2.89(0.33) | 10.24(3.36) | 29.21(6.40) | <0.02 | - | <0.2 | 6.61(3.15) | <0.2 | - | 89.95 | 41.40 |

Table B.2: continued.

## B.2 LH-DAC experiments

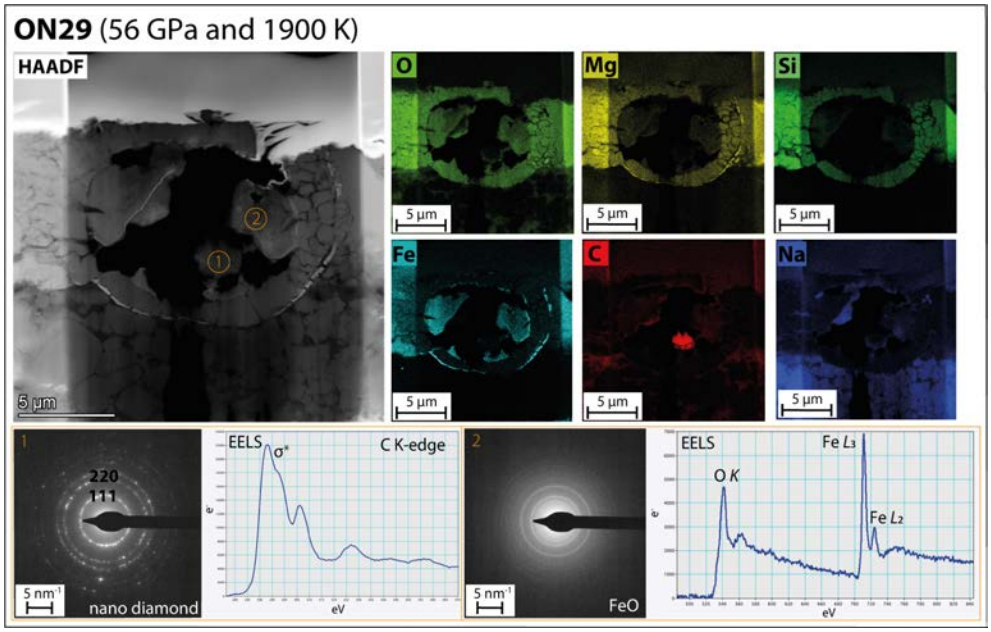


Figure B.4: Ex situ TEM analyses of the run ON29 (56 GPa and 1900 K) showing dark-field STEM image (HAADF), chemical maps for oxygen, magnesium, silicon, iron, carbon, and sodium. Electron diffraction on diamond and wüstite (FeO) associated with EELS spectra of C K-edge and Fe$L_{3,2}$ measurement.

# C | Appendix Chapter 4

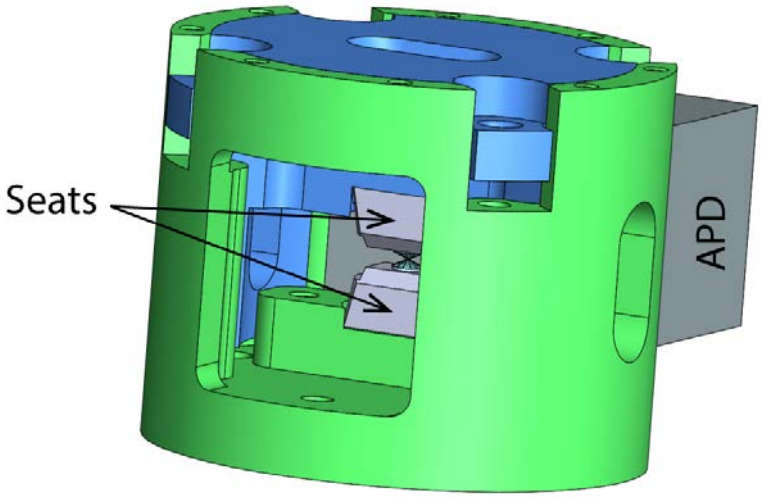


Figure C.1: 3D-views of the panoramic DAC design for NIS measurement allowing the insertion of a large APD detector (22 mm × 22 mm) modified after Mergner et al. (2021).

# References


Akahama, Y., Kawamura, H., 2006. Pressure calibration of diamond anvil Raman gauge to 310 GPa. Journal of Applied Physics 100, 043516. doi:10.1063/1.2335683.

Albers, C., Sakrowski, R., Libon, L., Spiekermann, G., Winkler, B., Schmidt, C., Bayarjargal, L., Cerantola, V., Chariton, S., Giordano, N., Gretarsson, H., Kaa, J., Liermann, H.P., Sundermann, M., Thiering, N., Tolan, M., Wilke, M., Sternemann, C., 2022. $Fe^{3+}$-hosting carbon phases in the deep Earth. Physical Review B 105, 085155. doi:10.1103/physrevb.105.085155.

Albers, C., Sakrowski, R., Thiering, N., Libon, L., Spiekermann, G., Kaa, J.M., Gretarsson, H., Sundermann, M., Tolan, M., Wilke, M., Sternemann, C., 2023. High-efficient X-ray emission spectroscopy of cold-compressed /ceFe2O3 and laser-heated pressurized /ceFeCO3 using a von Hámos spectrometer. Journal of Analytical Atomic Spectrometry doi:10.1039/d3ja00014a. (in review).

Andrault, D., Fiquet, G., Itié, J.P., Richet, P., Gillet, P., Häusermann, D., Hanfland, M., 1998. Thermal pressure in the laser-heated diamond-anvil cell: An X-ray diffraction study. European Journal of Mineralogy 10, 931–940. doi:10.1127/ejm/10/5/0931.

Anzellini, S., Boccato, S., 2020. A practical review of the laser-heated diamond anvil cell for university laboratories and synchrotron applications. Crystals 10, 459. doi:10.3390/cryst10060459.

Anzellini, S., Kleppe, A.K., Daisenberger, D., Wharmby, M.T., Giampaoli, R., Boccato, S., Baron, M.A., Miozzi, F., Keeble, D.S., Ross, A., Gurney, S., Thompson, J., Knap, G., Booth, M., Hudson, L., Hawkins, D., Walter, M.J., Wilhelm, H., 2018. Laser-heating system for high-pressure X-ray diffraction at the Extreme Conditions beamline I15 at Diamond Light Source. Journal of Synchrotron Radiation 25, 1860–1868. doi:10.1107/s1600577518013383.

Aprilis, G., Strohm, C., Kupenko, I., Linhardt, S., Laskin, A., Vasiukov, D.M., Cerantola, V., Koemets, E.G., McCammon, C., Kurnosov, A., Chumakov, A.I., Rüffer, R., Dubrovinskaia, N., Dubrovinsky, L., 2017. Portable double-sided pulsed laser heating system for time-resolved geoscience and materials science applications. Review of Scientific Instruments 88, 084501. doi:10.1063/1.4998985.

Asanuma, H., Ohtani, E., Sakai, T., Terasaki, H., Kamada, S., Kondo, T., Kikegawa, T., 2010. Melting of iron-silicon alloy up to the core-mantle boundary pressure: implications to the thermal structure of the Earth's core. Physics and Chemistry of Minerals 37, 353–359. doi:10.1007/s00269-009-0338-7.

Auzende, A.L., Gillot, J., Coquet, A., Hennet, L., Ona-Nguema, G., Bonnin, D., Esteve, I., Roskosz, M., Fiquet, G., 2011. Synthesis of amorphous MgO-rich peridotitic starting material for laser-heated diamond anvil cell experiments – application to iron partitioning in the mantle. High Pressure Research 31, 199–213. doi:10.1080/08957959.2011.556631.

Ballhaus, C., 1995. Is the upper mantle metal-saturated? Earth and Planetary Science Letters 132, 75–86. doi:10.1016/0012-821x(95)00047-g.

Benedetti, L.R., Loubeyre, P., 2004. Temperature gradients, wavelength-dependent emissivity, and accuracy of high and very-high temperatures measured in the laser-heated diamond cell. High Pressure Research 24, 423–445. doi:10.1080/08957950412331331718.

Binck, J., Bayarjargal, L., Lobanov, S.S., Morgenroth, W., Luchitskaia, R., Pickard, C.J., Milman, V., Refson, K., Jochym, D.B., Byrne, P., Winkler, B., 2020. Phase stabilities of $MgCO_3$ and $MgCO_3$-II studied by Raman spectroscopy, X-ray diffraction, and density functional theory calculations. Physical Review Materials 4, 055001. doi:10.1103/physrevmaterials.4.055001.

Birch, F., 1964. Density and composition of mantle and core. Journal of Geophysical Research 69, 4377–4388. doi:10.1029/jz069i020p04377.

Blanchard, I., Siebert, J., Borensztajn, S., Badro, J., 2017. The solubility of heat-producing elements in Earth's core. Geochemical Perspectives Letters , 1–5doi:10.7185/geochemlet.1737.

Boccato, S., Torchio, R., Kantor, I., Morard, G., Anzellini, S., Giampaoli, R., Briggs, R., Smareglia, A., Irifune, T., Pascarelli, S., 2017. The Melting Curve of Nickel Up to 100 GPa Explored by XAS. Journal of Geophysical Research: Solid Earth 122, 9921–9930. doi:10.1002/2017jb014807.

Boehler, R., 2000. High-pressure experiments and the phase diagram of lower mantle and core materials. Reviews of Geophysics 38, 221–245. doi:10.1029/1998rg000053.

Boehler, R., 2006. New diamond cell for single-crystal X-ray diffraction. Review of Scientific Instruments 77, 115103. doi:10.1063/1.2372734.

Boehler, R., Hantsetters, K.D., 2004. New anvil designs in diamond-cells. High Pressure Research 24, 391–396. doi:10.1080/08957950412331323924.

Boulard, E., Gloter, A., Corgne, A., Antonangeli, D., Auzende, A.L., Perrillat, J.P., Guyot, F., Fiquet, G., 2011. New host for carbon in the deep earth. Proceedings of the National Academy of Sciences 108, 5184–5187. doi:10.1073/pnas.1016934108.

Boulard, E., Guyot, F., Fiquet, G., 2020. High-Pressure Transformations and Stability of Ferromagnesite in the Earth's Mantle, in: Craig E. Manning, Jung-Fu Lin, W.L.M. (Ed.), Carbon in Earth's Interior. Wiley, pp. 105–113. doi:10.1002/9781119508229.ch11.

Bragg, W.L., 1914. The analysis of crystals by the X-ray spectrometer. Proceedings of the Royal Society of London. Series A, Containing Papers of a Mathematical and Physical Character 89, 468–489. doi:10.1098/rspa.1914.0015.

Brenker, F.E., Vollmer, C., Vincze, L., Vekemans, B., Szymanski, A., Janssens, K., Szaloki, I., Nasdala, L., Joswig, W., Kaminsky, F., 2007. Carbonates from the lower part of transition zone or even the lower mantle. Earth and Planetary Science Letters 260, 1–9. doi:10.1016/j.epsl.2007.02.038.

Brister, K., Bassett, W., 1995. $CO_2$ laser heating instrumentation at CHESS. Review of Scientific Instruments 66, 2698–2702. doi:10.1063/1.1146449.

Bulanova, G.P., Walter, M.J., Smith, C.B., Kohn, S.C., Armstrong, L.S., Blundy, J., Gobbo, L., 2010. Mineral inclusions in sublithospheric diamonds from collier 4 kimberlite pipe, juina, brazil: subducted protoliths, carbonated melts and primary kimberlite magmatism. Contributions to Mineralogy and Petrology 160, 489–510. doi:10.1007/s00410-010-0490-6.

Campbell, A.J., 2008. Measurement of temperature distributions across laser heated samples by multispectral imaging radiometry. Review of Scientific Instruments 79, 015108. doi:10.1063/1.2827513.

Cerantola, V., Bykova, E., Kupenko, I., Merlini, M., Ismailova, L., McCammon, C., Bykov, M., Chumakov, A.I., Petitgirard, S., Kantor, I., Svitlyk, V., Jacobs, J., Hanfland, M., Mezouar, M., Prescher, C., Rüffer, R., Prakapenka, V.B., Dubrovinsky, L., 2017. Stability of iron-bearing carbonates in the deep earth's interior. Nature Communications 8. doi:10.1038/ncomms15960.

Chijioke, A.D., Nellis, W.J., Soldatov, A., Silvera, I.F., 2005. The ruby pressure standard to 150 GPa. Journal of Applied Physics 98, 114905. doi:10.1063/1.2135877.

Childs, C., O'Donnell, W., Ellison, P.B., Shelton, D.P., Salamat, A., 2020. Optical and electronic solutions for power stabilization of $CO_2$ lasers. Review of Scientific Instruments 91, 103003. doi:10.1063/5.0021156.

Chumakov, A.I., Bosak, A., Rüffer, R., 2009. Contribution of acoustic modes to the density of vibrational states measured by inelastic scattering techniques. Physical Review B 80, 094303. doi:10.1103/physrevb.80.094303.

Connolly, J., 2005. Computation of phase equilibria by linear programming: A tool for geodynamic modeling and its application to subduction zone decarbonation. Earth and Planetary Science Letters 236, 524–541. doi:10.1016/j.epsl.2005.04.033.

Dasgupta, R., Hirschmann, M.M., 2010. The deep carbon cycle and melting in Earth's interior. Earth and Planetary Science Letters 298, 1–13. doi:10.1016/j.epsl.2010.06.039.

Dasgupta, R., Hirschmann, M.M., Withers, A.C., 2004. Deep global cycling of carbon constrained by the solidus of anhydrous, carbonated eclogite under upper mantle conditions. Earth and Planetary Science Letters 227, 73–85. doi:10.1016/j.epsl.2004.08.004.

Deng, J., Du, Z., Benedetti, L.R., Lee, K.K.M., 2017. The influence of wavelength-dependent absorption and temperature gradients on temperature determination in laser-heated diamond-anvil cells. Journal of Applied Physics 121, 025901. doi:10.1063/1.4973344.

Dewaele, A., 2019. Equations of State of Simple Solids (Including Pb, NaCl and LiF) Compressed in Helium or Neon in the Mbar Range. Minerals 9, 684. doi:10.3390/min9110684.

Dewaele, A., Eggert, J.H., Loubeyre, P., Toullec, R.L., 2003. Measurement of refractive index and equation of state in dense He, $H_2$, $H_2O$ and Ne under high pressure in a diamond anvil cell. Physical Review B 67, 094112. doi:10.1103/physrevb.67.094112.

Dewaele, A., Loubeyre, P., Mezouar, M., 2004. Equations of state of six metals above 94 GPa. Physical Review B 70, 094112. doi:10.1103/physrevb.70.094112.

Dominijanni, S., 2022. Physicochemical properties of Fe-bearing minerals and metal alloys at deep Earth conditions. Ph.D. thesis. Universität Bayreuth.

Dorfman, S.M., Badro, J., Nabiei, F., Prakapenka, V.B., Cantoni, M., Gillet, P., 2018. Carbonate stability in the reduced lower mantle. Earth and Planetary Science Letters 489, 84–91. doi:10.1016/j.epsl.2018.02.035.

Dorfman, S.M., Nabiei, F., Boukaré, C.E., Prakapenka, V.B., Cantoni, M., Badro, J., Gillet, P., 2021. Composition and pressure effects on partitioning of ferrous iron in iron-rich lower mantle heterogeneities. Minerals 11, 512. doi:10.3390/min11050512.

Dorfman, S.M., Prakapenka, V.B., Meng, Y., Duffy, T.S., 2012. Intercomparison of pressure standards (au, pt, mo, MgO, NaCl and ne) to 2.5 mbar. Journal of Geophysical Research: Solid Earth 117, n/a–n/a. doi:10.1029/2012jb009292.

Drewitt, J.W., Walter, M.J., Zhang, H., McMahon, S.C., Edwards, D., Heinen, B.J., Lord, O.T., Anzellini, S., Kleppe, A.K., 2019. The fate of carbonate in oceanic crust subducted into earth's lower mantle. Earth and Planetary Science Letters 511, 213–222. doi:10.1016/j.epsl.2019.01.041.

Dubrovinskaia, N., Dubrovinsky, L., Solopova, N.A., Abakumov, A., Turner, S., Hanfland, M., Bykova, E., Bykov, M., Prescher, C., Prakapenka, V.B., Petitgirard, S., Chuvashova, I., Gasharova, B., Mathis, Y.L., Ershov, P., Snigireva, I., Snigirev, A., 2016. Terapascal static pressure generation with ultrahigh yield strength nanodiamond. Science Advances 2. doi:10.1126/sciadv.1600341.

Dubrovinsky, L., Glazyrin, K., McCammon, C., Narygina, O., Greenberg, E., Übelhack, S., Chumakov, A.I., Pascarelli, S., Prakapenka, V., Bock, J., Dubrovinskaia,

N., 2009. Portable laser-heating system for diamond anvil cells. Journal of Synchrotron Radiation 16, 737–741. doi:10.1107/s0909049509039065.

Duffy, T.S., 2005. Synchrotron facilities and the study of the Earth's deep interior. Reports on Progress in Physics 68, 1811–1859. doi:10.1088/0034-4885/68/8/r03.

Duffy, T.S., 2008. Mineralogy at the extremes. Nature 451, 269–270. doi:10.1038/nature06584.

Dziewonski, A.M., Anderson, D.L., 1981. Preliminary reference Earth model. Physics of the Earth and Planetary Interiors 25, 297–356. doi:10.1016/0031-9201(81)90046-7.

Eugster, H.P., 1957. Heterogeneous Reactions Involving Oxidation and Reduction at High Pressures and Temperatures. The Journal of Chemical Physics 26, 1760–1761. doi:10.1063/1.1743626.

Ewels, P., Sikora, T., Serin, V., Ewels, C.P., Lajaunie, L., 2016. A Complete Overhaul of the Electron Energy-Loss Spectroscopy and X-Ray Absorption Spectroscopy Database: eelsdb.eu. Microscopy and Microanalysis 22, 717–724. doi:10.1017/s1431927616000179.

Fedotenko, T., Dubrovinsky, L., Aprilis, G., Koemets, E., Snigirev, A., Snigireva, I., Barannikov, A., Ershov, P., Cova, F., Hanfland, M., Dubrovinskaia, N., 2019. Laser heating setup for diamond anvil cells for in situ synchrotron and in house high and ultra-high pressure studies. Review of Scientific Instruments 90, 104501. doi:10.1063/1.5117786.

Fei, Y., Ricolleau, A., Frank, M., Mibe, K., Shen, G., Prakapenka, V., 2007. Toward an internally consistent pressure scale. Proceedings of the National Academy of Sciences 104, 9182–9186. doi:10.1073/pnas.0609013104.

Fiquet, G., Andrault, D., Itié, J., Gillet, P., Richet, P., 1996. X-ray diffraction of periclase in a laser-heated diamond-anvil cell. Physics of the Earth and Planetary Interiors 95, 1–17. doi:10.1016/0031-9201(95)03109-x.

Fiquet, G., Auzende, A.L., Siebert, J., Corgne, A., Bureau, H., Ozawa, H., Garbarino, G., 2010. Melting of peridotite to 140 gigapascals. Science 329, 1516–1518. doi:10.1126/science.1192448.

Fiquet, G., Dewaele, A., Andrault, D., Kunz, M., Bihan, T.L., 2000. Thermoelastic properties and crystal structure of $MgSiO_3$ perovskite at lower mantle pressure and temperature conditions. Geophysical Research Letters 27, 21–24. doi:10.1029/1999gl008397.

Fiquet, G., Guyot, F., Kunz, M., Matas, J., Andrault, D., Hanfland, M., 2002. Structural refinements of magnesite at very high pressure. American Mineralogist 87, 1261–1265. doi:10.2138/am-2002-8-927.

Fischer, R.A., Campbell, A.J., Reaman, D.M., Miller, N.A., Heinz, D.L., Dera, P., Prakapenka, V.B., 2013. Phase relations in the Fe-FeSi system at high pressures and temperatures. Earth and Planetary Science Letters 373, 54–64. doi:10.1016/j.epsl.2013.04.035.

Foley, S.F., 2010. A reappraisal of redox melting in the earth's mantle as a function of tectonic setting and time. Journal of Petrology 52, 1363–1391. doi:10.1093/petrology/egq061.

Frost, B.R., 1991. Chapter 1. Introduction to oxygen fugacity and its petrolofic importance, in: Oxide Minerals. De Gruyter, pp. 1–10. doi:10.1515/9781501508684-004.

Frost, D., Poe, B., Trønnes, R., Liebske, C., Duba, A., Rubie, D., 2004. A new large-volume multianvil system. Physics of the Earth and Planetary Interiors 143-144, 507–514. doi:10.1016/j.pepi.2004.03.003.

Frost, D.J., Langenhorst, F., 2002. The effect of $Al_2O_3$ on Fe-Mg partitioning between magnesiowüstite and magnesium silicate perovskite. Earth and Planetary Science Letters 199, 227–241. doi:10.1016/s0012-821x(02)00558-7.

Frost, D.J., McCammon, C.A., 2008. The Redox State of Earth's Mantle. Annual Review of Earth and Planetary Sciences 36, 389–420. doi:10.1146/annurev.earth.36.031207.124322.

Fukao, Y., Obayashi, M., 2013. Subducted slabs stagnant above, penetrating through, and trapped below the 660 km discontinuity. Journal of Geophysical Research: Solid Earth 118, 5920–5938. doi:10.1002/2013jb010466.

Garnero, E.J., 2000. Heterogeneity of the Lowermost Mantle. Annual Review of Earth and Planetary Sciences 28, 509–537. doi:10.1146/annurev.earth.28.1.509.

Giampaoli, R., Kantor, I., Mezouar, M., Boccato, S., Rosa, A.D., Torchio, R., Garbarino, G., Mathon, O., Pascarelli, S., 2018. Measurement of temperature in the laser heated diamond anvil cell: comparison between reflective and refractive optics. High Pressure Research 38, 250–269. doi:10.1080/08957959.2018.1480017.

Goncharov, A.F., Crowhurst, J.C., 2005. Pulsed laser Raman spectroscopy in the laser-heated diamond anvil cell. Review of Scientific Instruments 76, 063905. doi:10.1063/1.1931205.

Gorman, P.J., Kerrick, D.M., Connolly, J.A.D., 2006. Modeling open system metamorphic decarbonation of subducting slabs. Geochemistry, Geophysics, Geosystems 7. doi:10.1029/2005gc001125.

Hammouda, T., 2003. High-pressure melting of carbonated eclogite and experimental constraints on carbon recycling and storage in the mantle. Earth and Planetary Science Letters 214, 357–368. doi:10.1016/s0012-821x(03)00361-3.

Hammouda, T., Keshav, S., 2015. Melting in the mantle in the presence of carbon: Review of experiments and discussion on the origin of carbonatites. Chemical Geology 418, 171–188. doi:10.1016/j.chemgeo.2015.05.018.

Hanfland, M., Syassen, K., Fahy, S., Louie, S.G., Cohen, M.L., 1986. The first-order raman mode of diamond under pressure. Physica B 139-140, 516–519. doi:10.1016/0378-4363(86)90636-4.

Haselton, H.T., Sharp, W.E., Newton, R.C., 1978. $CO_2$ fugacity at high temperatures and pressures from experimental decarbonation reactions. Geophysical Research Letters 5, 753–756. doi:10.1029/gl005i009p00753.

Hennet, L., Thiaudière, D., Gailhanou, M., Landron, C., Coutures, J.P., Price, D.L., 2002. Fast x-ray scattering measurements on molten alumina using a 120° curved position sensitive detector. Review of Scientific Instruments 73, 124–129. doi:10.1063/1.1426228.

Hirose, K., Sinmyo, R., Hernlund, J., 2017. Perovskite in Earth's deep interior. Science 358, 734–738. doi:10.1126/science.aam8561.

Hirose, K., Sinmyo, R., Sata, N., Ohishi, Y., 2006. Determination of post-perovskite phase transition boundary in $MgSiO_3$ using Au and MgO pressure standards. Geophysical Research Letters 33. doi:10.1029/2005gl024468.

Hirose, K., Takafuji, N., Sata, N., Ohishi, Y., 2005. Phase transition and density of subducted MORB crust in the lower mantle. Earth and Planetary Science Letters 237, 239–251. doi:10.1016/j.epsl.2005.06.035.

Holmes, N.C., Moriarty, J.A., Gathers, G.R., Nellis, W.J., 1989. The equation of state of platinum to 660 GPa (6.6 mbar). Journal of Applied Physics 66, 2962–2967. doi:10.1063/1.344177.

Howard, J.E., 1979. Imaging properties of off-axis parabolic mirrors. Applied Optics 18, 2714. doi:10.1364/ao.18.002714.

Immoor, J., Miyagi, L., Liermann, H.P., Speziale, S., Schulze, K., Buchen, J., Kurnosov, A., Marquardt, H., 2022. Weak cubic $CaSiO_3$ perovskite in the Earth's mantle. Nature 603, 276–279. doi:10.1038/s41586-021-04378-2.

Irifune, T., Ringwood, A., 1993. Phase transformations in subducted oceanic crust and buoyancy relationships at depths of 600–800 km in the mantle. Earth and Planetary Science Letters 117, 101–110. doi:10.1016/0012-821x(93)90120-x.

Irifune, T., Shinmei, T., McCammon, C.A., Miyajima, N., Rubie, D.C., Frost, D.J., 2010. Iron Partitioning and Density Changes of Pyrolite in Earth's Lower Mantle. Science 327, 193–195. doi:10.1126/science.1181443.

Irifune, T., Tsuchiya, T., 2007. Mineralogy of the Earth – Phase Transitions and Mineralogy of the Lower Mantle, in: Treatise on Geophysics. Elsevier, pp. 33–62. doi:10.1016/b978-044452748-6.00030-4.

Ishii, T., Shi, L., Huang, R., Tsujino, N., Druzhbin, D., Myhill, R., Li, Y., Wang, L., Yamamoto, T., Miyajima, N., et al., 2016. Generation of pressures over 40 gpa using kawai-type multi-anvil press with tungsten carbide anvils. Review of Scientific Instruments 87, 024501.

Ishii, T., Yamazaki, D., Tsujino, N., Xu, F., Liu, Z., Kawazoe, T., Yamamoto, T., Druzhbin, D., Wang, L., Higo, Y., Tange, Y., Yoshino, T., Katsura, T., 2017. Pressure generation to 65 GPa in a kawai-type multi-anvil apparatus with tungsten carbide anvils. High Pressure Research 37, 507–515. doi:10.1080/08957959.2017.1375491.

Isshiki, M., Irifune, T., Hirose, K., Ono, S., Ohishi, Y., Watanuki, T., Nishibori, E., Takata, M., Sakata, M., 2004. Stability of magnesite and its high-pressure form in the lowermost mantle. Nature 427, 60–63. doi:10.1038/nature02181.

Jeanloz, R., Kavner, A., 1996. Melting criteria and imaging spectroradiometry in laser-heated diamond-cell experiments. Philosophical Transactions of the Royal Society of London. Series A: Mathematical, Physical and Engineering Sciences 354, 1279–1305. doi:10.1098/rsta.1996.0049.

Jennings, E.S., 2020. Using complementary microanalytical techniques to analyse diamond anvil cell experiments. IOP Conference Series: Materials Science and Engineering 891, 012015. doi:10.1088/1757-899x/891/1/012015.

Johannes, W., 1969. An experimental investigation of the system MgO-$SiO_2$ -$H_2O$-$CO_2$. American Journal of Science 267, 1083–1104. doi:10.2475/ajs.267.9.1083.

Kakizawa, S., Inoue, T., Suenami, H., Kikegawa, T., 2015. Decarbonation and melting in $MgCO_3$-$SiO_2$ system at high temperature and high pressure. Journal of Mineralogical and Petrological Sciences 110, 179–188. doi:10.2465/jmps.150124.

Kaminsky, F., 2012. Mineralogy of the lower mantle: A review of 'super-deep' mineral inclusions in diamond. Earth-Science Reviews 110, 127–147. doi:10.1016/j.earscirev.2011.10.005.

Kaminsky, F.V., 2017. The Earth's Lower Mantle. Springer International Publishing. doi:10.1007/978-3-319-55684-0.

Kaminsky, F.V., Ryabchikov, I.D., Wirth, R., 2015. A primary natrocarbonatitic association in the deep earth. Mineralogy and Petrology 110, 387–398. doi:10.1007/s00710-015-0368-4.

Kaminsky, F.V., Wirth, R., 2011. Iron carbide inclusions in lower-mantle diamond from Juina, Brazil IRON. The Canadian Mineralogist 49, 555–572. doi:10.3749/canmin.49.2.555.

Kantor, I., Marini, C., Mathon, O., Pascarelli, S., 2018. A laser heating facility for energy-dispersive x-ray absorption spectroscopy. Review of Scientific Instruments 89, 013111. doi:10.1063/1.5010345.

Kantor, I., Prakapenka, V., Kantor, A., Dera, P., Kurnosov, A., Sinogeikin, S., Dubrovinskaia, N., Dubrovinsky, L., 2012. BX90: A new diamond anvil cell design for x-ray diffraction and optical measurements. Review of Scientific Instruments 83, 125102. doi:10.1063/1.4768541.

Katsura, T., Ito, E., 1990. Melting and subsolidus phase relations in the $MgSiO_3$-$MgCO_3$ system at high pressures: implications to evolution of the Earth's atmosphere. Earth and Planetary Science Letters 99, 110–117. doi:10.1016/0012-821x(90)90074-8.

Katsura, T., Yoneda, A., Yamazaki, D., Yoshino, T., Ito, E., 2010. Adiabatic temperature profile in the mantle. Physics of the Earth and Planetary Interiors 183, 212–218. doi:10.1016/j.pepi.2010.07.001.

Kawai, N., Endo, S., 1970. The generation of ultrahigh hydrostatic pressures by a split sphere apparatus. Review of Scientific Instruments 41, 1178–1181. doi:10.1063/1.1684753.

Kelemen, P.B., Manning, C.E., 2015. Reevaluating carbon fluxes in subduction zones, what goes down, mostly comes up. Proceedings of the National Academy of Sciences 112. doi:10.1073/pnas.1507889112.

Kennett, B.L.N., Engdahl, E.R., 1991. Traveltimes for global earthquake location and phase identification. Geophysical Journal International 105, 429–465. doi:10.1111/j.1365-246x.1991.tb06724.x.

Kennett, B.L.N., Engdahl, E.R., Buland, R., 1995. Constraints on seismic velocities in the Earth from traveltimes. Geophysical Journal International 122, 108–124. doi:10.1111/j.1365-246x.1995.tb03540.x.

Keppler, H., Frost, D.J., 2006. Introduction to minerals under extreme conditions, in: Mineral behaviour at extreme conditions. Mineralogical society of Great Britain and Ireland, pp. 1–30. doi:10.1180/emu-notes.7.1.

Kerrick, D., Connolly, J., 2001. Metamorphic devolatilization of subducted oceanic metabasalts: implications for seismicity, arc magmatism and volatile recycling. Earth and Planetary Science Letters 189, 19–29. doi:10.1016/s0012-821x(01)00347-8.

Keshav, S., Gudfinnsson, G.H., 2010. Experimentally dictated stability of carbonated oceanic crust to moderately great depths in the Earth: Results from the solidus determination in the system CaO-MgO-$Al_3O_3$-$SiO_2$-$CO_2$. Journal of Geophysical Research 115. doi:10.1029/2009jb006457.

Kesson, S.E., Gerald, J.D.F., Shelley, J.M., 1998. Mineralogy and dynamics of a pyrolite lower mantle. Nature 393, 252–255. doi:10.1038/30466.

Kiseeva, E.S., Litasov, K.D., Yaxley, G.M., Ohtani, E., Kamenetsky, V.S., 2013. Melting and phase relations of carbonated eclogite at 9-21 GPa and the petrogenesis of alkali-rich melts in the deep mantle. Journal of Petrology 54, 1555–1583. doi:10.1093/petrology/egt023.

Konôpková, Z., Morgenroth, W., Husband, R., Giordano, N., Pakhomova, A., Gutowski, O., Wendt, M., Glazyrin, K., Ehnes, A., Delitz, J.T., Goncharov, A.F., Prakapenka, V.B., Liermann, H.P., 2021. Laser heating system at the Extreme Conditions Beamline, P02.2, PETRA III. Journal of Synchrotron Radiation 28, 1747–1757. doi:10.1107/s1600577521009231.

Koziol, A.M., Newton, R.C., 1995. Experimental determination of the reactions magnesite + quartz = enstatite + $CO_2$ and magnesite = periclase + $CO_2$, and enthalpies of formation of enstatite and magnesite. American Mineralogist 80, 1252–1260.

Kumar, P.S., Pavithra, K.G., Naushad, M., 2019. Characterization techniques for nanomaterials, in: Nanomaterials for Solar Cell Applications. Elsevier, pp. 97–124. doi:10.1016/b978-0-12-813337-8.00004-7.

Kupenko, I., Dubrovinsky, L., Dubrovinskaia, N., McCammon, C., Glazyrin, K., Bykova, E., Ballaran, T.B., Sinmyo, R., Chumakov, A.I., Potapkin, V., Kantor, A., Rüffer, R., Hanfland, M., Crichton, W., Merlini, M., 2012. Portable double-sided laser-heating system for mössbauer spectroscopy and x-ray diffraction experiments at synchrotron facilities with diamond anvil cells. Review of Scientific Instruments 83, 124501. doi:10.1063/1.4772458.

Kupenko, I., Kolesnikov, E., Mülle, S.C., Aprilis, G., Chumakov, A.I., Sergeev, I., LéliaLibon, Morgenroth, W., Rohrbach, A., Wilke, M., Sanchez-Valle, C., 2022. Carbon in the core: sound velocities of the $Fe_7C_3$ carbide at extreme conditions [abstract]. IMA2022-1615.

Kupenko, I., Strohm, C., McCammon, C., Cerantola, V., Glazyrin, K., Petitgirard, S., Vasiukov, D., Aprilis, G., Chumakov, A.I., Rüffer, R., Dubrovinsky, L., 2015. Time differentiated nuclear resonance spectroscopy coupled with pulsed laser heating in diamond anvil cells. Review of Scientific Instruments 86, 114501. doi:10.1063/1.4935304.

Kurnosov, A., Marquardt, H., Dubrovinsky, L., Potapkin, V., 2019. A waveguide-based flexible $CO_2$-laser heating system for diamond-anvil cell applications. Comptes Rendus Geoscience 351, 280–285. doi:10.1016/j.crte.2018.09.008.

Kushiro, I., 1975. Carbonate-silicate reactions at high presures and possible presence of dolomite and magnesite in the upper mantle. Earth and Planetary Science Letters 28, 116–120. doi:10.1016/0012-821x(75)90218-6.

Lajaunie, L., Pardanaud, C., Martin, C., Puech, P., Hu, C., Biggs, M., Arenal, R., 2017. Advanced spectroscopic analyses on a: C-H materials: Revisiting the EELS characterization and its coupling with multi-wavelength Raman spectroscopy. Carbon 112, 149–161. doi:10.1016/j.carbon.2016.10.092.

Laskin, A., 2021. Basics of Optics on Imaging Quality and Aberrations, in: Handbook of Laser Micro- and Nano-Engineering. Springer International Publishing, pp. 1–54. doi:10.1007/978-3-319-69537-2_62-2.

Laskin, A., Laskin, V., 2011. $\pi$shaper – refractive beam shaping optics for advanced laser technologies. Journal of Physics: Conference Series 276, 012171. doi:10.1088/1742-6596/276/1/012171.

Li, F., Cui, Q., He, Z., Cui, T., Gao, C., Zhou, Q., Zou, G., 2006. Brillouin scattering spectroscopy for a laser heated diamond anvil cell. Applied Physics Letters 88, 203507. doi:10.1063/1.2205164.

Liermann, H.P., Konôpková, Z., Morgenroth, W., Glazyrin, K., Bednarčik, J., McBride, E.E., Petitgirard, S., Delitz, J.T., Wendt, M., Bican, Y., Ehnes, A., Schwark, I., Rothkirch, A., Tischer, M., Heuer, J., Schulte-Schrepping, H., Kracht, T., Franz, H., 2015. The Extreme Conditions Beamline P02.2 and the Extreme Conditions Science Infrastructure at PETRA III. Journal of Synchrotron Radiation 22, 908–924. doi:10.1107/s1600577515005937.

Lin, J.F., Santoro, M., Struzhkin, V.V., kwang Mao, H., Hemley, R.J., 2004. In situ high pressure-temperature Raman spectroscopy technique with laser-heated diamond anvil cells. Review of Scientific Instruments 75, 3302–3306. doi:10.1063/1.1791811.

Lin, J.F., Struzhkin, V.V., Jacobsen, S.D., Hu, M.Y., Chow, P., Kung, J., Liu, H., kwang Mao, H., Hemley, R.J., 2005. Spin transition of iron in magnesiowüstite in the Earth's lower mantle. Nature 436, 377–380. doi:10.1038/nature03825.

Lin, J.F., Vankó, G., Jacobsen, S.D., Iota, V., Struzhkin, V.V., Prakapenka, V.B., Kuznetsov, A., Yoo, C.S., 2007. Spin Transition Zone in Earth's Lower Mantle. Science 317, 1740–1743. doi:10.1126/science.1144997.

Litasov, K.D., Fei, Y., Ohtani, E., Kuribayashi, T., Funakoshi, K., 2008. Thermal equation of state of magnesite to 32gpa and 2073k. Physics of the Earth and Planetary Interiors 168, 191–203. doi:10.1016/j.pepi.2008.06.018.

Litasov, K.D., Shatskiy, A., 2018. Carbon-bearing magmas in the earth's deep interior, in: Magmas Under Pressure. Elsevier, pp. 43–82. doi:10.1016/b978-0-12-811301-1.00002-2.

Litasov, K.D., Shatskiy, A., Ohtani, E., Yaxley, G.M., 2013. Solidus of alkaline carbonatite in the deep mantle. Geology 41, 79–82. doi:10.1130/g33488.1.

Litasov, K.D., Shatskiy, A.F., 2019. $MgCO_3$ + $SiO_2$ Reaction at Pressures up to 32 GPa Studied Using in-Situ X-Ray Diffraction and Synchrotron Radiation. Geochemistry International 57, 1024–1033. doi:10.1134/s0016702919090064.

Liu, H., Shu, D., Sun, F., Li, Q., Chen, T., Xing, B., Chen, D., Qing, C., 2018. Effect of manganese substitution on the crystal structure and decomposition kinetics of siderite. Journal of Thermal Analysis and Calorimetry 136, 1315–1322. doi:10.1007/s10973-018-7767-9.

Liu, L.g., 1974. Silicate perovskite from phase transformations of pyrope-garnet at high pressure and temperature. Geophysical Research Letters 1, 277–280. doi:10.1029/gl001i006p00277.

Liu, X., Lu, Z., Wang, X., Jiang, Z., Li, Y., 2011. Study on the focusing characteristics of off-axis parabolic mirror focusing system, in: 2011 Academic International Symposium on Optoelectronics and Microelectronics Technology, IEEE. pp. 116–119. doi:10.1109/aismot.2011.6159331.

Liu, Z., Ishii, T., Katsura, T., 2017. Rapid decrease of $MgAlO_{2.5}$ component in bridgmanite with pressure. Geochemical Perspectives Letters , 12–18doi:10.7185/geochemlet.1739.

Lord, O., Walter, M., Dasgupta, R., Walker, D., Clark, S., 2009. Melting in the Fe-C system to 70 GPa. Earth and Planetary Science Letters 284, 157–167. doi:10.1016/j.epsl.2009.04.017.

Lord, O.T., Walter, M.J., Dobson, D.P., Armstrong, L., Clark, S.M., Kleppe, A., 2010. The FeSi phase diagram to 150 GPa. Journal of Geophysical Research 115. doi:10.1029/2009jb006528.

Luth, R.W., 2001. Experimental determination of the reaction aragonite + magnesite = dolomite at 5 to 9 GPa. Contributions to Mineralogy and Petrology 141, 222–232. doi:10.1007/s004100100238.

Luth, R.W., Palyanov, Y.N., Bureau, H., 2022. Experimental petrology applied to natural diamond growth. Reviews in Mineralogy and Geochemistry 88, 755–808. doi:10.2138/rmg.2022.88.14.

Maeda, F., Ohtani, E., Kamada, S., Sakamaki, T., Hirao, N., Ohishi, Y., 2017. Diamond formation in the deep lower mantle: a high-pressure reaction of $MgCO_3$ and $SiO_2$. Scientific Reports 7. doi:10.1038/srep40602.

Malone, R.M., Becker, S.A., Dolan, D.H., Hacking, R.G., Hickman, R.J., Kaufman, M.I., Stevens, G.D., Turley, W.D., 2006. Design of a thermal imaging diagnostic using 90-degree off-axis parabolic mirrors, in: Mouroulis, P.Z., Smith, W.J., Johnson, R.B. (Eds.), SPIE Proceedings, SPIE. pp. 315–323. doi:10.1117/12.681080.

Mao, H., Bell, P., 1977. Technique of operating the diamond-window pressure cell: Considerations of the design and functions of the diamond anvils. Year Book–Carnegie Inst. Washington 76, 646–650.

Mao, H.K., Wu, Y., Chen, L.C., Shu, J.F., Jephcoat, A.P., 1990. Static compression of iron to 300 GPa and $Fe_{0.8}Ni_{0.2}$ alloy to 260 GPa: Implications for composition of the core. Journal of Geophysical Research 95, 21737. doi:10.1029/jb095ib13p21737.

Mao, H.K., Xu, J., Bell, P.M., 1986. Calibration of the ruby pressure gauge to 800 kbar under quasi-hydrostatic conditions. Journal of Geophysical Research 91, 4673. doi:10.1029/jb091ib05p04673.

Mao, W.L., Boulard, E., 2013. Nanoprobes for deep carbon. Reviews in Mineralogy and Geochemistry 75, 423–448. doi:10.2138/rmg.2013.75.13.

Marquardt, H., Marquardt, K., 2012. Focused ion beam preparation and characterization of single-crystal samples for high-pressure experiments in the diamond-anvil cell. American Mineralogist 97, 299–304. doi:10.2138/am.2012.3911.

Marquardt, H., Miyagi, L., 2015. Slab stagnation in the shallow lower mantle linked to an increase in mantle viscosity. Nature Geoscience 8, 311–314. doi:10.1038/ngeo2393.

Martirosyan, N., Shatskiy, A., Chanyshev, A., Litasov, K., Podborodnikov, I., Yoshino, T., 2019. Effect of water on the magnesite–iron interaction, with implications for the fate of carbonates in the deep mantle. Lithos 326-327, 435–445. doi:10.1016/j.lithos.2019.01.004.

Martirosyan, N., Shatskiy, A., Litasov, K., Sharygin, I., Yoshino, T., 2022. Interaction of carbonates with peridotite containing iron metal: Implications for carbon speciation in the upper mantle. Lithos 428-429, 106817. doi:10.1016/j.lithos.2022.106817.

Mashino, I., Murakami, M., Miyajima, N., Petitgirard, S., 2020. Experimental evidence for silica-enriched Earth's lower mantle with ferrous iron dominant bridgmanite. Proceedings of the National Academy of Sciences 117, 27899–27905. doi:10.1073/pnas.1917096117.

McCammon, C., Bureau, H., Cleaves, J.H., Cottrell, E., Dorfman, S.M., Kellogg, L.H., Li, J., Mikhail, S., Moussallam, Y., Sanloup, C., Thomson, A.R., Brovarone, A.V., 2020. Deep earth carbon reactions through time and space. American Mineralogist 105, 22–27. doi:10.2138/am-2020-6888ccby.

McDonough, W., s. Sun, S., 1995. The composition of the Earth. Chemical Geology 120, 223–253. doi:10.1016/0009-2541(94)00140-4.

Meier, T., Dwivedi, A.P., Khandarkhaeva, S., Fedotenko, T., Dubrovinskaia, N., Dubrovinsky, L., 2019. Table-top nuclear magnetic resonance system for high-pressure studies with in situ laser heating. Review of Scientific Instruments 90, 123901. doi:10.1063/1.5128592.

Meng, Y., Hrubiak, R., Rod, E., Boehler, R., Shen, G., 2015. New developments in laser-heated diamond anvil cell with in situ synchrotron x-ray diffraction at High Pressure Collaborative Access Team. Review of Scientific Instruments 86, 072201. doi:10.1063/1.4926895.

Mergner, V., Kupenko, I., Spiekermann, G., Petitgirard, S., Libon, L., Chariton, S., Krug, M., Steinbrügge, R., Sergueev, I., Sanchez-Valle, C., 2021. Sound velocities in FeSi at lower mantle conditions and the origin of ultralow-velocity zones. Geophysical Research Letters 48. doi:10.1029/2020gl092257.

Merrill, L., Bassett, W.A., 1974. Miniature diamond anvil pressure cell for single crystal x-ray diffraction studies. Review of Scientific Instruments 45, 290–294. doi:10.1063/1.1686607.

Mezouar, M., Giampaoli, R., Garbarino, G., Kantor, I., Dewaele, A., Weck, G., Boccato, S., Svitlyk, V., Rosa, A.D., Torchio, R., Mathon, O., Hignette, O., Bauchau, S., 2017. Methodology for in situ synchrotron X-ray studies in the laser-heated diamond anvil cell. High Pressure Research 37, 170–180. doi:10.1080/08957959.2017.1306626.

Ming, L.C., Bassett, W.A., 1974. Laser heating in the diamond anvil press up to 2000°C sustained and 3000°C pulsed at pressures up to 260 kilobars. Review of Scientific Instruments 45, 1115–1118. doi:10.1063/1.1686822.

Miyahara, M., Sakai, T., Ohtani, E., Kobayashi, Y., Kamada, S., Kondo, T., E, T.N., Yoo, J.H., Nishijima, M., Vashaei, Z., 2008. Application of FIB system to ultrahigh-pressure Earth science. Journal of Mineralogical and Petrological Sciences 103, 88–93. doi:10.2465/jmps.070612b.

Molina, J., 2000. Carbonate stability and fluid composition in subducted oceanic crust: an experimental study on $H_2O$-$CO_2$-bearing basalts. Earth and Planetary Science Letters 176, 295–310.

Morelli, A., Dziewonski, A.M., 1993. Body Wave Traveltimes and A Spherically Symmetric P- and S-Wave Velocity Model. Geophysical Journal International 112, 178–194. doi:10.1111/j.1365-246x.1993.tb01448.x.

Morlidge, M., Pawley, A., Droop, G., 2006. Double carbonate breakdown reactions at high pressures: an experimental study in the system CaO-MgO-FeO-MnO-$CO_2$. Contributions to Mineralogy and Petrology 152, 365–373. doi:10.1007/s00410-006-0112-5.

Murakami, M., Asahara, Y., Ohishi, Y., Hirao, N., Hirose, K., 2009. Development of in situ Brillouin spectroscopy at high pressure and high temperature with synchrotron radiation and infrared laser heating system: Application to the Earth's deep interior. Physics of the Earth and Planetary Interiors 174, 282–291. doi:10.1016/j.pepi.2008.07.030.

Murakami, M., Hirose, K., Kawamura, K., Sata, N., Ohishi, Y., 2004. Post-Perovskite Phase Transition in $MgSiO_3$. Science 304, 855–858. doi:10.1126/science.1095932.

Murakami, M., Ohishi, Y., Hirao, N., Hirose, K., 2012. A perovskitic lower mantle inferred from high-pressure, high-temperature sound velocity data. Nature 485, 90–94. doi:10.1038/nature11004.

Murphy, C.A., Jackson, J.M., Sturhahn, W., 2013. Experimental constraints on the thermodynamics and sound velocities of hcp-Fe to core pressures. Journal of Geophysical Research: Solid Earth 118, 1999–2016. doi:10.1002/jgrb.50166.

Müller, S.C., Kolesnikov, E., Aprilis, G., Chumakov, A., Comboni, D., Hanfland, M., Sergeev, I., Libon, L., Morgenroth, W., Wilke, M., Li, X., Koppetz-Mitra, H., Rohrbach, A., Berndt, J., Sanchez-Valle, C., Kupenko, I., 2022. Silicon and carbon content in the earth's inner core constrained from sound velocities [abstract]. IMA2022-1468.

Navrotsky, A., 1999. A Lesson from Ceramics. Science 284, 1788–1789. doi:10.1126/science.284.5421.1788.

Oganov, A.R., Ono, S., 2004. Theoretical and experimental evidence for a post-perovskite phase of $MgSiO_3$ in Earth's D" layer. Nature 430, 445–448. doi:10.1038/nature02701.

O'neill, H.S.C., Wall, V., 1987. The Olivine—Orthopyroxene—Spinel oxygen geobarometer, the nickel precipitation curve, and the oxygen fugacity of the Earth's Upper Mantle. Journal of Petrology 28, 1169–1191. doi:10.1093/petrology/28.6.1169.

Ono, S., Hirose, K., Murakami, M., Isshiki, M., 2002. Post-stishovite phase boundary in SiO2 determined by in situ x-ray observations. Earth and Planetary Science Letters 197, 187–192. doi:10.1016/s0012-821x(02)00479-x.

Ono, S., Ito, E., Katsura, T., 2001. Mineralogy of subducted basaltic crust (MORB) from 25 to 37 GPa, and chemical heterogeneity of the lower mantle. Earth and Planetary Science Letters 190, 57–63. doi:10.1016/s0012-821x(01)00375-2.

Ono, S., Kikegawa, T., Ohishi, Y., 2006. Structural property of CsCl-type sodium chloride under pressure. Solid State Communications 137, 517–521. doi:10.1016/j.ssc.2006.01.022.

Petitgirard, S., Borchert, M., Andrault, D., Appel, K., Mezouar, M., Liermann, H.P., 2012. An in situ approach to study trace element partitioning in the laser heated diamond anvil cell. Review of Scientific Instruments 83, 013904. doi:10.1063/1.3680573.

Petitgirard, S., Salamat, A., Beck, P., Weck, G., Bouvier, P., 2013. Strategies for in situ laser heating in the diamond anvil cell at an X-ray diffraction beamline. Journal of Synchrotron Radiation 21, 89–96. doi:10.1107/s1600577513027434.

Piermarini, G.J., Block, S., Barnett, J.D., Forman, R.A., 1975. Calibration of the pressure dependence of the R1 ruby fluorescence line to 195 kbar. Journal of Applied Physics 46, 2774–2780. doi:10.1063/1.321957.

Plank, T., Manning, C.E., 2019. Subducting carbon. Nature 574, 343–352. doi:10.1038/s41586-019-1643-z.

Prakapenka, V.B., Kubo, A., Kuznetsov, A., Laskin, A., Shkurikhin, O., Dera, P., Rivers, M.L., Sutton, S.R., 2008. Advanced flat top laser heating system for high pressure research at GSECARS: application to the melting behavior of germanium. High Pressure Research 28, 225–235. doi:10.1080/08957950802050718.

Prescher, C., Prakapenka, V.B., 2015. Dioptas: a program for reduction of two-dimensional x-ray diffraction data and data exploration. High Pressure Research 35, 223–230. doi:10.1080/08957959.2015.1059835.

Reed, S.J.B., 2005. Electron Microprobe Analysis and Scanning Electron Microscopy in Geology. Cambridge University Press. doi:10.1017/cbo9780511610561.

Regier, M.E., Pearson, D.G., Stachel, T., Luth, R.W., Stern, R.A., Harris, J.W., 2020. The lithospheric-to-lower-mantle carbon cycle recorded in superdeep diamonds. Nature 585, 234–238. doi:10.1038/s41586-020-2676-z.

Richet, P., Leclerc, F., Benoist, L., 1993. Melting of forsterite and spinel, with implications for the glass transition of mg2sio4 liquid. Geophysical Research Letters 20, 1675–1678. doi:10.1029/93gl01836.

Richmond, N.C., Brodholt, J.P., 1998. Calculated role of aluminum in the incorporation of ferric iron into magnesium silicate perovskite. American Mineralogist 83, 947–951. doi:10.2138/am-1998-9-1003.

Ricolleau, A., Fei, Y., Cottrell, E., Watson, H., Deng, L., Zhang, L., Fiquet, G., Auzende, A.L., Roskosz, M., Morard, G., Prakapenka, V., 2009. Density profile of pyrolite under the lower mantle conditions. Geophysical Research Letters 36. doi:10.1029/2008gl036759.

Ringwood, A., 1991. Phase transformations and their bearing on the constitution and dynamics of the mantle. Geochimica et Cosmochimica Acta 55, 2083–2110. doi:10.1016/0016-7037(91)90090-r.

Rohrbach, A., Ballhaus, C., Golla–Schindler, U., Ulmer, P., Kamenetsky, V.S., Kuzmin, D.V., 2007. Metal saturation in the upper mantle. Nature 449, 456–458. doi:10.1038/nature06183.

Rohrbach, A., Schmidt, M.W., 2011. Redox freezing and melting in the Earth's deep mantle resulting from carbon-iron redox coupling. Nature 472, 209–212. doi:10.1038/nature09899.

Rubie, D.C., 1999. Characterising the sample environment in multianvil high-pressure experiments. Phase Transitions 68, 431–451. doi:10.1080/01411599908224526.

Rubie, D.C., Frost, D.J., Mann, U., Asahara, Y., Nimmo, F., Tsuno, K., Kegler, P., Holzheid, A., Palme, H., 2011. Heterogeneous accretion, composition and core–mantle differentiation of the Earth. Earth and Planetary Science Letters 301, 31–42. doi:10.1016/j.epsl.2010.11.030.

Rueff, J.P., Mezouar, M., Acet, M., 2008. Short-range magnetic collapse of Fe under high pressure at high temperatures observed using x-ray emission spectroscopy. Physical Review B 78, 100405. doi:10.1103/physrevb.78.100405.

Sakai, T., Ohtani, E., Hirao, N., Ohishi, Y., 2011. Equation of state of the NaCl-b2 phase up to 304 GPa. Journal of Applied Physics 109, 084912. doi:10.1063/1.3573393.

Sakamaki, T., Ohtani, E., Fukui, H., Kamada, S., Takahashi, S., Sakairi, T., Takahata, A., Sakai, T., Tsutsui, S., Ishikawa, D., Shiraishi, R., Seto, Y., Tsuchiya, T., Baron, A.Q.R., 2016. Constraints on Earth's inner core composition inferred from measurements of the sound velocity of hcp-iron in extreme conditions. Science Advances 2. doi:10.1126/sciadv.1500802.

Salamat, A., Fischer, R.A., Briggs, R., McMahon, M.I., Petitgirard, S., 2014. In situ synchrotron X-ray diffraction in the laser-heated diamond anvil cell: Melting phenomena and synthesis of new materials. Coordination Chemistry Reviews 277-278, 15–30. doi:10.1016/j.ccr.2014.01.034.

Sato, K., Katsura, T., 2001. Experimental investigation on dolomite dissociation into aragonite + magnesite up to 8.5 GPa. Earth and Planetary Science Letters 184, 529–534. doi:10.1016/s0012-821x(00)00346-0.

Serin, V., Beche, E., Berjoan, R., Abidate, O., Dorignac, D., Rats, D., Fontaine, J., L.Vandenbulcke, Germain, C., Catherinot, A., 1997. XAES, XPS, EELS and Raman spectroscopy of polycrystalline to amorphous carbon films with various sp 3 to sp 2 bondings. Diamond Materials V.

Seto, Y., Hamane, D., Nagai, T., Fujino, K., 2008. Fate of carbonates within oceanic plates subducted to the lower mantle, and a possible mechanism of diamond formation. Physics and Chemistry of Minerals 35, 223–229. doi:10.1007/s00269-008-0215-9.

Shatskiy, A., Arefiev, A.V., Litasov, K.D., 2023. Change in carbonate budget and composition during subduction below metal saturation boundary. Geoscience Frontiers 14, 101463. doi:10.1016/j.gsf.2022.101463.

Shcheka, S.S., Wiedenbeck, M., Frost, D.J., Keppler, H., 2006. Carbon solubility in mantle minerals. Earth and Planetary Science Letters 245, 730–742. doi:10.1016/j.epsl.2006.03.036.

Shen, G., Mao, H.K., 2016. High-pressure studies with x-rays using diamond anvil cells. Reports on Progress in Physics 80, 016101. doi:10.1088/1361-6633/80/1/016101.

Shen, G., Rivers, M.L., Wang, Y., Sutton, S.R., 2001. Laser heated diamond cell system at the Advanced Photon Source for in situ x-ray measurements at high pressure and temperature. Review of Scientific Instruments 72, 1273. doi:10.1063/1.1343867.

Shen, G., Wang, L., Ferry, R., kwang Mao, H., Hemley, R.J., 2010. A portable laser heating microscope for high pressure research. Journal of Physics: Conference Series 215, 012191. doi:10.1088/1742-6596/215/1/012191.

Shim, S.H., 2008. The postperovskite transition. Annual Review of Earth and Planetary Sciences 36, 569–599. doi:10.1146/annurev.earth.36.031207.124309.

Smith, D., Smith, J.S., Childs, C., Rod, E., Hrubiak, R., Shen, G., Salamat, A., 2018. A $CO_2$ laser heating system for in situ high pressure-temperature experiments at HPCAT. Review of Scientific Instruments 89, 083901. doi:10.1063/1.5040508.

Smith, E.M., Shirey, S.B., Nestola, F., Bullock, E.S., Wang, J., Richardson, S.H., Wang, W., 2016. Large gem diamonds from metallic liquid in Earth's deep mantle. Science 354, 1403–1405. doi:10.1126/science.aal1303.

Solopova, N.A., Dubrovinsky, L., Spivak, A.V., Litvin, Y.A., Dubrovinskaia, N., 2015. Melting and decomposition of $MgCO_3$ at pressures up to 84 GPa. Physics and Chemistry of Minerals 42, 73–81. doi:10.1007/s00269-014-0701-1.

Spiekermann, G., Harder, M., Gilmore, K., Zalden, P., Sahle, C., Petitgirard, S., Wilke, M., Biedermann, N., Weis, C., Morgenroth, W., Tse, J., Kulik, E., Nishiyama, N., Yavaş, H., Sternemann, C., 2019. Persistent Octahedral Coordination in Amorphous $GeO_2$ Up to 100 GPa by K$\beta$" X-Ray Emission Spectroscopy. Physical Review X 9, 011025. doi:10.1103/physrevx.9.011025.

Spiekermann, G., Kupenko, I., Petitgirard, S., Harder, M., Nyrow, A., Weis, C., Albers, C., Biedermann, N., Libon, L., Sahle, C.J., Cerantola, V., Glazyrin, K., Konôpková, Z., Sinmyo, R., Morgenroth, W., Sergueev, I., Yavaş, H., Dubrovinsky, L., Tolan, M., Sternemann, C., Wilke, M., 2020. A portable on-axis laser-heating system for near-90° x-ray spectroscopy: application to ferropericlase and iron silicide. Journal of Synchrotron Radiation 27, 414–424. doi:10.1107/s1600577519017041.

Spiekermann, G., Libon, L., Albers, C., Sakrowski, R., Petitgirard, S., Sahle, C.J., Sundermann, M., Gretarsson, H., Sergueev, I., Sternemann, C., Wilke, M., Murakami, M., 2021. Reflective imaging, on-axis laser heating and radiospectrometry of samples in diamond anvil cells with a parabolic mirror. High Pressure Research 41, 142–154. doi:10.1080/08957959.2021.1921173.

Stachel, T., Harris, J.W., Brey, G.P., Joswig, W., 2000. Kankan diamonds (guinea) II: lower mantle inclusion parageneses. Contributions to Mineralogy and Petrology 140, 16–27. doi:10.1007/s004100000174.

Stagno, V., 2019. Carbon, carbides, carbonates and carbonatitic melts in the earth's interior. Journal of the Geological Society 176, 375–387. doi:10.1144/jgs2018-095.

Stagno, V., Cerantola, V., Aulbach, S., Lobanov, S., McCammon, C.A., Merlini, M., 2019. Carbon-bearing phases throughout Earth's interior, in: Orcutt, B.N., Daniel, I., Dasgupta, R. (Eds.), Deep carbon: Past to present. Cambridge University Press. chapter Chapter4, pp. 129–162.

Stagno, V., Tange, Y., Miyajima, N., McCammon, C.A., Irifune, T., Frost, D.J., 2011. The stability of magnesite in the transition zone and the lower mantle as function of oxygen fugacity. Geophysical Research Letters 38, n/a–n/a. doi:10.1029/2011gl049560.

Stan, C., Beavers, C., Kunz, M., Tamura, N., 2018. X-Ray Diffraction under Extreme Conditions at the Advanced Light Source. Quantum Beam Science 2, 4. doi:10.3390/qubs2010004.

Sternemann, C., Wilke, M., 2016. Spectroscopy of low and intermediate Z elements at extreme conditions: in situ studies of Earth materials at pressure and temperature via X-ray Raman scattering. High Pressure Research 36, 275–292. doi:10.1080/08957959.2016.1198903.

Syracuse, E.M., van Keken, P.E., Abers, G.A., 2010. The global range of subduction zone thermal models. Physics of the Earth and Planetary Interiors 183, 73–90. doi:10.1016/j.pepi.2010.02.004.

Takafuji, N., Fujino, K., Nagai, T., Seto, Y., Hamane, D., 2006. Decarbonation reaction of magnesite in subducting slabs at the lower mantle. Physics and Chemistry of Minerals 33, 651–654. doi:10.1007/s00269-006-0119-5.

Tange, Y., Takahashi, E., Nishihara, Y., ichi Funakoshi, K., Sata, N., 2009. Phase relations in the system MgO-FeO-$SiO_2$ to 50 GPa and 2000°C: An application of experimental techniques using multianvil apparatus with sintered diamond anvils. Journal of Geophysical Research 114. doi:10.1029/2008jb005891.

Tateno, S., Hirose, K., Ohishi, Y., 2014. Melting experiments on peridotite to lowermost mantle conditions. Journal of Geophysical Research: Solid Earth 119, 4684–4694. doi:10.1002/2013jb010616.

Thomson, A., Kohn, S., Bulanova, G., Smith, C., Araujo, D., Walter, M., 2016a. Trace element composition of silicate inclusions in sub-lithospheric diamonds from the juina-5 kimberlite: Evidence for diamond growth from slab melts. Lithos 265, 108–124. doi:10.1016/j.lithos.2016.08.035.

Thomson, A.R., Walter, M.J., Kohn, S.C., Brooker, R.A., 2016b. Slab melting as a barrier to deep carbon subduction. Nature 529, 76–79. doi:10.1038/nature16174.

Thomson, A.R., Walter, M.J., Lord, O.T., Kohn, S.C., 2014. Experimental determination of melting in the systems enstatite-magnesite and magnesite-calcite from 15 to 80 GPa. American Mineralogist 99, 1544–1554. doi:10.2138/am.2014.4735.

Trønnes, R.G., 2009. Structure, mineralogy and dynamics of the lowermost mantle. Mineralogy and Petrology 99, 243–261. doi:10.1007/s00710-009-0068-z.

Tschauner, O., Huang, S., Yang, S., Humayun, M., Liu, W., Corder, S.N.G., Bechtel, H.A., Tischler, J., Rossman, G.R., 2021. Discovery of davemaoite, $CaSiO_3$-perovskite, as a mineral from the lower mantle. Science 374, 891–894. doi:10.1126/science.abl8568.

Tschauner, O., Ma, C., Beckett, J.R., Prescher, C., Prakapenka, V.B., Rossman, G.R., 2014. Discovery of bridgmanite, the most abundant mineral in Earth, in a shocked meteorite. Science 346, 1100–1102. doi:10.1126/science.1259369.

Uchic, M.D., Holzer, L., Inkson, B.J., Principe, E.L., Munroe, P., 2007. Three-Dimensional Microstructural Characterization Using Focused Ion Beam Tomography. MRS Bulletin 32, 408–416. doi:10.1557/mrs2007.64.

Walter, M.J., Bulanova, G.P., Armstrong, L.S., Keshav, S., Blundy, J.D., Gudfinnsson, G., Lord, O.T., Lennie, A.R., Clark, S.M., Smith, C.B., Gobbo, L., 2008. Primary carbonatite melt from deeply subducted oceanic crust. Nature 454, 622–625. doi:10.1038/nature07132.

Walter, M.J., Koga, K.T., 2004. The effects of chromatic dispersion on temperature measurement in the laser-heated diamond anvil cell. Physics of the Earth and Planetary Interiors 143-144, 541–558. doi:10.1016/j.pepi.2003.09.019.

Watanuki, T., Shimomura, O., Yagi, T., Kondo, T., Isshiki, M., 2001. Construction of laser-heated diamond anvil cell system for in situ x-ray diffraction study at SPring-8. Review of Scientific Instruments 72, 1289. doi:10.1063/1.1343869.

Weir, C.E., Lippincott, E.R., Valkenburg, A.V., Bunting, E.N., 1959. Infrared studies in the 1- to 15-micron region to 30,000 atmospheres. Journal of Research of the National Bureau of Standards Section A: Physics and Chemistry 63A, 55. doi:10.6028/jres.063a.003.

Weis, C., Spiekermann, G., Sternemann, C., Harder, M., Vankó, G., Cerantola, V., Sahle, C.J., Forov, Y., Sakrowski, R., Kupenko, I., Petitgirard, S., Yavaş, H., Bressler, C., Gawelda, W., Tolan, M., Wilke, M., 2019. Combining X-ray K$\beta_{1,3}$, valence-to-core, and X-ray Raman spectroscopy for studying Earth materials at high pressure and temperature: the case of siderite. Journal of Analytical Atomic Spectrometry 34, 384–393. doi:10.1039/c8ja00247a.

Weng, X., Rez, P., Ma, H., 1989. Carbon E-shell near-edge structure: Multiple scattering and band-theory calculations. Physical Review B 40, 4175–4178. doi:10.1103/physrevb.40.4175.

Wille, H.C., Franz, H., Röhlsberger, R., Caliebe, W.A., Dill, F.U., 2010. Nuclear resonant scattering at PETRA III: Brillant opportunities for nano - and extreme

condition science. Journal of Physics: Conference Series 217, 012008. doi:10.1088/1742-6596/217/1/012008.

Williams, D.B., Carter, C.B., 1996. The transmission electron microscope, in: Transmission Electron Microscopy. Springer US, pp. 3–17. doi:10.1007/978-1-4757-2519-3_1.

Wirth, R., 2009. Focused ion beam (FIB) combined with SEM and TEM: Advanced analytical tools for studies of chemical composition, microstructure and crystal structure in geomaterials on a nanometre scale. Chemical Geology 261, 217–229. doi:10.1016/j.chemgeo.2008.05.019.

Yamazaki, D., Ito, E., Yoshino, T., Tsujino, N., Yoneda, A., Gomi, H., Vazhakuttiyakam, J., Sakurai, M., Zhang, Y., Higo, Y., Tange, Y., 2019. High-pressure generation in the Kawai-type multianvil apparatus equipped with tungsten-carbide anvils and sintered-diamond anvils, and X-ray observation on $CaSnO_3$ and $(Mg, Fe)SiO_3$. Comptes Rendus Geoscience 351, 253–259. doi:10.1016/j.crte.2018.07.004.

Yaxley, G.M., Brey, G.P., 2004. Phase relations of carbonate-bearing eclogite assemblages from 2.5 to 5.5 GPa: implications for petrogenesis of carbonatites. Contributions to Mineralogy and Petrology 146, 606–619. doi:10.1007/s00410-003-0517-3.

Yaxley, G.M., Ghosh, S., Kiseeva, E.S., Mallik, A., Spandler, C., Thomson, A.R., Walter, M.J., 2019. $CO_2$-rich melts in Earth, in: Orcutt, B.N., Daniel, I., Dasgupta, R. (Eds.), Deep Carbon. Cambridge University Press. chapter Chapter6, pp. 129–162. doi:10.1017/9781108677950.006.

Zedgenizov, D., Kagi, H., Shatsky, V., Ragozin, A., 2014. Local variations of carbon isotope composition in diamonds from São-Luis (Brazil): Evidence for heterogenous carbon reservoir in sublithospheric mantle. Chemical Geology 363, 114–124. doi:10.1016/j.chemgeo.2013.10.033.

Zhou, Q., Ma, Y., Cui, Q., Cui, T., Zhang, J., Xie, Y., Yang, K., Zou, G., 2004. Raman scattering system for a laser heated diamond anvil cell. Review of Scientific Instruments 75, 2432–2434. doi:10.1063/1.1763260.

Zhu, F., Li, J., Liu, J., Lai, X., Chen, B., Meng, Y., 2019. Kinetic control on the depth distribution of superdeep diamonds. Geophysical Research Letters 46, 1984–1992. doi:10.1029/2018gl080740.

# List of Figures

# List of Tables

# Zusammenfassung

Karbonate, die von subduzierenden Platten mitgeführt werden, könnten eine wichtige Rolle bei der Transport und Speicherung von Kohlenstoff im tiefen Erdinneren spielen. Aktuellen Schätzungen zufolge gelangen pro Jahr zwischen 40 und 66 Millionen Tonnen Kohlenstoff über Subduktionszonen ins Erdinnere, aber es ist unbekannt, wie viel davon den unteren Erdmantel erreicht. Es gibt Hinweise darauf, dass der größte Teil dieses Kohlenstoffs aus den subduzierenden Platten am Mantelkeil extrahiert wird und nur eine begrenzte Menge den tiefen Erdmantel erreicht. Die Schätzungen über tief subduzierten Kohlenstoff reichen von 0,0001 bis 52 Millionen Tonnen Kohlenstoff pro Jahr. Diese Diskrepanz ist in erster Linie auf das begrenzte Wissen über die Stabilität von Karbonatmineralen während ihres Transports in den tiefen Erdmantel zurückzuführen. In der Tat hat Kohlenstoff eine sehr geringe Löslichkeit in Mantelsilikaten, daher wird erwartet, dass er hauptsächlich in akzessorischen Phasen wie Karbonaten gespeichert wird.

Unter diesen Karbonaten nur Magnesit ($MgCO_3$) ist unter allen Mantelbedingungen stabil. Experimentelle Untersuchungen über die Stabilität von Magnesit im Kontakt mit $SiO_2$ bei niedrigeren Mantelbedingungen legen jedoch nahe, dass Magnesit nur entlang einer kalten subduzierten Plattengeotherme stabil ist. Darüber hinaus ist unser Verständnis der Stabilität von Magnesit in Wechselwirkung mit komplexeren Silikatphasen im Erdmantel noch unvollständig. Im ersten Teil dieser Dissertation wurde die Stabilität von Magnesit im Kontakt mit eisenhaltigen Mantelsilikaten anhand von Experimenten mit lasergeheizten Diamantstempelzellen und Vielstempel-Pressen untersucht. Dabei wurden Sub-Solidus-Reaktionen, Schmelzen, Dekarbonisierung und Diamantbildung unter Bedingungen im flachen bis mittleren unteren Erdmantel (25 bis 68 GPa; 1300 bis 2000 K) untersucht. Experimenten in der Vielstempel-Presse bei 25 GPa zeigen die Bildung von karbonatreicher Schmelze, Bridgmanit und Stishovit, wobei die erste Teilschmelze bei einer Temperatur auftritt, die über der kältesten Geothermen liegt. Die in-situ-Diffraktion in Experimenten

mit laserbeheizten Diamantstempelzellen zeigt die Kristallisation von Bridgmanit und Stishovit. Hierbei wurde keine Schmelzphase in situ nachgewiesen. Zum Nachweis von Dekarbonisierungsphasen wie Diamant wurden manche Proben mittels der Raman-Spektroskopie überprüft. Die Kristallisation von Diamanten wird als Sub-Solidus-Prozess selbst bei Temperaturen beobachtet, die für die kälteste Geothermie der Platte (1350 K bei 33 GPa) relevant und niedriger sind. Die aus dieser Arbeit gewonnenen Daten legen nahe, dass Magnesit im Kontakt mit dem umgebenden Peridotitmantel im oberen Teil desunteren Mantel instabil ist. Das Vorhandensein von Magnesit induziert stattdessen das Schmelzen unter oxidierten Bedingungen und/oder fördert die Bildung von Diamanten unter reduzierten Bedingungen in einer Tiefe von ∼700 km. Infolgedessen werden Karbonate aus den karbonatreichen Plattenim flachen unteren Mantel extrahiert, wo der Eintauchwinkel dieser subduzierten Plattenstagniert. Daher wird der Transport von Karbonat in größere Tiefen eingeschränkt sein, was für das Vorhandensein einer Barriere für die Subduktion von Kohlenstoff am oberen Ende des unteren Mantels spricht. Darüber hinaus liefert die Reduktion von Magnesit, aus der Diamanten entstehen, einen zusätzlichen Beweis dafür, dass die Kristallisation von Diamanten in großer Tiefe mit der Reduktion von Karbonaten oder karbonatreicher Schmelze zusammenhängt.

Im zweiten Teil dieser Dissertation wird die Entwicklung eines portabel Laserheizsystems vorgestellt, das für die Röntgenemissionsspektroskopie (XES) und die Spektroskopie mit nuklearer inelastischer Streuung (NIS) optimiert ist. Das Signal kann hierbei aus einer Diamantstempelzellein einem Winkel von nahezu 90° gesammelt werden. Die laserbeheizte Diamantstempelzelle ist das einzige statische Druckgerät, das den Druck und die Temperaturen des unteren Erdmantels und des Erdkerns erzeugenkann. Die hohen Temperaturen werden durch den Einsatz von Hochleistungslasern erreicht, die auf die Probe gerichtet sind, welche sich zwischen den Diamantstempeln befindet. Darüber hinaus ermöglicht die Transparenz von Diamanten im Wellenlängenbereich von Röntgenstrahlung in-situ röntgenspektroskopische Messungen, mit denen die Probe unter Hochtemperatur- und Hochdruckbedingungen untersucht werden kann. Um hierbei ausreichende Intensitäten im ausgehenden Signal zu erreichen, wurde das portabel Laserheizsystem für den Einsatz an Synchrotronanlagen konzipiert, die über keine eigenen Laserheizanlagen für Diamantstempelzellen verfügen. Beschrieben wird der allgemeine Aufbau des Systems. Außerdem werden Einzelheiten der Verwendung eines Parabolspiegels als reflektivem abbildenden Objektivs für die Laserheizung dargelegt. Der Parabolspiegel verbessert die Genauigkeit von Temperaturmessungen, da er über einen breiten Spektralbereich frei von chro-

matischer Aberration ist. Eine Perforation dieses Spiegels ermöglicht seinen Einsatz bei in-situ Röntgenstrahlungsmessungen an Synchrotronanlagen. Der Parabolspiegel ist eine gut geeignete Alternative zu refraktiven Objektiven in Laserheizsystemen und wird künftige Anwendungen beim Einsatz von $CO_2$-Lasern erleichtern.

# Acknowledgments

This project was made possible by funding the Deutsche Forschungsgemeinschaft (DFG) through the research unit FOR 2125 - 'CarboPaT' (AP 262/1-1).

This work will not have been possible without the efforts of many people. I express my gratitude to Max Wilke and Karen Appel, for trusting me on this project, and for the numerous opportunities and experiences I got the chance to be part of during the time of this thesis. I am appreciative of all the members of the CarboPaT group, for the interesting discussions during our group meetings and for making the collaboration with BGI possible.

I am deeply grateful to Dr. Georg Spiekermann, for your unlimited support, and trust all the way until the end. Your curiosity and dedication have been contagious and it is with nostalgia that I think of all the long but great hours spent with you in the lab and at beamtimes. You never failed to be present and to provide advice during the challenging times, which significantly impacted me and the work presented in this dissertation. I owe you a lot.

I am very thankful to Dr. Ingrid Blanchard, you have played an essential role in the last two years and provided essential suggestions during the writing of the paper and this manuscript. Thanks for sharing your skills with diamond-anvil cells, and guiding me in my future career development.

A special thanks to Johannes Kaa, who has been my best buddy for so many (stressful) beamtimes, and for the translation of the abstract in german. Thanks for being around and having my back.

I want to acknowledge the people of the institute of Geoscience of the University of Potsdam: Dr. Christina Günther, Christine Fischer, Tanja Klaka-Tauscher, Cornelia Becker, Annika Mareck, Ines Münch, Corinna Kallich, and Jens Bölke. I have also spent some time at the GFZ, and I am really grateful for the work of Anja Schreiber at the FIB and Dr. Vladimir Roddatis at the TEM.

I am deeply thankful to my friends, officemates, and colleagues: Dr. Alessia Borghini for being a great friend since my first day in the institute, Dr. Magda Patyniak, Theresa Rein, Maria R. P. Sudibyo, Isabel Wapenhans, for all the great discussions and support in the office, Dr. Mirko Förster for your help with Overleaf, Dr. Serena Dominijanni for the multi-anvil press experiments, Leïla Coudray, Dr. Audrey Margirier, Asfaw Erbello Doelesso, Dr. Niels Meijer, Dr. Edith Kubick, LingXiao Gong, Dr. Lea Pennacchioni, Dr. Maxime Bernard, Dr. Julien Amalberti and Dr. Verónica Torres Acosta for all the good times, coffee breaks, support and love you gave me. I have been lucky to have you all and had such a great stay in Potsdam.

Lastly, to the important people in my life, my mom, my family, Yoann, and Cody for their unconditional love and support in all my choices, if I managed to reach my goals, it is thanks to you.